Accurate Nanofabrication Techniques for High-Index-Contrast Microphotonic Devices

by

Tymon Barwicz

B.Eng. Engineering Physics (2000)
École polytechnique de Montréal

Submitted to the Department of Materials Science and Engineering
in Partial Fulfillment of the Requirements for the Degree of
Doctor of Philosophy in Materials Science and Engineering

at the

Massachusetts Institute of Technology

September 2005

© 2005 Massachusetts Institute of Technology
All rights reserved

Signature of Author..
Department of Materials Science and Engineering
August 1, 2005

Certified by ....
Henry I. Smith
Joseph F. and Nancy P. Keithley Professor of Electrical Engineering
Thesis Supervisor

Certified by ....
Harry L. Tuller
Professor of Ceramics and Electronic Materials
Thesis Supervisor

Accepted by ....
Gerbrand Ceder
R.P. Simmons Professor of Materials Science and Engineering
Chair, Departmental Committee on Graduate Students

Accurate Nanofabrication Techniques for High-Index-Contrast Microphotonic Devices

by

Tymon Barwicz

Submitted to the Department of Materials Science and Engineering
on August 1, 2005 in Partial Fulfillment of the
Requirements for the Degree of Doctor of Philosophy
in Materials Science and Engineering

ABSTRACT

High-refractive-index-contrast microphotonic devices provide strong light confinement allowing for sharp waveguide bends and small dielectric optical resonators. They allow dense optical integration and unique applications to optical filters and sensors but present exceptional complications in design and fabrication. In this work, nanofabrication techniques are developed to address the two main challenges in fabrication of high-index-contrast microphotonic devices: sidewall roughness and dimensional accuracy.

The work focuses on fabrication of optical add-drop filters based on high-index-contrast microring-resonators. The fabrication is based on direct-write scanning-electron-beam lithography. A sidewall-roughness characterization and optimization scheme is developed as is the first three-dimensional analysis of scattering losses due to sidewall roughness. Writing strategy in scanning-electron-beam lithography and absolute and relative dimensional control are addressed.

The nanofabrication techniques developed allowed fabrication of the most advanced microring add-drop-filters reported in the literature. The sidewall-roughness standard-deviation was reduced to 1.6 nm. The field polarization and the waveguide cross-sections minimizing scattering losses are presented. An absolute dimensional control accuracy of 5 nm is demonstrated. Microring resonators with average ring-waveguide widths matched to 26 pm to a desired relative width-offset are reported.

Thesis Supervisor: Henry I. Smith
Title: Joseph F. and Nancy P. Keithley Professor of Electrical Engineering

Thesis Supervisor: Harry L. Tuller
Title: Professor of Ceramics and Electronic Materials

Table of Contents

Chapter 1 Introduction **19**

PART I High-Index-Contrast Filters **23**

Chapter 2 Background **25**

2.1 Optical add-drop filters 25
2.2 Microring-Resonator Filters 28
2.2.1 How They Work 28
2.2.2 Spectral Response of Microring Filters 30
2.2.3 Racetrack Resonators and Vernier Operation 32

Chapter 3 Fabricated Add-Drop Filters **35**

3.1 Introduction 35
3.2 Structures Overview 35
3.3 One-Layer Fabrication Process 38
3.4 Fabricated Third-Order Filters 40
3.4.1 First Third-Order Filters 40
3.4.2 First Frequency-Matched Filters 45
3.4.3 Multistage Filters 49
3.4.4 Polarization-Independent Filters 54
3.4.4.1 Integrated Polarization Diversity 54
3.4.4.2 Two-Layer Fabrication Process 56
3.4.4.3 Fabricated Polarization-Independent Filters 59
3.4.5 Summary 62
3.5 FSR-doubled Filters 63
3.6 Conclusion 67

PART II Sidewall Roughness **69**

Chapter 4 Roughness Characterization **71**

4.1 Introduction 71
4.2 Roughness Model 73
4.3 Measuring Roughness: Methodology 74
4.3.1 Acquiring Micrographs 74
4.3.2 Obtaining $f(z)$ from the micrographs 75
4.3.3 Obtaining a spectral density estimate from $f(z)$ 75

4.3.4 Fitting the spectral density estimate to the roughness model ... 77
4.4 Experiment ... 78
4.4.1 Evolution of LER during fabrication of HIC microphotonic devices ... 78
4.4.2 Study of resist ... 80
4.4.3 Study of RIE ... 81
4.5 Discussion ... 82
4.6 Conclusion ... 83

Chapter 5 Roughness Optimization ... 85

5.1 Introduction ... 85
5.2 Liftoff Optimization ... 86
5.3 Reactive-Ion Etching Optimization ... 90
5.4 Resulting Sidewall Roughness ... 91
5.5 Chemical Polishing ... 93
5.6 Conclusion ... 94

Chapter 6 Roughness-Induced Optical Loss ... 97

6.1 Introduction ... 97
6.2 Roughness Model ... 99
6.3 Volume Current Method ... 101
6.4 Three-Dimensional Analysis ... 102
6.4.1 Problem Decomposition ... 102
6.4.2 Impact of Waveguide Height, Field Polarization, Vertical Field-Shape, and Roughness Statistics ... 106
6.5 High Index-Contrast ... 112
6.5.1 Rationale ... 112
6.5.2 Dyadic Green's Functions in One-Layer Media ... 115
6.5.2.1 Coordinate System ... 115
6.5.2.2 Dyadic Green's Functions in Layered Media ... 116
6.5.2.3 Leading-Order Solution ... 119
6.5.3 Scattering Losses ... 121
6.6 Numerical Results ... 124
6.7 Discussion ... 128
6.7.1 Trends ... 128
6.7.2 Quick Scattering-Loss Estimates. ... 134
6.7.3 Extension of the Roughness Model ... 136
6.7.4 Propagation Loss in Fabricated Filters ... 137
6.7.4.1 Propagation Loss Analysis ... 137

6.7.4.2 Potential Sources of SiN Material Loss ... 138
6.7.5 Scattering Losses in Microring Resonators ... 140
6.7.6 Scattering Losses due to Lithographic Discretization ... 141
6.8 Conclusion ... 143

PART III Dimensional Accuracy ... 145

Chapter 7 Pattern Fidelity ... 147

7.1 Introduction ... 147
7.2 SEBL Writing Strategy ... 147
7.3 Conclusion ... 151

Chapter 8 Process Calibration: Absolute Dimensional Control ... 153

8.1 Introduction ... 153
8.2 Process Calibration ... 154
8.3 Resulting Dimensional Control ... 156
8.4 Conclusion ... 157

Chapter 9 Frequency Matching: Relative Dimensional Control ... 159

9.1 Introduction ... 159
9.2 Frequency Matching Strategy ... 160
9.3 Proximity Function ... 161
9.4 Fast Proximity Effects Computation ... 166
9.5 Predicted Microring Shapes ... 168
9.6 Comparison of Predicted and Measured Dimensions ... 172
9.7 Experimental Results ... 174
9.8 Conclusion ... 179

Chapter 10 Conclusions ... 181

10.1 Summary of Accomplishments ... 181
10.2 Future Work ... 182

Appendix A Raith 150 ... 185

A.1 General Operation ... 185
A.1.1 Introduction ... 185
A.1.2 Column-Related Problems ... 186
A.1.3 Stage-Related Problems ... 187
A.1.4 Bugs ... 189
A.2 Multilayer Exposures ... 190

A.2.1 Introduction 190
A.2.2 Signal 191
A.2.3 Alignment Marks and Acquisition 191

Bibliography 195

List of Figures

Fig. 2.1 Schematic of a modern optical network....26
Fig. 2.2 Add-drop-filter functionality. 27
Fig. 2.3 Spectral response of an add-drop filter 28
Fig. 2.4 Schematic and spectral response of a microring-resonator add-drop filter....29
Fig. 2.5 Schematic and spectral response of a third-order microring resonator....31
Fig. 2.6 Schematic of a racetrack-resonator add-drop filter....33
Fig. 2.7 Illustration of the Vernier effect 34

Fig. 3.1 Designed series-coupled third-order microring filters....37
Fig. 3.2 One-layer fabrication process overview 38
Fig. 3.3 Cross-section of a smooth SiN waveguide 39
Fig. 3.4 Electron micrograph of the first third-order microring filters 41
Fig. 3.5 Measured and simulated response of the first third-order microring filters 44
Fig. 3.6 Micrograph and spectral responses of frequency-matched filters. 46
Fig. 3.7 Cascaded third-order filters used to enhance the in-band extinction....49
Fig. 3.8 Electron micrographs of fabricated multistage filters 50
Fig. 3.9 Spectral responses of fabricated multistage filters 52
Fig. 3.10 Measured and calculated spectral responses at drop-ports of successive stages of a three-stage filter. 53
Fig. 3.11 Integrated polarization-diversity scheme....54
Fig. 3.12 Integrated polarization splitter and rotator....55
Fig. 3.13 Polarization-independent fiber-to-chip coupler....56
Fig. 3.14 Novel multilayer fabrication process used for the polarization independent add-drop-filters....57
Fig. 3.15 Electron micrographs of waveguide cross-sections obtained using the fabrication process presented in Fig. 3.14 58
Fig. 3.16 Schematic and optical micrograph of the polarization-independent add-drop filter. 60
Fig. 3.17 Spectral response of a polarization independent add-drop filter for 50 random polarizations....61

Fig. 3.18 Schematic of a second-order microring filter with doubled FSR 64
Fig. 3.19 Nomarski optical micrograph of an FSR-doubled filter 65
Fig. 3.20 Spectral response of an FSR-doubled filter. 66

Fig. 4.1 Schematic of a line with rough edges. Roughness is described by a 1D distribution with zero mean called $f(z)$. 73
Fig. 4.2 Roughness spectral density estimates presenting the evolution of line-edge roughness during fabrication of HIC microphotonic devices..79

Fig. 5.1 Problems with liftoff of Cr...87
Fig. 5.2 Impact of resist profile on waveguide sidewall roughness 89
Fig. 5.3 Top-view electron-micrographs of bus-waveguides from various fabricated filters illustrating the sidewall roughness. 92
Fig. 5.4 Side-view electron-micrograph of a ring-to-ring coupling gap illustrating the sidewall roughness..93

Fig. 6.1 Schematic of a rough rectangular waveguide and spherical coordinate system used 99
Fig. 6.2 Decomposition of the radiation problem 104
Fig. 6.3 Relation between two- and three-dimensional array-factors of a line array. 105
Fig. 6.4 Radiation efficiency of the x- and y-polarization for various vertical-field-shapes and roughness statistics.. 107
Fig. 6.5 Radiation efficiency of the z-polarization for various vertical-field-shapes and roughness statistics, and schematic of the vertical-field-profiles used 108
Fig. 6.6 Radiation profile of a point source with various polarizations and forms of the power array-factors corresponding to various vertical-field-shapes 110
Fig. 6.7 Cross-section of the roughness power-array-factor for practical roughness correlation lengths. 112
Fig. 6.8 Actual and approximate dielectric distribution used for computation of the radiation profile 113
Fig. 6.9 Current sources in a one-layer medium and applicability of free-space array factors...114
Fig. 6.10 Schematic of planar layered-media and rotated coordinated system used in the high index-contrast analysis. 117

Fig. 6.11 Vertical profiles of the current sources used to approximate the shapes of the modes at the rough boundary. 123
Fig. 6.12 Radiation efficiency of SiON (n_{core}=1.50) waveguides embedded in a SiO_2 (n_{clad}=1.45) cladding. 125
Fig. 6.13 Radiation efficiency of Si_3N_4 (n_{core}=2.00) waveguides embedded in a SiO_2 (n_{clad}=1.45) cladding 126
Fig. 6.14 Radiation efficiency of Si (n_{core}=3.50) waveguides embedded in a SiO_2 (n_{clad}=1.45) cladding 127
Fig. 6.15 Scattering losses in dB/cm normalized to the roughness variance in nm^2 for SiON (n_{core}=1.50) waveguides embedded in a SiO_2 (n_{clad}=1.45) cladding 129
Fig. 6.16 Scattering losses in dB/cm normalized to the roughness variance in nm^2 for Si_3N_4 (n_{core}=2.00) waveguides embedded in a SiO_2 (n_{clad}=1.45) cladding 130
Fig. 6.17 Scattering losses in dB/cm normalized to the roughness variance in nm^2 for Si (n_{core}=3.50) waveguides embedded in a SiO_2 (n_{clad}=1.45) cladding. 131
Fig. 6.18 Impact of roughness correlation length on scattering losses. 134
Fig. 6.19 Illustration of deterministic roughness introduced by lithographic pixelization. 142

Fig. 7.1 Electron micrographs demonstrating e-beam deflection errors introduced by the Raith 150. 148
Fig. 7.2 Various e-beam vector-scanning strategies for microrings and observed problems in practice. 149
Fig. 7.3 Micrograph of a lithographically perfect microring exposed in PMMA using the writing strategy presented in Fig. 7.2d. 150

Fig. 8.1 Impact of e-beam proximity effects on absolute dimensional control 155

Fig. 9.1 Frequency matching strategies. 160
Fig. 9.2 Empirical methods used to obtain the e-beam proximity function 162
Fig. 9.3 Experimentally obtained e-beam proximity function 165
Fig. 9.4 Resist clearing-dose contours in first frequency-matched filters for various exposure doses 169
Fig. 9.5 Resist clearing-dose contours in multistage filters for various SEBL exposure doses. 170

Fig. 9.6 Predicted frequency mismatch between middle and outer microrings due to e-beam proximity effects and required dose-compensation 171
Fig. 9.7 Predicted and measured width variations in ring waveguides of first frequency-matched filters 173
Fig. 9.8 Frequency mismatch observed in experiment at various dose-compensations for first-frequency-matched filters and multistage filters 175
Fig. 9.9 Drift of the absolute resonant frequency of outer rings with filter position on the optical chip 178

Fig. A.1 Illustration of the multilayer alignment strategy.....................................192

List of Tables

Table 3.1 Designed third-order-filter parameters 37
Table 3.2 Vertical waveguide parameters of first third-order filters 42
Table 3.3 Waveguide vertical parameters of first frequency-matched filters 48
Table 3.4 Performance of polarization dependent third-order-filters 62
Table 3.5 Designed FSR-doubled filter parameters 64

Table 4.1 Spectral density of line-edge roughness at various stages of fabrication 80

Table 5.1 Measured sidewall roughness on fabricated filters 91

Table 6.1 Measured and expected polarization dependence of propagation loss 138

Table 8.1 Process calibration performance 156

Table 9.1 E-beam proximity function fitted parameters 167
Table 9.2 Calculated and observed frequency mismatch 176

List of Acronyms

1D: One-dimensional

2D: Two-dimensional

3D: Three-dimensional

CIFS: Coupling-induced frequency shift

FDTD: Finite-difference-time-domain

FSR: Free spectral range

HIC: High refractive-index contrast

HSQ: Hydrogen silsesquioxane

LER: Line-edge roughness

LPCVD: Low-pressure chemical-vapor deposition

MPE dose: Minimum-proximity-effect dose

OADM: Optical add-drop multiplexer

PMMA: Poly-methyl-methacrylate

RIE: Reactive-ion etching

SEBL: Scanning-electron-beam lithography

SEM: Scanning-electron microscopy

Acknowledgments

I would like to start by thanking my closest collaborators: Miloš A. Popović, Michael R. Watts and Peter T. Rakich. They are responsible for the outstanding optical design and characterization work required for the fabricated filters presented in this Thesis. I believe we made a great team and hope we will have the opportunity to work together in the future.

I would like to thank the members of MIT's NanoStructures Laboratory (NSL). In particular, I thank Prof. Henry I. Smith, my primary Thesis advisor and men of remarkable scientific inquisitiveness, from whom I have learned more than he presumes. Remarkably, he directs NSL as a big family and not as a small company providing exceptional freedom to his students. In addition, I thank J. Todd Hastings and Joseph Huang, two NSL alumni, who have spent considerable energy in introducing me to NSL's facilities and teaching me e-beam lithography. Moreover, I thank Feng Zhang, who helped me troubleshoot the Raith 150 on a regular basis, and Minghao Qi, who was my officemate throughout my doctoral studies. Finally, I thank Jim Daley and underline his dedication in running the laboratory.

In the first half of my doctoral studies, I had the exceptional opportunity to work with Prof. Hermann A. Haus, who inspired two generations of students during his incredible life at MIT. In the second half of my doctoral studies, Profs. Erich P. Ippen and Franz X. Kaertner became my unofficial co-advisors. I would like to thank them for having always been a source of countless support.

Last but not least, I would like to thank Luciano Socci, who has been smoothing our relations with Pirelli Labs (Milan, Italy), our main sponsor, and has always been very entertaining in doing so.

Chapter 1

Introduction

As all living beings, humans need to communicate. Short distance communication was developed first and the unaided human body was sufficient for it. Long distance communication was developed next. Messengers were the first natural choice but their intrinsic communication time-delay was inadequate for many applications. In some parts of the world, smoke signals or acoustically loud devices were employed. Then, came the telegraph and radio telecommunication. Humans went from using oscillations of air molecules to electrons in metallic cables to photons in free-space and, more recently, in optical fibers.

The new optical communication era offers significant excitement and new possibilities. It allowed the internet to become the most important communication medium in our small but commanding industrialized world. Creating integrated optical circuits on planar surfaces by microfabrication techniques (microphotonic integration) to generate complex optical functions was born to respond to the needs of these optical networks. Planar integration eliminates alignment issues, reduces coupling losses, and shrinks the size and the fabrication cost of complex elements. As did microelectronics, microphotonics have the potential to impact significantly the way we live. Surprisingly, despite considerable efforts toward microphotonic integration in the last decade, the

optical-network-component market is still dominated by components that cannot be integrated on a planar surface such as thin-film filters and devices based on free-space light-propagation combined with micro-electro-mechanical mirrors and gratings. This is in contrast with the evolution of microelectronics. After the integrated circuit was invented by Robert Noyce in 1959, it was widely applied to commercially available computers by the mid 1960s. The difference between microelectronics then and microphotonics now is the required complexity of the devices they are used to build. Complexity is the driving force for integration. Simple elements are often better and more easily made without planar integration. The cost of a transistor that is part of a complex computer-chip has dropped by a factor of 100 in the last 25 years. This is because the fabrication-cost of a modern transistor is shared with the billions of other transistors making up the computer chip. However, fabricating stand-alone transistors with the microfabrication techniques used for complex computer-chips would result in prohibitive cost and performance.

Today, as a result of the difficult economics resulting from the optical network over-capacity created by the internet rush of the 1990s, low-cost, and not performance, is the driver for optical-network elements. At this time, optical networks do not require the complex optical elements motivating microphotonic integration and the required complexity is expected to increase at a slow pace as the focus is on low-cost and not on performance. A better motivation for microphotonics is to achieve isolated-device functionality not otherwise possible. For instance, high refractive-index-contrast (HIC) between the core and the cladding of dielectric microphotonic waveguides have shown growing interest as they provide strong confinement of light allowing unique possibilities such as small resonators, sharp bends, and dense integration. Small HIC dielectric resonators are exceptionally sensitive to perturbation of their environment making them

excellent candidates for high-sensitivity detectors, widely-tunable filters, and fast optical switches. Unfortunately, HIC microphotonic devices are uniquely difficult to design and fabricate and have shown limited success in practical applications. In design of HIC devices, the small-perturbation assumption cannot usually be applied, prohibiting the application of most analytical design tools and requiring intensive three-dimensional simulations. In fabrication, HIC devices require sidewall smoothness and dimensional control well beyond of what is achieved in microelectronics, for which most microfabrication processes have been developed.

In this work, we address the challenges in fabricating HIC microphotonic devices. We focus on fabrication of HIC microring resonators for optical add-drop multiplexers. Problems which need to be addressed in the fabrication of HIC microrings need to be addressed in fabrication of all HIC resonators and almost all HIC microphotonic devices. Hence, this work applies to fabrication of HIC microphotonic devices in general. This includes integrated photonic-bandgap structures.

The present Thesis is arranged in three parts. First, the fabricated HIC microring filters are presented in Part I. The fabrication is based on direct-write scanning-electron-beam lithography (SEBL). We demonstrate the most advanced microring add-drop filters that have ever been reported in literature. Part I allows us to identify and illustrate the fabrication problems that had to be addressed. Then, the identified problems are tackled in details in Part II and Part III, which represent the scientific core of the Thesis.

In Part II, sidewall roughness is characterized and optimized, and the induced optical-loss calculated. The spectral density of sidewall roughness is measured at various stages of fabrication, identifying the fabrication steps inducing scattering losses. Then, these steps are empirically optimized. Finally, a three-dimensional analysis of scattering losses due to sidewall roughness, valid for any refractive-index-contrast and field

polarization, is presented. To our knowledge, this is the first scattering losses analysis that explicitly considers how the radiation pattern is affected by the waveguide cross-section. It allows better understanding of the propagation-loss mechanism in microphotonic waveguides and recommending waveguide cross-sections minimizing scattering losses.

In Part III, lithographic-pattern accuracy is addressed. The SEBL scanning strategy is first optimized to be better suited for the smooth curves required in HIC microphotonic devices. Then, a process calibration technique is presented to obtain strict absolute dimensional control. Finally, relative dimensional control is investigated. Resonant frequency disparities between adjacent resonators produced by slight dimensional changes are calculated and corrected.

The present text assumes that the reader has a basic knowledge of microfabrication techniques. To gain the required microfabrication background, please refer to [1]. The needed knowledge of optical networks is presented in Chapter 2.

PART I

High-Index-Contrast Filters

Chapter 2 Background .... p. 25

Chapter 3 Fabricated Add-Drop Filters .... p. 35

In Part I, an introduction to optical networks and microring filters is presented. Then, the fabricated high-index-contrast microring filters are reported. Part I allows us to identify and illustrate the fabrication problems that need to be addressed in fabrication of high-index-contrast devices. The nanofabrication techniques developed to address these problems are further described in Parts II and III of the Thesis. The developed techniques allowed fabrication of the most advanced microring add-drop filters reported in the literature.

Chapter 2

Background

2.1 OPTICAL ADD-DROP FILTERS

A modern optical ring-network is shown in Fig. 2.1. It is formed of interconnected rings of optical fiber. Each node of the optical network communicates with other nodes on dedicated wavelengths, also called channels. A node could be a building, a neighborhood or even a large town. The channels are all carried on the same optical fiber and densely space in a relatively narrow spectral band centered around 194 THz (free-space wavelength of 1550 nm). As of 2005, a single channel carries up to 40 Gb/s of data, which requires a minimum channel spectral-width of 40 GHz (~0.32 nm). The spectral-spacing between center-wavelengths of such consecutive channels can be as small as 100 GHz (~0.8 nm). This is referred to as dense wavelength-division multiplexing (DWDM). Obviously, there are many different DWDM schemes with diverse channel widths and channel spacings. Nonetheless, all schemes are limited to spectral bands defined by the operational spectral ranges of optical fiber amplifiers. First, the conventional band (C-band) is based on conventional Er-doped fiber amplifiers and spans a spectral window from about 1530 to 1565 nm. Then, the short band (S-band, 1460-1530 nm) is based on fiber Raman amplifiers and the long band (L-band, 1565-1625 nm)

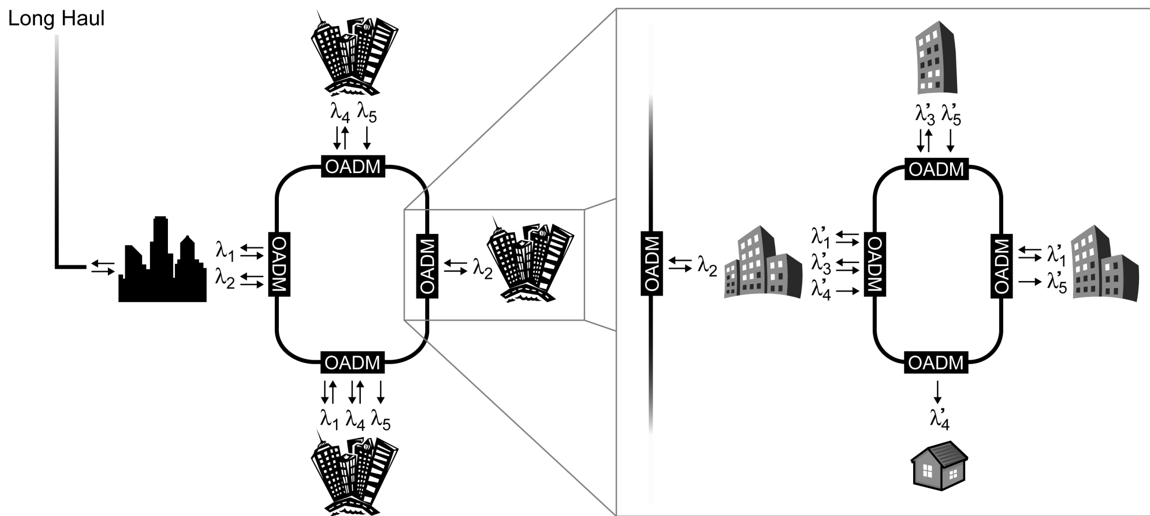

Fig. 2.1 Schematic of a modern optical network employing interconnected rings of optical fiber. Each node of the optical network communicates with other nodes on dedicated wavelengths, which are also called channels. An optical add-drop multiplexer (OADM) is required at every node. An OADM is formed of a set of add-drop filters, which are described in Fig. 2.2.

is based on gain-shifted Er-doped fiber amplifiers [2]. The S- and L-bands have shown increasing interest in recent years but are not yet widely employed. The common goal is to fit as much bandwidth as is reasonably possible in a given spectral window with either numerous low-bandwidth tightly-spaced channels or fewer wider-bandwidth more-loosely-spaced channels.

Each node requires an optical add-drop multiplexer (OADM). An OADM is formed of a set of optical add-drop filters. As shown in Fig. 2.2, an add-drop filter must reroute (drop) the data stream carried at a given wavelength (λ_k) and replace it (add) by a new data stream (λ_k') carried at the wavelength that was just dropped. This must be done without disturbing the other channels ($\lambda_{i\neq k}$).

A spectral response of an add-drop filter is presented in Fig. 2.3. The response should be as square as possible. The input-to-drop loss, the loss on the adjacent channels and the ripple need to be minimized. On the other hand, the in-band extinction and the

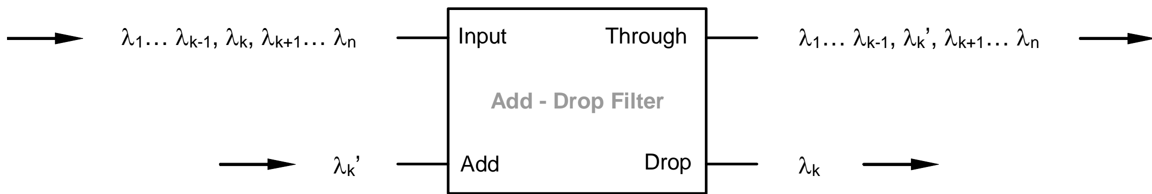

Fig. 2.2 Add-drop-filter functionality. An add-drop filter must reroute (drop) the data stream carried at a given wavelength (λ_k) and replace it (add) by a new data stream (λ_k') carried at the wavelength that was just dropped. This must be done without disturbing the data streams carried on the other wavelengths ($\lambda_{i\neq k}$).

out-of-band rejection need to be maximized. Usually, a ~3 dB drop loss is tolerated while only a ~1 dB loss on adjacent channels is found acceptable. The ripple introduces dispersion in the dropped channel and needs to be kept below ~0.1 dB. Dispersion can induce transmission errors by distorting the optical impulses forming the data stream. In general, dispersion is created by slope in the filter spectral response and should not exceed ~22 ps/nm. Power left in the through-port from the dropped data-stream (λ_k) will act as noise for the added data-stream. Similarly, power rerouted to the drop-port from adjacent channels will act as noise for the dropped data-stream (if the dropped port is connected to a detector) or as noise for other adjacent channels (if the dropped data-stream is directed towards another optical fiber). Hence, the through extinction and the out-of-band rejection must both reach at least 30 dB.

For an OADM to be useful in practice, it has to fulfill two additional requirements. First, the spectral responses of the add-drop filters must be polarization independent. The polarization state in a fiber changes randomly. Any polarization dependence in the add-drop filters would means that their performance would change randomly in time. Second, the OADM should be reconfigurable. In other words, one should be able to drop any channel and output it on any of the OADM drop ports while the system is in use. This can be accomplished by using tunable add-drop filter, where the spectral response of the filter

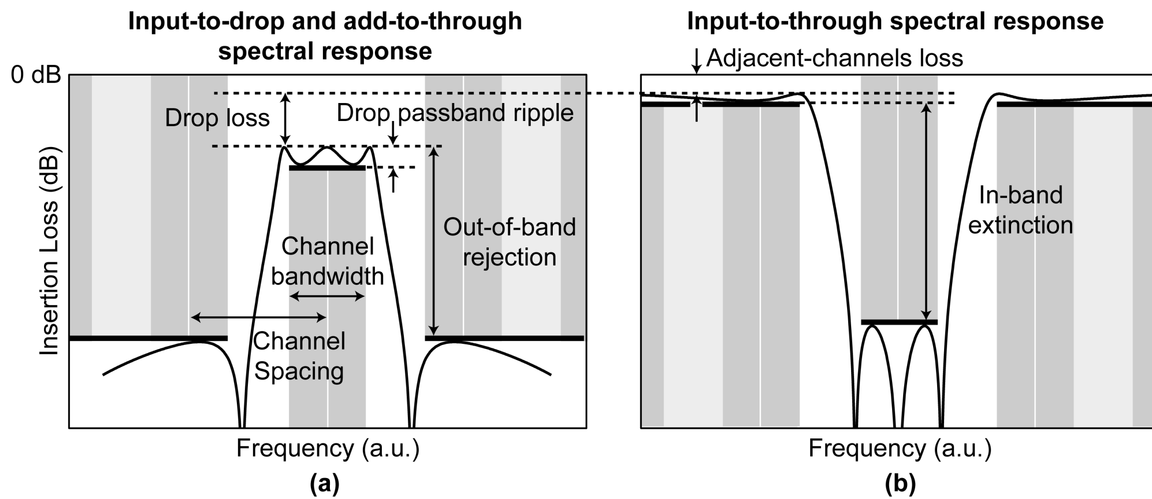

Fig. 2.3 Spectral response of an add-drop filter. (a) Input-port to drop-port and add-port to through-port spectral response. (b) Input-port to through-port spectral response. An elliptic filter response is used in this illustration. [Calculation by M.A. Popovič]

can be shifted and precisely positioned in the spectral domain over the entire spectral band used. Another approach is to use a complete set of switchable add-drop filters statically positioned on given channels. In this scheme, all add-drop filters are turned off but for the one corresponding to the channel to be dropped. Numerous other architectures are also possible. However, the heart of the challenge is creating an add-drop filter that is widely tunable or quickly switchable.

2.2 MICRORING-RESONATOR FILTERS

2.2.1 How They Work

Optical ring resonators were proposed in 1969 [3]. However, it was only in the late 1990s that fabrication advances made it plausible to consider these structures for add-drop filters. A microring resonator filter is shown in Fig. 2.4a. Let us imagine a monochromatic wave launched in the input port. The wave will evanescently couple to

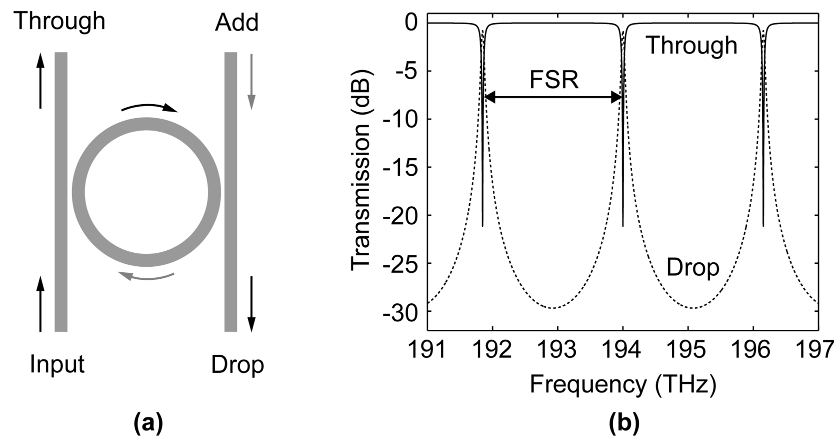

Fig. 2.4 (a) Schematic of a microring-resonator add-drop filter. (b) Spectral response of a single microring resonator. The spectral distance between resonances is called the free-spectral-range (FSR).

the ring and start propagating in it. If the optical path length in the ring corresponds to an integer number of wavelengths, there will be resonance and a significant amount of power will be transferred to the ring. If the input and output coupling coefficient are properly chosen, nearly all optical power will be extracted from the input bus-waveguide and redirected to the drop-port. Each time a wave is evanescently coupled from one waveguide to another without significant coupler loss, it is phase shifted by 90 degrees with respect to the wave in the primary waveguide. Hence, the wave in the ring is 90 degrees phase shifted with respect to the wave in the input bus-waveguide. When the wave in the ring is resonant and couples back to the input bus-waveguide, the phase shift with the primary wave is mainly induced by the evanescent coupling, reaches 180 degrees, and results in destructive interference. Thus, after a short transient state, the optical power in the ring will have built up sufficiently to kill most of the wave in the through port. The microring filter exhibits two-fold rotational symmetry so the add function is accomplished in the same way as the drop function.

2.2.2 Spectral Response of Microring Filters

The spectral response of a single-microring filter is presented in Fig 2.4b. The spectral distance between two consecutive resonances is called the free-spectral-range (FSR). As only a single channel should be dropped at a time by a given add-drop filter, the FSR needs to be as wide as the spectral band used (usually 30 nm or more). The smaller the resonator is, the larger the spectral spacing between the resonances. The microring diameter needs to be on the order of 10 μm to provide an FSR on the order of 30 nm (this is dependent on the refractive index of the material used). Such small microrings require strong light confinement to manage bending loss. This is the primary reason for which high-refractive-index-contrast has to be used for microring filters.

The frequency selectivity of a single microring is most often measured through the quality factor of the resonator (Q). Q is defined as the time averaged stored energy per optical cycle divided by the power leaving the resonator. It is related to the wavelength selectivity through $Q \approx \lambda/\Delta\lambda$ where $\Delta\lambda$ is the full-width at half-maximum (FWHM) of the resonance peak. Power leaving the resonator is due to scattering loss, material loss, and bending loss as well as to coupling to the bus waveguides. The smaller the couplings to the bus waveguides and the losses in the ring are, the longer the photon lifetime in the ring, the larger the Q, and the sharper the resonance. In short, the coupling strength defines the bandwidth of the filter as it, and not the losses in the ring, need to be the Q limiting factor (photon-lifetime limiting-factor) in add-drop filters.

An elegant way of looking at single-ring resonators is to reduce them to Fabry-Perot resonators. Accordingly, one considers the input and output waveguides as the Fabry-Perot mirrors. The transmission of the mirrors is equated to the evanescent coupling between the waveguides and the ring. In consequence, the spectral selectivity of a ring

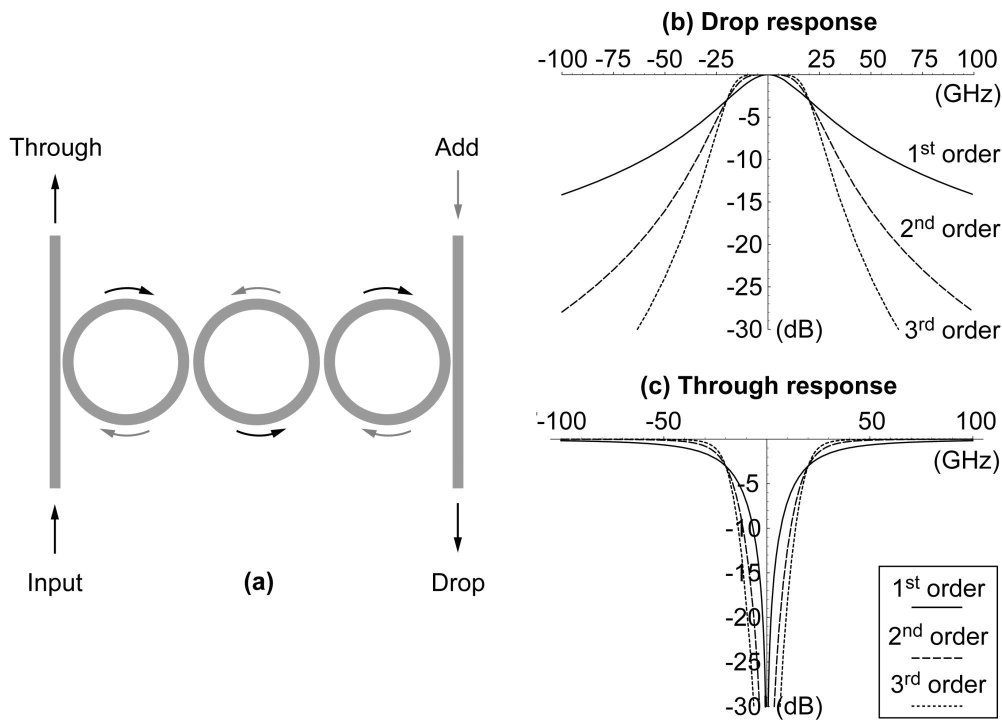

Fig. 2.5 (a) Schematic of a third-order microring resonator. (b) Drop-port response and (c) through-port response of first-, second-, and third-order microring filters [Calculation by M.A. Popovič]

resonator is sometimes described by its finesse (F) which is defined as $F = FSR/\Delta\lambda$ where $\Delta\lambda$ is the FWHM of the resonance peak.

A single microring forms a first-order filter, which yields a Lorentzian response. It is not square enough for DWDM applications, where a flat top and a sharp roll-off are required. These characteristics are obtained with appropriate high-order filters. A higher-order than first-order microring filter can be obtained by arranging multiple microrings in a series-coupled configuration. A third-order microring filter requires three microrings and is presented in Fig. 2.5 along with the spectral responses of first-, second-, and third-order filters. By appropriate selection of the coupling ratios between the microrings, standard electronic filter responses such as Chebyshev, Butterworth, and elliptic can be obtained [4].

In summary, the bus-to-ring couplings control the filter finesse (FSR/bandwidth), the ratios between bus-to-ring and the various ring-to-ring couplings control the filter shape, and the optical path lengths in the microrings (microring radius and optical propagation constant) control the resonant frequency and the FSR of the filter.

The optical propagation constant can be adjusted by changing the cross-section of the waveguides. It is most often expressed through the effective refractive-index of the waveguide defined as

$$n_{eff} = \beta / k_0 ,$$

where β is the propagation constant and k_0 is the free-space wavenumber. These two quantities are defined through

$$E(z,t) = E_0 e^{i(\omega t - \beta z)} \text{ and}$$

$$k_0 = 2\pi / \lambda_0 ,$$

where E is a given electric-field component of the propagating wave, z is the propagation direction of the wave, λ_0 is the free-space wavelength, and ω is the radial frequency. For more information on optical wave propagation in dielectric media please refer to [5].

2.2.3 Racetrack Resonators and Vernier Operation

Racetrack resonators and Vernier operation have attracted significant attention in the literature. However, neither was employed in the present work as their drawbacks were found to outweigh their benefits.

Racetrack resonators are elongated rings created by introducing straight segments as shown in Fig 2.6. They are used to ease restrictions on the coupling regions. Coupling gaps in microring resonators can be narrower than 0.1 μm, which requires use of

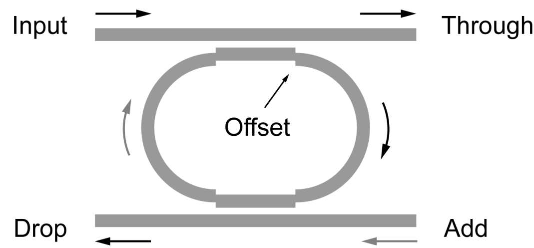

Fig. 2.6 Schematic of a racetrack-resonator add-drop filter. Straight segments are introduced to enhance coupling to the bus waveguides and allow wider coupling gaps than in microring resonators. Smooth curvature transitions or precise offsets need to be introduced to reduce loss resulting from mode mismatch between straight and bent waveguide segments.

expensive high-resolution lithography. For a given coupling coefficient, the coupling gaps are wider for racetracks than for rings as the coupling region is longer. This eases lithographic requirements. Nonetheless, the straight portions increase the path length in the resonator significantly and, in turn, reduce the FSR appreciably. To restore the FSR, a higher index-contrast must be used. A higher index contrast means stricter lithographic requirements and the racetrack's main benefit is partially lost. In addition, the optical mode in a bend is spatially offset in the waveguide towards the outer radius. Connecting a straight waveguide to a bent waveguide results in modal mismatch and, consecutively, in optical loss. To manage this problem, smooth transitions or accurate waveguide offsets need to be introduced.

Vernier operation can significantly enlarge the FSR of coupled-resonator filters. Enlarging the FSR enables a lower index-contrast to be used to achieve the required filter specifications. A lower index-contrast relaxes fabrication tolerances and reduces scattering losses. Each microring shows a comb of resonances. Two microrings with different radii (hence different FSR) in a series-coupled configuration will form a second-order filter with an enlarged effective FSR. As illustrated in Fig 2.7, the filter will drop power only at frequencies where both microrings are resonant (synchronous resonances).

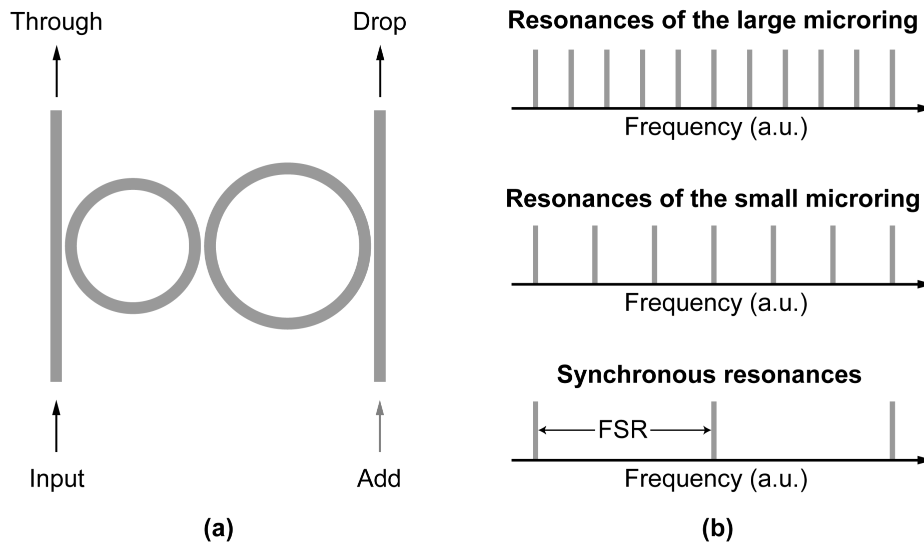

Fig. 2.7 (a) Schematic of a second-order microring-filter employing the Vernier effect. (b) Illustration of the Vernier effect. Power will be dropped only at frequencies where both microrings are resonant (synchronous resonances).

Superimposing the combs of resonances of both microrings, the effective FSR of the filter will be the distance between the spectral positions where resonances of both microrings overlap.

The Vernier effect was successfully employed to extend the FSR of drop-only filters [6] where the through response is not critical. However, it cannot be used for add-drop filters as it can introduce intolerable dispersion in the through port. At spectral positions where the input ring is resonant but not the output ring, the filter acts as a single ring connected only to the input bus-waveguide. Such a filter is called an all-pass filter. It can introduce loss and intolerable dispersion at the input-ring resonances that do not correspond to output-ring resonances.

Chapter 3

Fabricated Add-Drop Filters

3.1 INTRODUCTION

The present Chapter is an overview of the fabrication work done to realize the most advanced microring add-drop-filters reported in the literature. It allows demonstrating problems encountered in the fabrication of HIC filters and motivating Parts II and III of the Thesis. The reader is referred to later Chapters for detailed investigations of given problems. As mentioned in Chapter 1, microring resonators are a good example of high-index-contrast (HIC) microphotonic devices. In this Chapter we demonstrate fabrication problems that need to be addressed in HIC devices in general.

The filters were fabricated in four distinct phases that are reported in Sec. 3.4. An overview of the structures and of the fabrication process is presented in Sec. 3.2 and 3.3. Finally, a scheme allowing doubling the free-spectral-range (FSR) of microring filters is demonstrated in Sec. 3.5.

3.2 STRUCTURES OVERVIEW

Our goal was to create add-drop filters with a 40 GHz bandwidth, less than 0.1 dB ripple, at least 20 nm of FSR, and at least 30 dB of in-band extinction and out-of-band rejection

(assuming a 100 GHz channel spacing). Consequently, third-order filters were designed with a flat-top (Chebyshev) drop-port response using known synthesis techniques [4]. The coupling gaps were obtained using three-dimensional finite-difference-time-domain (3D FDTD) simulations [7]. The design strategy is reported in [8], [9] and [10]. For a detailed treatment of the filter design and numerical simulations, the reader is referred to [7] and [11].

A series-coupled third-order microring filter is shown schematically in Fig. 3.1. The waveguides are formed of a silicon-rich silicon-nitride (SiN) core, a silicon-oxide under-cladding, and an air top-cladding. The waveguides are designed monomode. Hence, they support a single TE-like (main *E* component horizontal) and a single TM-like (main *E* component vertical) mode only. The mode used in all microrings presented below is the TE-like mode. Polarization independence is addressed in Sec. 3.4.4. The waveguides are designed wide and flat

1. to reduce the field overlap at the sidewalls to lower scattering losses due to sidewall roughness and decrease the sensitivity of the effective index (and, hence, of microring resonant frequencies) to the waveguide width, and
2. to induce modal birefringence (effective-index difference between TE- and TM-like modes) to avoid waveguide-imperfections induced coupling between polarizations.

Designed filter dimensions are summarized in Table 3.1 for all fabricated third-order filters. Unless otherwise indicated, all refractive indices in the present work are reported for $\lambda_0 = 1.55\ \mu\text{m}$. FSR-doubling of microring filters was demonstrated on second-order filters described in Sec. 3.5.

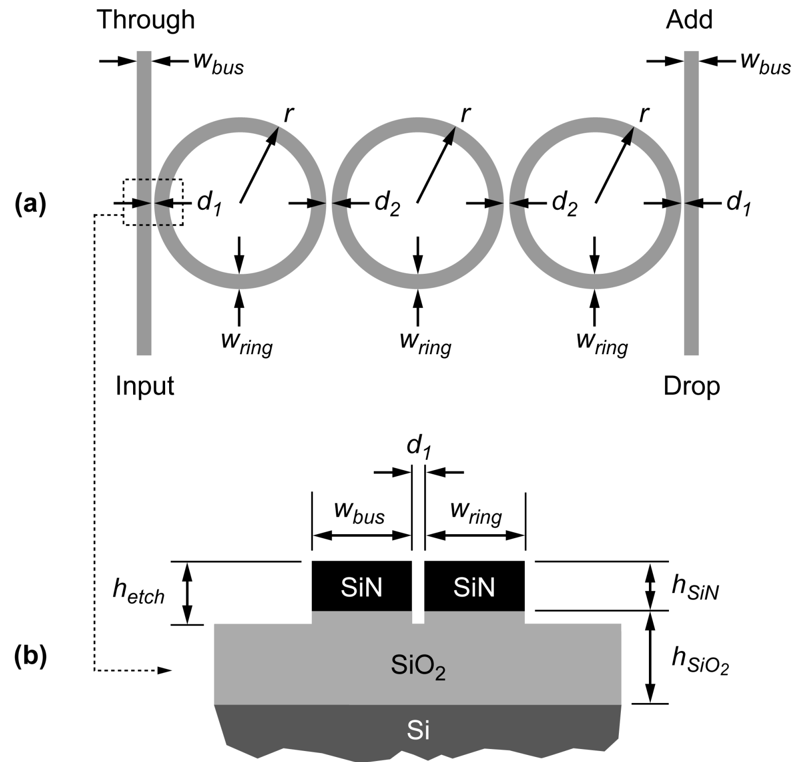

Fig. 3.1 Schematic of a series-coupled third-order microring filter. The microrings are designed identical. The actual parameters used are presented in Table 3.1. (a) Top view. (b) Cross-section of the waveguides at the bus-to-ring coupling region.

TABLE 3.1
DESIGNED THIRD-ORDER-FILTER PARAMETERS

Parameter	First Third-Order Filters	First Frequency-Matched Filters	Multistage Filters	Polarization Independent Filters
h_{SiN}	330 nm	400 nm	396 nm	420 nm
h_{SiO2}	2.5 μm	3 μm	3 μm	3 μm
h_{etch}	430 nm	500 nm	600 nm	520 nm
n_{SiN}	2.200	2.200	2.181	2.193
n_{SiO2}	1.445	1.455	1.455	1.455
w_{bus}	850 nm	804 nm	702 nm	600 nm
w_{ring}	1050 nm	804 nm	900 nm	876 nm
d_1	60 nm	102 nm	120 nm	162 nm
d_2	285 nm	492 nm	372 nm	396 nm
r	7265 nm	8004 nm	7998 nm	7998 nm

But for the first third-order filters, all lithographically defined dimensions were rounded to a 6 nm scanning-electron-beam-lithography step-size to ensure consistent discretization of patterns.

3.3 ONE-LAYER FABRICATION PROCESS

Fabrication of HIC microring resonators requires high-resolution lithography, strict dimensional control, and smooth sidewalls. Consequently, the fabrication process is based on direct-write scanning-electron-beam lithography (SEBL) and non-chemically-amplified resist.

A process diagram is shown in Fig. 3.2. First, a Si wafer is thermally oxidized to form a 2.5- to 3-μm-layer of SiO_2. Then, a 330- to 400-nm-layer of SiN is deposited by low-pressure chemical-vapor-deposition (LPCVD) in a vertical thermal reactor with a gas mixture of SiH_2Cl_2 and NH_3 in a 10 to 1 ratio. The resulting SiN shows low stress and is often referred to as low-stress nitride. The vertical thermal reactor provides excellent on-wafer uniformity and a repeatable wafer-to-wafer distribution of film thicknesses and

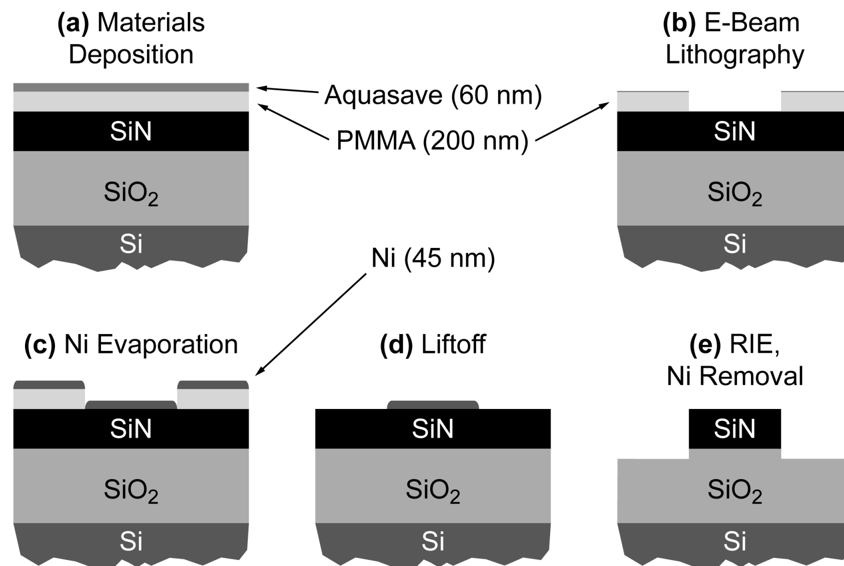

Fig. 3.2 Fabrication process overview (a) Initial multilayer formed of 3 μm of silicon oxide, 400 nm of silicon-rich silicon-nitride (SiN), 200 nm of poly-methyl-methacrylate (PMMA) and 60 nm of Aquasave [12]. (b) Scanning-electron-beam-lithography exposure, Aquasave removal, and PMMA development. (c) 45 nm Ni evaporation. (d) Liftoff. (e) Reactive-ion etching and Ni removal.

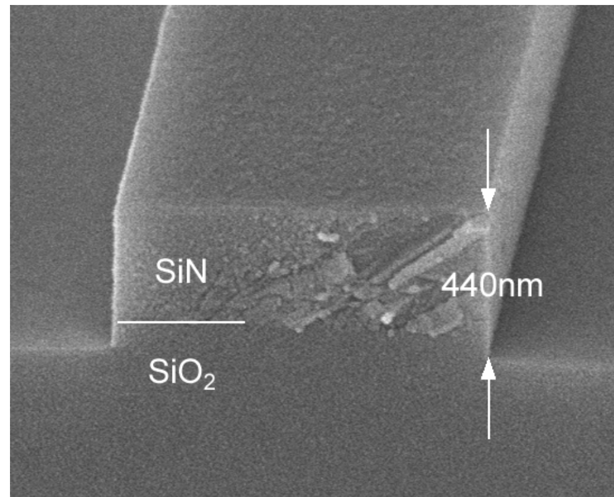

Fig. 3.3 Cross-section of a smooth SiN waveguide. The desired etching depth was 430 nm. A 10 nm etch depth accuracy is obtained by performing the RIE in several steps, between which the etch depth is measured with a profilometer.

indices of refraction. The most suitable wafer for device fabrication is selected from the batch by measuring the obtained thicknesses and indices of refraction with a spectroscopic ellipsometer. Next, 200 nm of poly-methyl-methacrylate (PMMA) and 60 nm of Aquasave are spun on. PMMA is a positive e-beam resist while Aquasave [12] is a water-soluble conductive polymer used to prevent charging during SEBL. The PMMA is exposed at 30 KeV using a Raith 150 SEBL system. The Aquasave is removed, and the PMMA developed. Next, a 45- to 50-nm-layer of Ni is evaporated on the structure, and a liftoff performed by removing the non-exposed PMMA. Using the Ni as a hardmask, the waveguides are defined by conventional reactive-ion-etching (RIE) with a gas mixture of CHF_3-O_2. To obtain an accurate etch depth, the RIE is performed in several steps, between which the etch depth is measured with a profilometer. Finally, the Ni is removed using a nitric-acid-based commercial wet Ni etchant and the sample prepared for optical characterization.

The fabrication process is optimized to reduce sidewall roughness as described in

Chapter 5. Moreover, strict dimensional control is achieved by process calibration as described in Chapter 8. The cross-section of a resulting fabricated waveguide is presented in Fig. 3.3. Using this process, ring-to-bus gaps as small as 50 nm were successfully fabricated with good repeatability. Note that the polarization-independent filters require a more complex two-layer fabrication process that will be presented in Sec. 3.4.4.

3.4 FABRICATED THIRD-ORDER FILTERS

3.4.1 First Third-Order Filters

The goal of the first third-order filters was to create a wide variety of structures to asses the partially optimized fabrication process and the initial designs. The filters were fabricated as described in Sec. 3.3. The designed dimensions are reported in Table 3.1. A fabricated filter along with the experimental layout is presented in Fig. 3.4. As a wide variety of filters were fabricated, the structures were only coarsely calibrated. Nevertheless, a 20 nm dimensional control was achieved. Detailed dimensional measurements are presented in Chapter 8.

The measured vertical waveguide parameters are reported in Table 3.2. The discrepancy between the designed and the employed SiN thickness is due to a problem with the optical characterization tool (single-angle narrow-spectral-band spectroscopic ellipsometer) used in the clean room to select the device wafer. More accurate measurements were obtained using a Sopra spectroscopic ellipsometer with multi-angle measurements and wide (400-2000 nm) spectral scans. Both the SiN and SiO_2 refractive indices were higher than expected. For SiN this is easily understood as the reactants are introduced in a strongly non-stoichiometric ratio to create a silicon-rich material. Hence, the material composition is sensitive to deposition parameters and the index is expected

to vary from batch to batch. For thermal oxidation of Si, however, it is usual to get variations in the film thickness but not in the refractive index. The refractive index offset was found to be repeatable and is most likely due to Si dopants that become part of the SiO_2 once the Si is oxidized.

The filter response is presented in Fig. 3.5. For the first time, a low drop loss (3dB) and a wide FSR (24 nm) were demonstrated in high-order HIC filters without using the Vernier effect. The drop loss was improved by 10 dB over previously reported wide-FSR

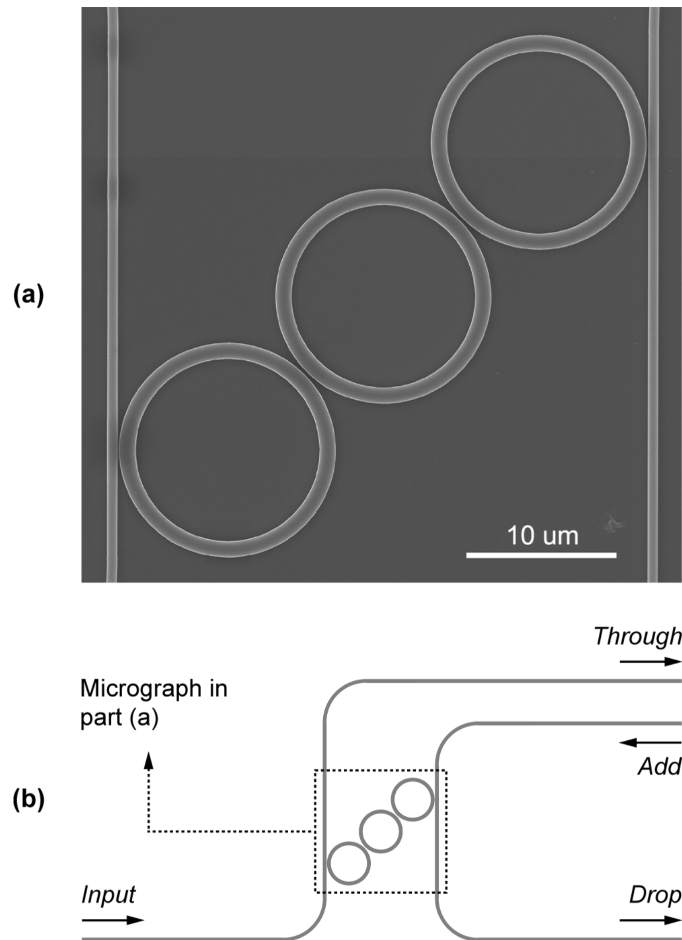

Fig. 3.4 Third-order add-drop filter based on series-coupled microring resonators. (a) Scanning-electron micrograph. (b) Schematic of the chip layout used in the experiment. To ensure a reliable drop-loss measurement, the drop and the through waveguides traverse equivalent paths.

TABLE 3.2
VERTICAL WAVEGUIDE PARAMETERS OF FIRST THIRD-ORDER FILTERS

Parameter	Designed	Measured
h_{SiN}	330 nm	314 ± 1 nm
n_{SiN}	2.200	2.217± 0.006
h_{SiO2}	2.50 μm	2.53 ± 0.01 μm
n_{SiO2}	1.445	1.455 ± 0.003
h_{etch}	430 nm	440 ± 10 nm

Layer thicknesses and indices of refraction were measured with a Sopra spectroscopic ellipsometer, while the etch depth was measured with a Dektak profilometer.

filters [13]. The FSR was improved by more than a factor of 2 over moderate-index-contrast filters with only a 2 dB penalty in the drop-loss [14].

Post-fabrication simulations were performed to understand the observed response of the fabricated third-order filter using the measured dimensions and refractive indices. Ring-ring and ring-bus coupling coefficients were calculated using 3D FDTD. A cylindrical mode solver yielded bend losses and ring effective and group indices. The ring resonant frequencies were chosen to fit the data. As seen in Fig. 3.5, the spectral response of the filter is matched to excellent agreement by the rigorous numerical simulations.

The FDTD simulations indicate that additional losses were present in each of the rings due primarily to coupling to a lossy higher-order transverse mode of the ring waveguide at the couplers. The waveguides support a single mode of each polarization when straight, but when bent regain the second-order TE mode as a leaky resonance with high bend loss. A higher-order mode can be tolerated if its loss is engineered to be high enough to ensure that it is not resonant and that no coupling to it from the fundamental mode is present. In our design, the bending loss of the second-order TE mode was sufficient to suppress its resonance but too low to forbid its excitation at the couplers by

the fundamental resonance. This excitation translates to coupler losses, which are higher in the outer rings since the ring-bus coupling is stronger than the ring-ring coupling. This coupler scattering is a significant loss mechanism. Coupler scattering and bend loss fully account for the observed 3 dB drop loss. Hence, scattering loss and material loss have no impact on the performance of the present filter. The propagation loss in straight waveguides was measured using the Fabry-Perot method. In short, the waveguide is considered as a Fabry-Perot resonator with the Fabry-Perot mirrors being formed of the reflections at the waveguide input and output facets. The Q of the resonator will be limited by propagation loss of the waveguide and the transmission at the waveguides facets. A propagation loss of 3.6 dB/cm was obtained. This loss was later found to be strongly under-estimated because of the strong sensitivity of the measurement to changes in the reflectivity of the waveguide facets. More accurate propagation loss measurements were obtained in analysis of later fabrication phases. An investigation of propagation loss in SiN waveguides is presented in Sec. 6.7.4.

The SEBL field covers a $100 \times 100\ \mu m$ area. Features larger than a single field require exposing multiple fields and moving the interferometrically-controlled SEBL stage between the field exposures. A field-stitching error with zero mean and 20 nm standard deviation is expected. In the present filters, a rotational error in the SEBL field calibration created a 30 nm mean offset of the bus waveguides every 100 μm. Numerical simulations indicate that such offsets result in a significant loss of 0.021 dB/junction or 2.1 dB/cm. This illustrates the sensitivity of HIC waveguides to any perturbation.

The spectral asymmetry, clear in the through-port response of Fig. 3.5, is indicative of unequal, symmetrically distributed resonance frequencies, with the central ring having a higher frequency than the outer rings by 22 GHz. The effect is partially explained by coupling-induced frequency shifting (CIFS) of resonators [15], a purely optical effect due

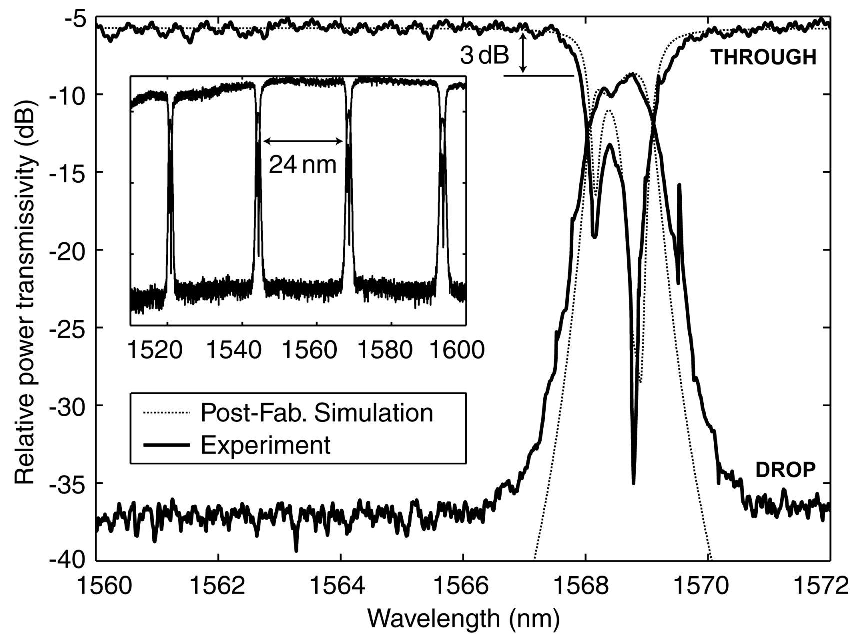

Fig. 3.5 Measured and simulated response of the first third-order microring filters. The spectral asymmetry is due to frequency mismatch of resonators and can be compensated. Input-to-drop loss is dominated by scattering at the 60-nm-wide ring-bus coupler gaps. The narrow peak on the right of the drop spectrum is a measurement artifact. The inset shows several resonances and the free-spectral-range. [Measurement by P.T. Rakich, simulations by M.R. Watts and M.A. Popovič]

to the index perturbations caused by adjacent ring and bus waveguides. The CIFS calculated by FDTD for the present filters is 43 GHz. Frequency shifts also result from dimensional variations in the rings due to e-beam proximity effects, SEBL discretization errors and other lithographic imperfections such as SEBL digital-to-analog converter errors. The frequency mismatch is corrected in later fabrication phases and the correction mechanism is thoroughly described in Chapter 9.

Despite accurate dimensional control at fabrication, the measured 88 GHz bandwidth was more than twice the intended 40 GHz bandwidth. Matching of post-fabrication simulation results and experimental data supports the validity of the simulations, and the discrepancy is attributed to the simple couple-mode-theory model used in the design.

Finally, a larger-than-intended passband ripple limited in-band (through-port) extinction to 9 dB instead of an intended 13 dB. The resonant frequency mismatch further reduced this to 7.5 dB.

3.4.2 First Frequency-Matched Filters

In the first third-order filters, the following three problems were identified:

1. inaccurate bandwidth,
2. coupler loss,
3. frequency mismatch of resonators.

In the second fabrication phase, these three problems were addressed. The bandwidth and the coupler loss were improved by using rigorous 3D FDTD simulation to redesign the waveguide cross-section and the coupler gaps [8]. The frequency mismatch was corrected by a deliberate increase of the SEBL dose on the middle microring. Such a dose increase results in a slightly wider middle-ring-waveguide and lowers the resonance frequency of the middle ring to match it to the outer rings. The frequency-matching technique is described in Chapter 9.

The filters were fabricated as described in Sec. 3.3. The process was properly calibrated to achieve strict dimensional control as described in Chapter 8. Dimensional measurements are reported in Sec. 8.3 and Sec. 9.6. The SEBL writing strategy was optimized to achieve smooth rings with a uniform ring-waveguide width. The SEBL writing strategy is addressed in Chapter 7.

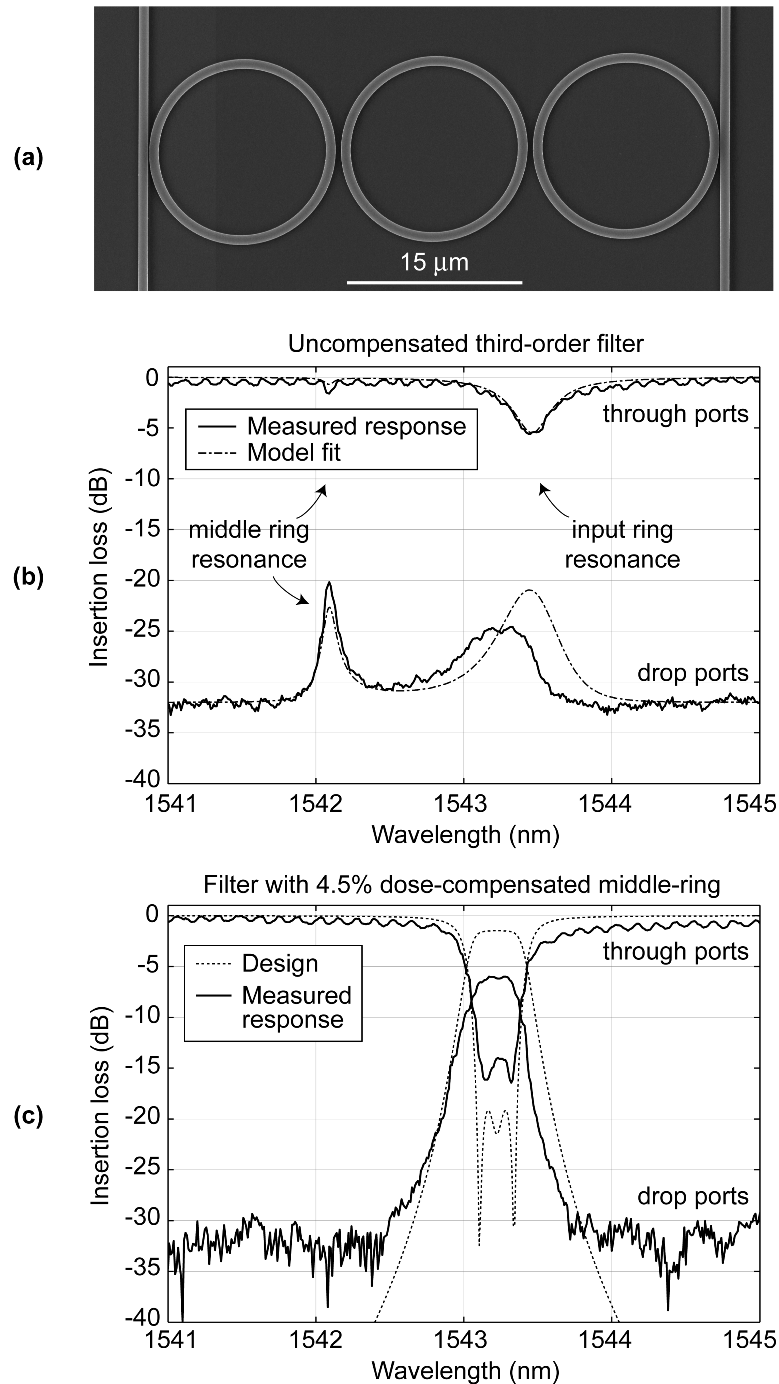

Fig. 3.6 (a) Micrograph of a frequency-matched filter. (b) Measured and fit spectral response of a filter without dose-compensation. A 170 GHz mismatch is observed. (c) Filter that is frequency-matched to better than 1 GHz as a result of an intentional SEBL dose increase of 4.5% on the middle ring. [Measurement by P.T. Rakich, simulations by M.A. Popovič and M.R. Watts]

A micrograph of a frequency-matched filter is shown in Fig. 3.6a. The spectral responses obtained with and without SEBL dose compensation are shown in Fig. 3.6c and Fig. 3.6b, respectively. The uncompensated filter shows a frequency mismatch of 170 GHz with 38 GHz attributed to CIFS (from 3D FDTD simulations). This is much higher than the 22 GHz frequency mismatch in the first third-order filters. The difference is mainly due to

1. uniform SEBL discretization of patterns obtained in the present filters by choosing all dimensions to be multiples of the SEBL step size (discretization errors may have introduced a significant negative frequency shift component in the first third-order filters), and to
2. a difference in ring-waveguide width between the two designs, making the resonant frequency of the present filters twice as sensitive to waveguide-width variations as the first third-order filters.

The three microring resonators of the best compensated filter are frequency matched to better than 1 GHz (5 ppm). This allowed the in-band extinction to reach 14 dB, the highest reported in the literature. Since the resonance frequency of these microrings changes by about 40 GHz for a change of 1 nm in the average ring-waveguide width, the average waveguide-widths of the three microrings are matched to better than 26 pm to a desired width-offset needed to compensate for the CIFS. Obtaining such relative dimensional control is addressed in Chapter 9. These filters were the first frequency-matched microring filters reported in the literature.

The main downside of the present filters is the high drop-loss (5-6 dB). From the filter responses, the propagation loss is estimated to 10-15 dB/cm. This is the main source of loss in the filters as bending and coupler loss are responsible for only 1.5 dB of drop loss. At first, the higher than expected propagation loss was attributed to an imperfect Ni

TABLE 3.3
WAVEGUIDE VERTICAL PARAMETERS OF
FIRST FREQUENCY-MATCHED FILTERS

Parameter	Designed	Measured
h_{SiN}	400 nm	406 ± 1 nm
n_{SiN}	2.200	2.189 ± 0.003
h_{etch}	500 nm	510 ± 10 nm

SiN thickness and index of refraction were measured with a Sopra spectroscopic ellipsometer, while the etch depth was measured with a Dektak profilometer.

liftoff. The Ni evaporation produced a thicker film (62 nm) than expected (45 nm) and a coarse microstructure, which amplified the line-edge-roughness of the Ni hardmask and translated to larger sidewall roughness and higher than expected scattering losses. To reduce scattering losses in later fabrication phases, the process was carefully re-optimized to minimize roughness. The optimization strategy and resulting roughness are reported in Chapter 5. Nonetheless, the scattering loss analysis of Chapter 6 and later experiments have shown that the propagation loss should rather be attributed to SiN material loss. This is discussed in Sec. 6.7.4.

The 1 dB bandwidth of the frequency-matched filters is 30 GHz. The designed filter bandwidth is 38 GHz. The discrepancy is attributed to rounding of the filter response due to propagation loss and to lower than expected coupling coefficients. The later are mainly due to a slight offset of the actual SiN refractive index and thickness from design values. The designed and measured vertical dimensions are shown in Table 3.3. The SiN layer of the device wafer cannot be directly characterized prior to fabrication as the adequate characterization tool (Sopra ellipsometer) is not located in a clean environment. The device wafer is selected from a deposition batch by accurately characterizing monitor wafers placed on the edges of the stack and interpolating the SiN thickness and index of refraction on the remaining wafers. Variations in the deposition rate and film composition

does not allow for accurate control of thickness and refractive index at MIT. In later fabrication phases, the design was trimmed to the interpolated SiN index and thickness of a chosen device wafer prior to fabrication.

3.4.3 Multistage Filters

Add-drop filters have to provide an in-band extinction of at least 30 dB. Even if a third-order filter were perfectly fabricated, its in-band extinction would only reach about 20 dB. To obtain the required extinction with a single filter, a filter of higher order than third would be required. When the order of a filter is increased, the fabrication tolerances become more stringent. Another possible approach to reach the required in-band

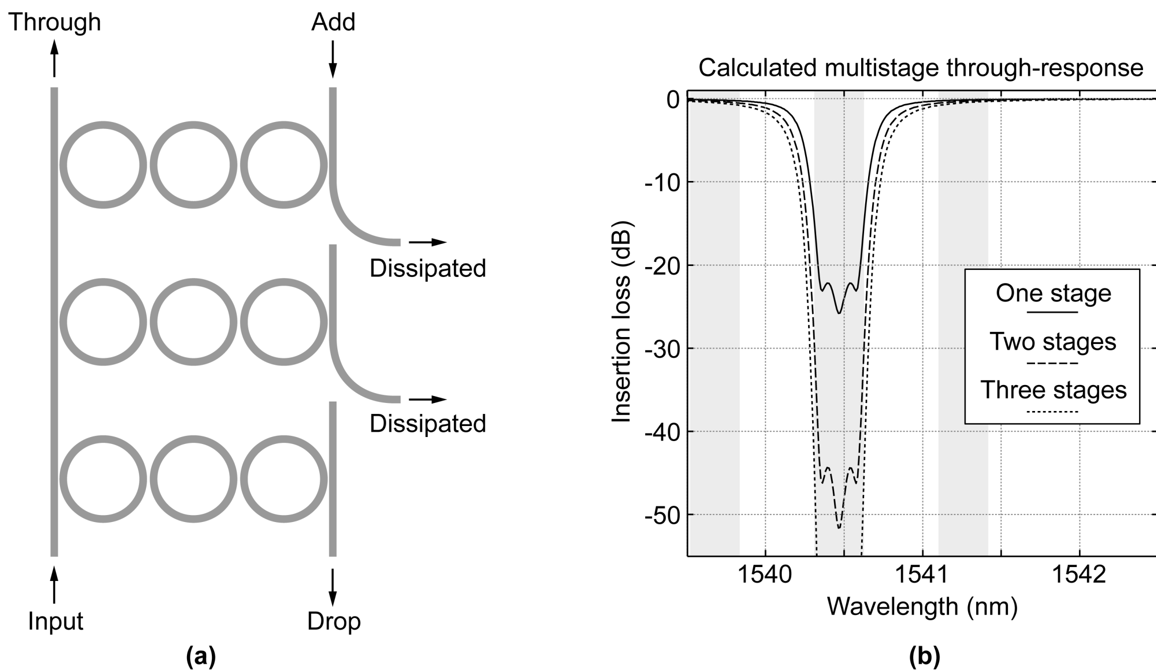

Fig. 3.7 Cascaded third-order filters used to enhance the in-band extinction. (a) Three-stage third-order filter. The power dropped at the second and third stage is dissipated. (b) Calculated through-port spectral response of one-, two-, and three-stage filters. The in-band extinction of a multistage filter is the sum (in dB scale) of the in-band extinctions of the individual stages forming the filter. [Scheme proposed by M.A. Popovič]

extinction is to cascade third-order filters as shown on Fig. 3.7. Such a multistage filter introduces new degrees of freedom in filter design and allows decoupling the design of the drop-port response from the design of the through-port response. Consequently, the through-port response can be improved without increasing the drop-loss and making fabrication tolerances more stringent. The in-band extinction of a multistage filter is given by the sum (in dB scale) of the in-band extinctions of the individual stages forming the multistage filter.

The main fabrication challenge in cascading filters is to have all stages spectrally

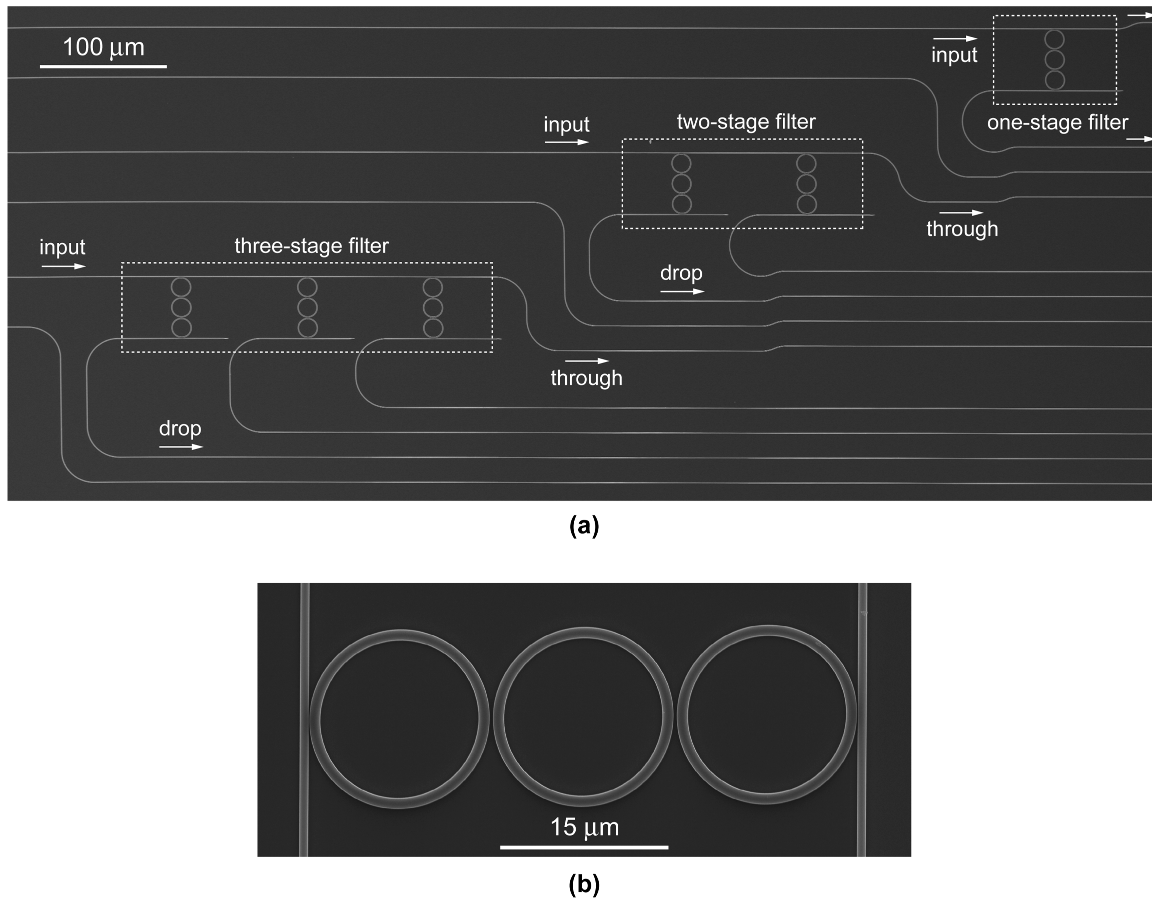

Fig. 3.8 Fabricated multistage filters. (a) Electron micrograph of one, two- and three-stage filters showing the layout used in the experiment. (b) Electron micrograph of a single stage.

aligned to within a few GHz. Thus, the stages must be kept spatially close to one another to prevent resonant frequency variations due to non-uniformity in the SiN thickness, SiN index, PMMA thickness, and development rate. Moreover, the stages need to be e-beam written with minimal time delays between the stages to avoid drift of the e-beam current in between stage exposures (a dose difference would result in a frequency difference). However, it would be ill-advised to put all stages in the same SEBL field. Rather, the stages are exposed in consecutive SEBL fields and positioned in the center of each field to avoid spectrally misaligning the filters by SEBL intra-field distortions.

The filters were fabricated as described in Sec. 3.3. The fabrication process was optimized to minimize sidewall roughness as presented in Chapter 5. The filters were re-designed for the SiN index and thickness of a selected device wafer. An asymmetric coupler design reduced coupler scattering significantly when compared to the first frequency-matched filters. This provided for a better tolerance of the filter spectral response to propagation loss. The designed filter parameters are presented in Table 3.1.

A micrograph of fabricated one-, two-, and three-stage third-order filters is presented in Fig. 3.8. The spectral response of a one- and two-stage filter is presented in Fig. 3.9. The dose-compensated one-stage filter is frequency-matched to better than 2 GHz and shows an in-band extinction of 17.5 dB, the highest reported in literature (the previously highest extinction was that of the first frequency-matched filters). The average ring-waveguide widths are matched to better than 68 pm to a desired width-offset within a single stage. The filter 1 dB bandwidth is 42 GHz, only 2 GHz off the designed 40 GHz bandwidth. The drop loss was improved to 2.5 dB as a result of the asymmetric coupler design. The propagation loss remained high near 10 dB/cm despite smoother waveguide-sidewalls. Roughness measurements were performed using the method presented in Chapter 4 and are reported in Sec. 5.4. The continuation of the high propagation loss

despite improvement of sidewall roughness suggests that scattering losses are not the main source of loss. This was confirmed by the analysis of Chapter 6 and is addressed in Sec 6.7.4.

The in-band extinctions of two- and three-stage filters are limited by a -30 dB

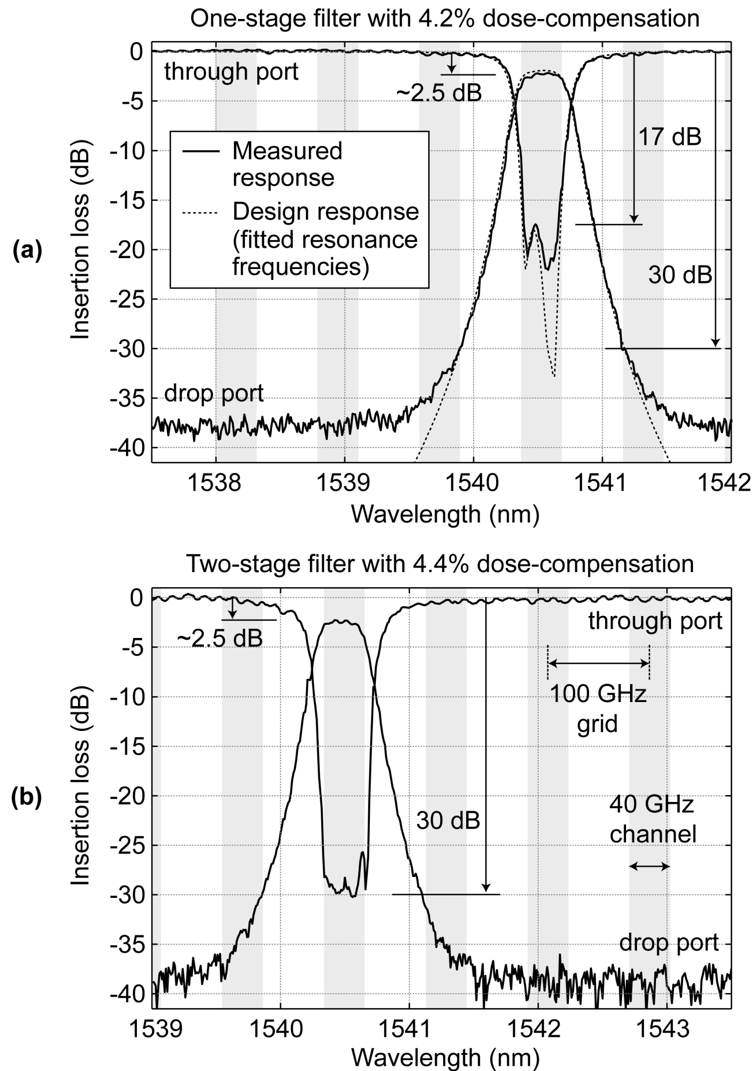

Fig. 3.9 Spectral response of (a) a one-stage filter and (b) a two-stage filters. The in-band extinction of the two- and three-stage filters is characterization-limited to 30 dB by the laser line of the tunable laser used for characterization. The noise floor in the drop-ports is not limited by the laser line and reaches -40 dB. [Measurement by P.T. Rakich and L. Socci, design by M.A. Popovič, and required FDTD simulations by M.R. Watts]

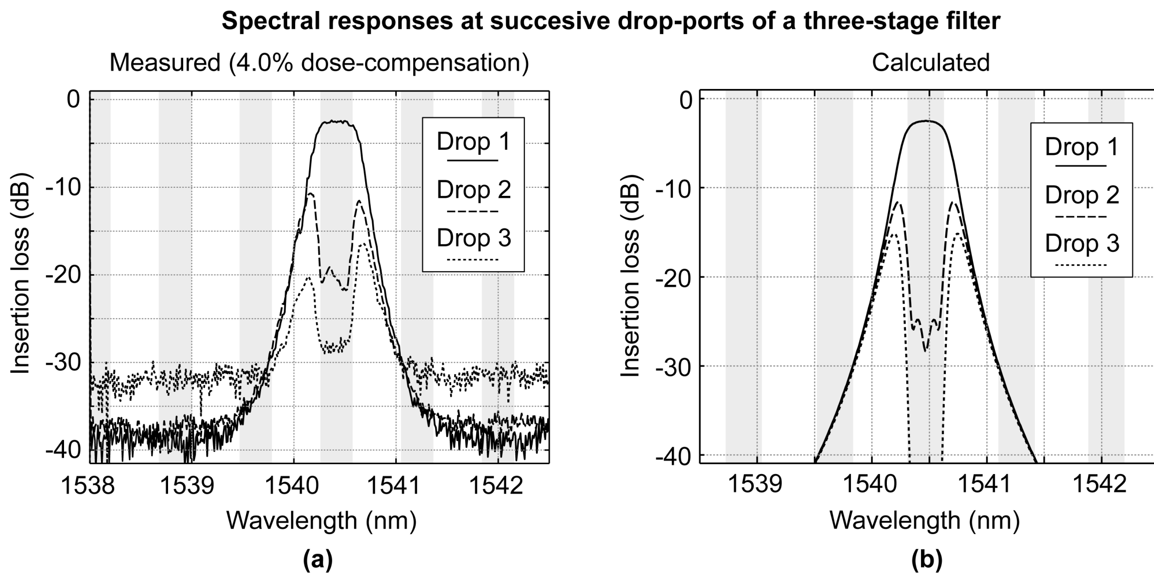

Fig. 3.10 (a) Measured and (b) calculated spectral responses at drop-ports of successive stages of a three-stage filter. The measured spectral responses are consistent with the calculated ones. The stages are spectrally aligned within 2-5 GHz. The higher noise-floor in the third drop-port measured is most probably due to a problem with the end-facet at the output of the chip. [Measurement by P.T. Rakich and L. Socci, calculation by M.A. Popovič]

characterization noise-floor most likely due to the laser line of the tunable laser used at characterization. This noise floor does not allow appropriate characterization of the through-port response but is sufficient to demonstrate that the in-band extinction reaches the required 30 dB. Note that the drop-port noise-floor is not laser-line limited and reaches about -40 dB.

The stages were spectrally aligned within 2 to 5 GHz. For a three-stage filter, this indicates that the average ring-waveguide widths of all 9 rings are matched to the ideal to better than 0.16 nm. The drop-port responses of the three consecutive stages of a three-stage filter are shown in Fig. 3.10. The responses are well aligned, symmetric, and follow the theoretically predicted shape. Even if a higher than 30 dB extinction is not desired, a triple-stage filter may still be found desirable. It relaxes fabrication tolerances by

allowing a wide range of dose-compensation to provide the required 30 dB extinction. This is further addressed in Chapter 9.

3.4.4 Polarization-Independent Filters

3.4.4.1 Integrated Polarization Diversity

All microring filters presented above work for the TE polarization only (main *E* component in the plane of the substrate). However, the polarization state in an optical fiber is random and both polarizations need to be handled equally. Polarization independent HIC filters, showing identical spectral responses for TE and TM polarizations, are not achievable in practice as they require control of dimensions and indices of refraction that may not be available for years to come. To achieve polarization-independent operation in HIC filters, we turn instead towards an integrated polarization diversity scheme [7,16]. As presented in Fig. 3.11, the polarization is first split in its TE and TM components. Then, the TM is rotated to become TE and both arms go through identical copies of the same filters. Finally, the non-rotated TE is rotated to become TM and the two arms are combined near the output of the chip. In this way, a polarization-

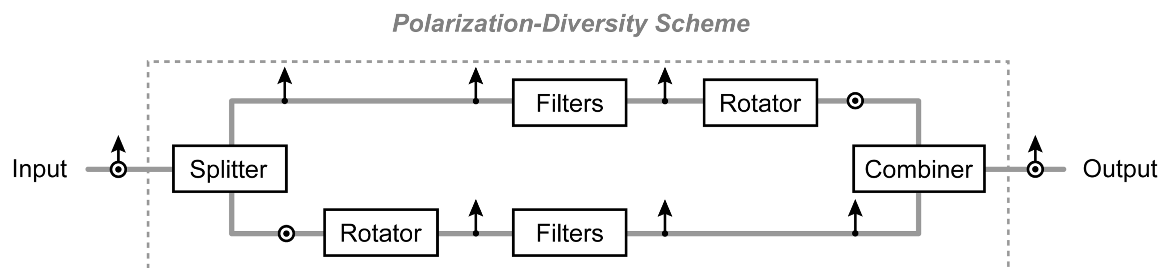

Fig. 3.11 Integrated polarization-diversity scheme allowing for polarization-independent optical chips built from polarization-dependent components. The input polarization is split in its TE and TM components. The TM is then rotated to become TE and both arms go through identical optical elements. The non-rotated TE is rotated to become TM and the two polarizations are combined at the output. [Scheme by M.R. Watts and H.A. Haus]

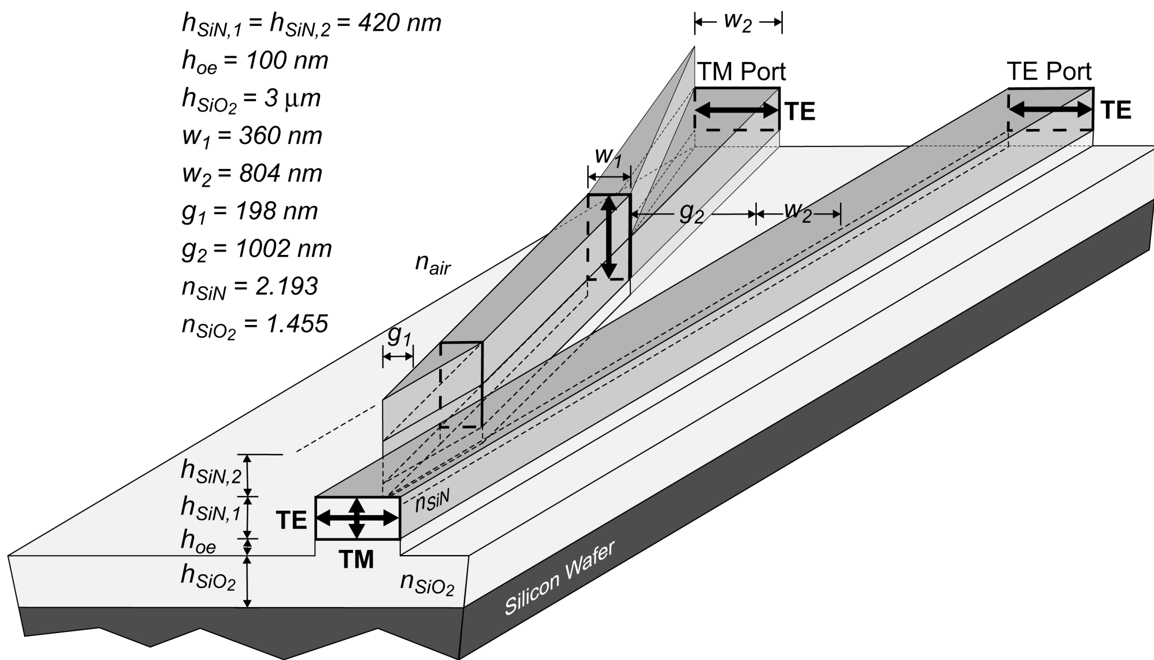

Fig. 3.12 Integrated polarization splitter and rotator. The structure can be anywhere between 300- to 600-µm-long. A longer structure allows for more relaxed fabrication tolerances. The design parameters are reported in the upper left. [Design by M.R. Watts]

independent optical chip can be formed from polarization-dependent optical elements. The rotation of the TE into TM at the end of the chip is required to avoid creating an interferometer between the two polarizations and to have perfectly balanced arms. The combiner is simply a splitter used in reversed direction.

The needed integrated polarization splitters and rotators (PSR) were designed employing adiabatic mode evolution [7, 17, 18]. In other words, there is no mode coupling in the structure. Instead, a single mode is used for each polarization. The mode is slowly transformed to achieve polarization splitting and rotating. This approach makes the PSR tolerant to fabrication errors. The PSR design is shown in Fig. 3.12. To ensure appropriate characterization of the device, polarization-independent couplers were designed and are presented in Fig. 3.13.

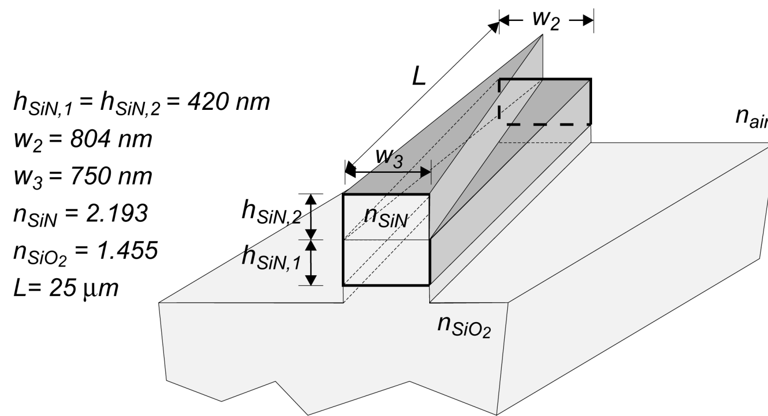

Fig. 3.13 Polarization-independent fiber-to-chip coupler required for polarization-independent operation. The initial waveguide cross-section allows for equal coupling efficiency of the fundamental TE- and TM-like modes. The waveguide is initially multimode but any initial higher-order mode is radiated at the taper. [Design by M.R. Watts]

3.4.4.2 Two-Layer Fabrication Process

The PSR is a two-layer structure. The lower layer is shared with the microring filters. To simplify the fabrication process, we proposed an innovative multilayer processing approach depicted in Fig. 3.14 [19]. First, the full SiN thickness of the two layers is deposited. Then, the top-layer pattern is exposed and the pattern transferred into a Cr hardmask by liftoff. Next, the bottom-layer pattern is exposed and the pattern transferred into a Ni hardmask by liftoff. The bottom-layer exposure is aligned to the top-layer pattern registered in the Cr hardmask. The structure is RIE etched halfway, the Ni hardmask removed, and the structure RIE etched again. Finally, the Cr hardmask is removed and the samples are prepared for optical characterization.

The RIE is done iteratively as described in Sec. 3.3. However, a gas mixture of CHF_3-O_2 in a 16-to-4 sccm ratio is used (16-to-3 ratio used in the one-layer process) to prioritize vertical sidewalls in the high-aspect-ratio structures over sidewall smoothness.

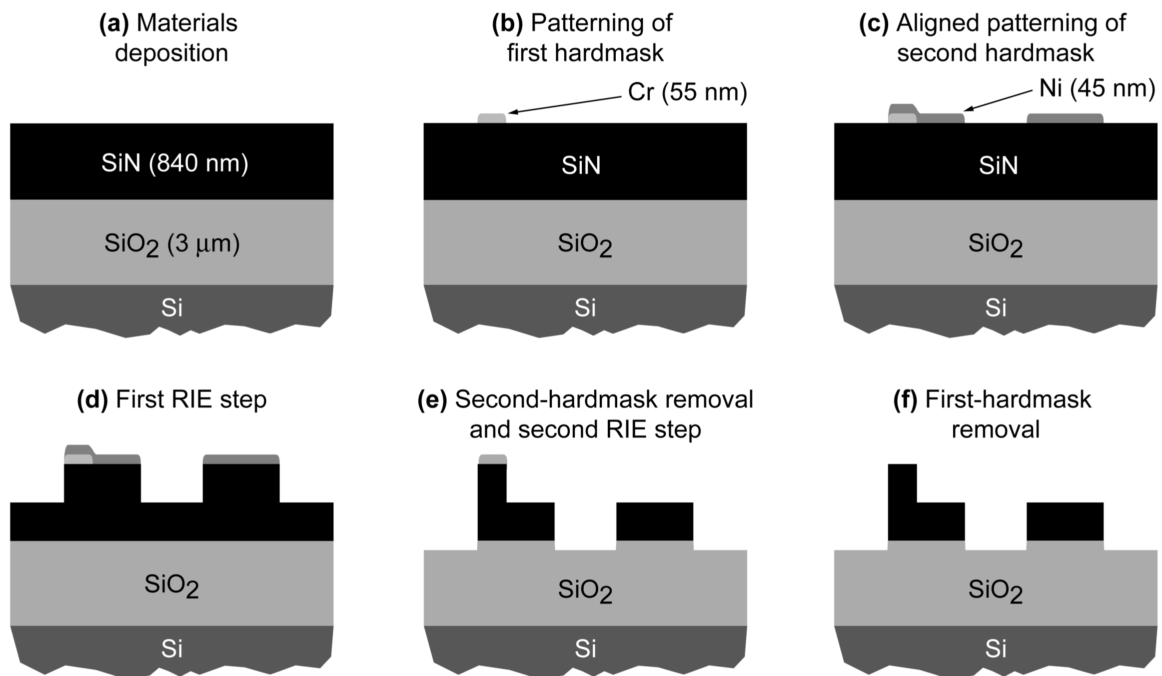

Fig. 3.14 Novel multilayer fabrication process used for the polarization independent add-drop-filters. (a) The full SiN thickness is deposited by LPCVD. (b) The pattern of the top layer is registered into a Cr hardmask using e-beam lithography and liftoff. (c) The pattern of the bottom layer (layer of the filters) is registered into a Ni hardmask using aligned e-beam lithography and liftoff. (d) The first RIE step defines the height of the bottom layer. (e) The second RIE step defines the height of the top and bottom layer. (f) The remaining Cr hardmask is removed.

The first etch defines the height of the bottom layer while the second etch defines the height of the top layer. Hence, the first etch must take into account the required over-etch into the SiO_2 and the etch rate difference between the SiN and the SiO_2 during the second etch. The second etch is done at reduced bias (300 V instead of 500 V) until the SiO_2 boundary was reached to avoid erosion of waveguide corners in the bottom layer that is transferred down without a mask. When transferred down without a mask, the structure width is thinned down by up to 100 nm. Each sidewall is moved inwards horizontally by up to 1 nm for every 10 nm etched vertically. This reduces the effective resolution on the bottom layer by the amount of thinning encountered. For this reason the filter coupling

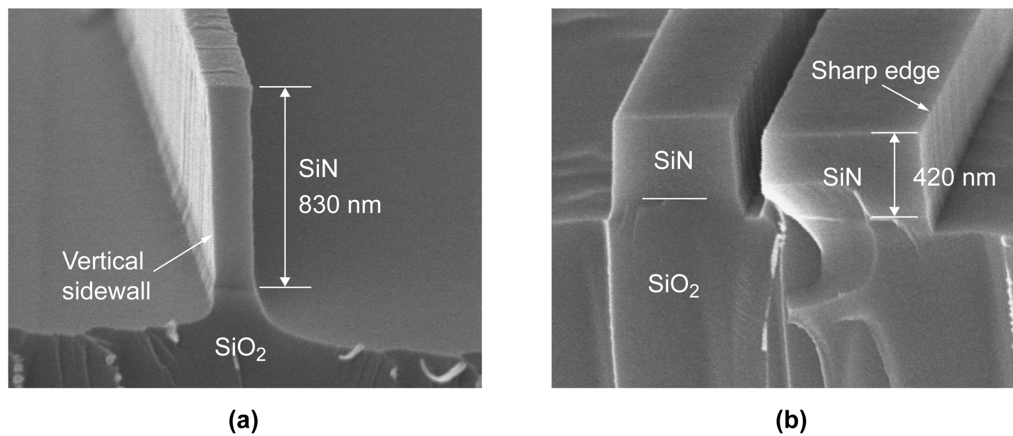

Fig. 3.15 Electron micrographs of waveguide cross-sections obtained using the fabrication process presented in Fig. 3.14. (a) Tall waveguide spanning the top and bottom layer of the structure. (b) Waveguide on the bottom layer of the structure. Sharp edges are obtained in bottom-layer waveguide by reducing the RIE power at the second RIE step, when the bottom layer is transferred down without a mask. Sidewall roughness is worse in these micrographs than in Fig. 3.2 as the RIE was optimized for vertical sidewalls and not sidewall smoothness. In addition, the roughness on the tall waveguide is worse than on the bottom-layer waveguide as ultrasonic agitation is used for Cr liftoff. This is addressed in Chapter 5.

region was redesigned to enlarge the coupling gap to 162 nm. Moreover, the two layers need to be carefully and independently optimized and dimensionally calibrated, as described in Chapters 5 and 8, for the wide range of dimensions needed (70 to 3000 nm).

The minimum feature size used was 70 nm. Below it, the 940-nm-tall waveguides (aspect ratio of 13.5-to-1) were mechanically unstable during wet processing. Cross-sections of resulting etched structures are presented in Fig. 3.15. The SEBL alignment procedure enables alignment accuracy with standard deviation of 20 nm or better. It is described in Appendix I.

The Ni hardmask can be removed without damaging the Cr hardmask by using a nitric-acid based commercial wet etchant (Transene TFB). The Cr hardmask is stripped at the end of the process with a perchloric-acid based commercial wet-etchant (Cyantek CR-7). The hardmask-material order is important as Cr cannot be easily removed without

damaging Ni.

This novel multilayer processing is the only way the PSR structures can be fabricated at MIT as cleanliness requirements do not allow SEBL processed samples to be re-inserted into the vertical thermal-reactor for further LPCVD deposition of SiN that would be required in standard multilayer processing.

3.4.4.3 Fabricated Polarization-Independent Filters

The goal was to demonstrate a polarization independent add-drop filter with full add and drop functionality and the spectral requirements presented in Sec. 3.2. To obtain 30 dB of in-band extinction in the resulting add-drop filter, all integrated components need to be designed to reduce all possible crosstalk between polarizations to below -30 dB. In fact, power in the TM-like mode in the input bus-waveguide of the microring filters will not be dropped by the filter and will act as noise in the through-port limiting the in-band-extinction.

Three-stage third-order filters were used for each polarization to allow a wide-range of dose compensation to provide the required 30 dB extinction. All the 18 microrings producing the two multistage filters must resonate at the same frequency for the filter to work optimally. The filter parameters are reported in Table 3.1. To make the PSR more tolerant to fabrication errors, a second splitter was added after the rotator to clean up any TM left after polarization rotation.

The full add-drop functionality required use of waveguide crossings. These were designed as $150 \times 150\,\mu\text{m}$ crosses (as seen in Fig. 3.16b). The waveguide width was tapered from the bus-waveguide width at the edges of the crosses to a width of 3 μm near the center of crosses. At 3 μm, the waveguides are multimode. Nonetheless, if there are no major perturbations, such as bends, the fundamental mode will not couple to higher

order modes and will be restored without significant loss after the waveguide is tapered down. Near the center of the crosses, the field overlap of the fundamental mode at the waveguide sidewalls is small so the crossing waveguides do not act to one another as a significant perturbation that could result in loss or crosstalk.

A schematic of the layout is presented in Fig. 3.16 with an optical micrograph of the crossings and the multistage filters. The layout exhibits two-fold symmetry. To minimize frequency variations between the filters, all stages are centered on consecutively written SEBL fields as discussed above in Sec. 3.4.3.

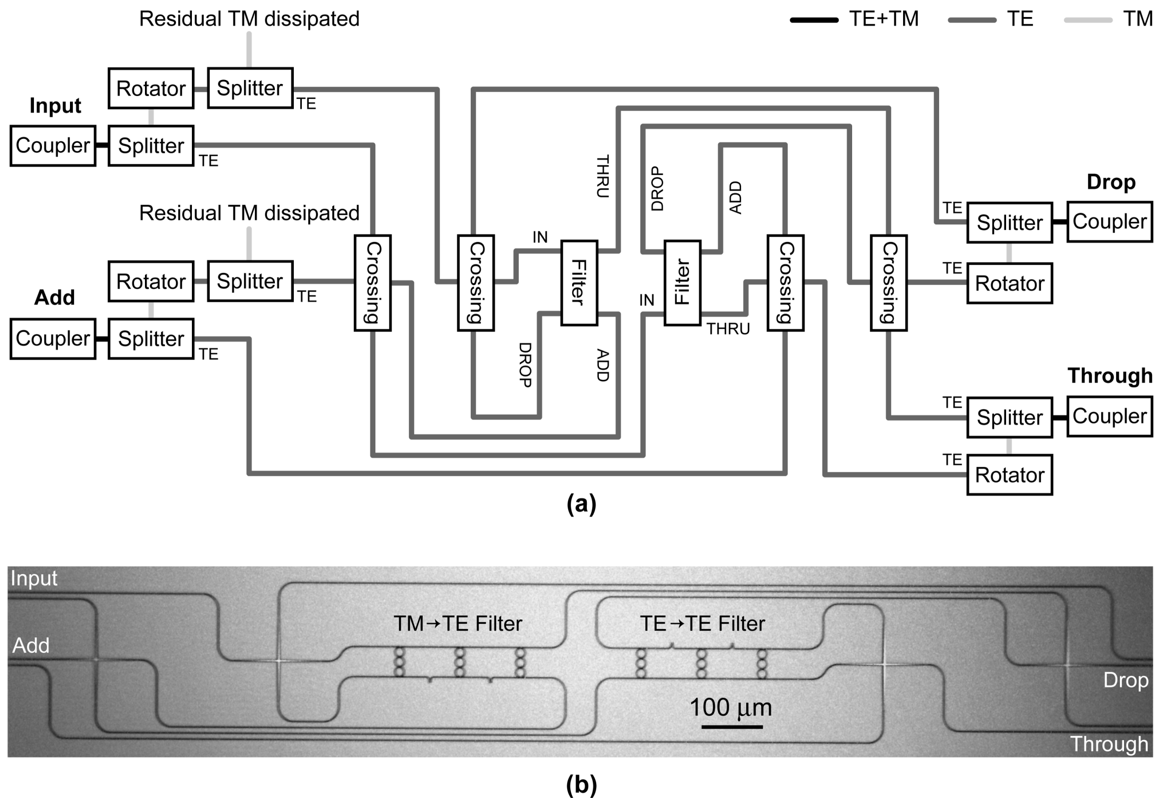

Fig. 3.16 (a) Schematic of the polarization-independent add-drop filter. The structure shows two-fold symmetry but for additional splitters at the input. These were included to ensure appropriate polarization control with relaxed rotator-fabrication tolerances. (b) Optical micrograph of the central part of the structure. Couplers and polarization splitters and rotators are not shown in the micrograph.

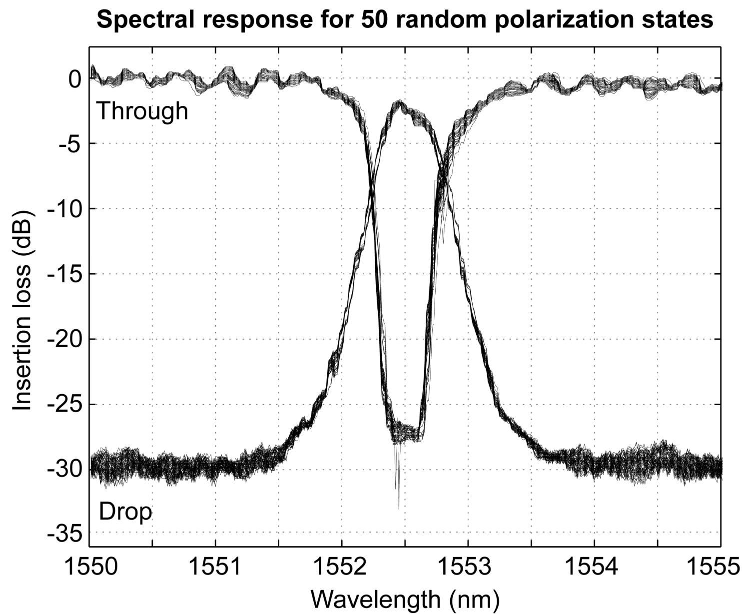

Fig. 3.17 Spectral response of a polarization independent add-drop filter for 50 random polarizations. Most of the polarization dependent loss (power variation) is believed to be due to the characterization setup. The in-band extinction is limited by the laser line of the tunable laser used at characterization. It is believed to reach at least 35 dB. The 6 stages forming the two filters acting on the two polarizations show excellent spectral alignment [Measurement by P.T. Rakich and L. Socci.]

Preliminary measured spectral responses are presented in Fig. 3.17. Polarization independent operation is demonstrated. The two multistage filters handling the two polarizations show excellent spectral alignment. The drop loss is below 3 dB. The transmitted power variations with polarization, also called polarization dependent loss (PDL), are below 1 dB. In Fig. 3.17, the in-band extinction and the PDL are believed to be limited by the characterization setup. A PDL not exceeding 0.5 dB is desired in optical networks. As for the in-band extinction, independent measurements have shown it reaches at least 35 dB.

At fabrication, the Cr evaporation resulted in a 71-nm-thick film instead of the 55-nm-thick film desired. This hindered the Cr liftoff on the smallest features and made them discontinuous. As a result, the PSR performance was worse than expected

(polarization control of ~20 dB instead of the expected ~30 dB). An insufficient polarization control will hinder the in-band extinction of the filters as the TM polarization will act as a noise floor. However, as the system was significantly over-designed, the filter performance reached the required specifications. Note that the crosstalk between polarizations is enhanced at the output of the chip. As long as there is no polarization conversion in the optical chip between the end of the input PSRs and the beginning of the output PSRs, the optical chip will exhibit a crosstalk between polarizations that is twice as small (twice as big a number in dB scale) as it is in an isolated PSR. By reciprocity, the output PSRs reject any TM in the output waveguides at the input of the output PSRs doubling the polarization control of the optical chip and, in turn, the achievable in-band extinction.

3.4.5 Summary

In Sec 3.4, we have presented the most advanced microring add-drop filters reported in the literature. Our progress is summarized in Table 3.4, where key indicators of filter performance are presented.

The drop-loss is a function of the internal losses of the resonators. When the filter is well designed to avoid coupler loss and bending loss, the waveguide propagation loss will

TABLE 3.4
PERFORMANCE OF POLARIZATION DEPENDENT THIRD-ORDER-FILTERS

Filter	Drop Loss	In-Band Extinction	Bandwidth
Required specifications	< 3 dB	> 30 dB	40 GHz
First third-order filters	3 dB	7.5 dB	88 GHz
First frequency-matched filters	5-6 dB	14 dB	30 GHz
Multistage filters (one-stage)	2.5 dB	17.5 dB	42 GHz
Multistage filters (two-stage)	2.5 dB	> 30 dB	42 GHz

be the main source of loss. Thus, understanding the source of propagation loss is of great importance to reduce the internal losses in resonators. This allows one to reduce drop-loss and to obtain the high-Q resonators required for narrow-bandwidth filters. In HIC waveguides, propagation loss is often limited by scattering losses due to sidewall roughness. This is addressed in Part II where roughness is characterized and optimized, and the induced optical loss is calculated.

In Part III, lithographic-pattern accuracy is considered. The filter-bandwidth accuracy depends on the refractive-index control and on the absolute dimensional-control. The filter in-band extinction is limited by the relative dimensional-control between resonators. As demonstrated above, fabrication of high-performance HIC devices requires strict absolute and relative dimensional controls. These are addressed in Chapters 8 and 9, respectively.

3.5 FSR-DOUBLED FILTERS

All third-order filters presented above show either a 20 or a 24 nm FSR. This is short of the 30 nm FSR desired. The FSR could be improved to some extent by changing the cross-section of the ring-waveguides. Tall waveguides show smaller bending loss than flat waveguides allowing for smaller resonators and wider FSRs. However, tall waveguides are more sensitive to width variations making the resonant-frequency control more difficult. Alternatively, a higher-index waveguide-core could be used. Again, the bending loss would be reduced but scattering losses due to sidewall roughness would increase and the resonant frequencies would be more difficult to control. In general, the higher the FSR of a resonator is, the more difficult its resonant frequency is to control.

In this section, we demonstrate an interferometric coupling scheme allowing doubling the FSR of a microring filter. The FSR of the microring resonators is left

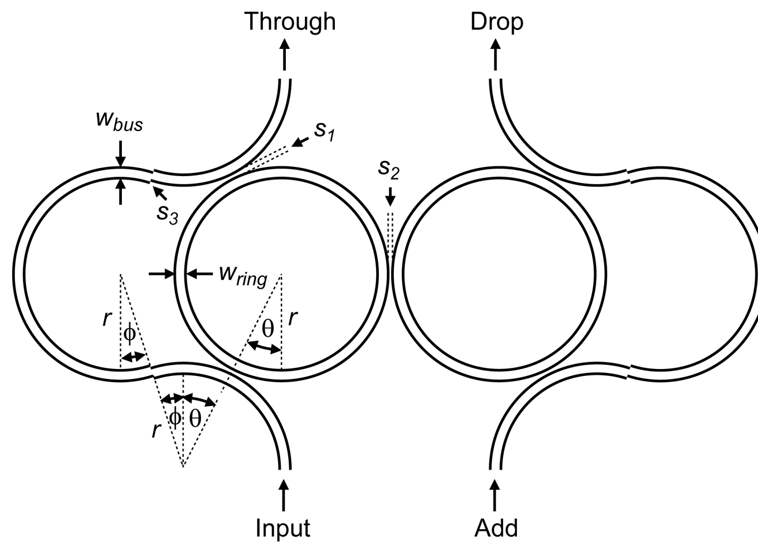

Fig. 3.18 Schematic of a second-order microring filter with doubled FSR. The interferometric coupling scheme eliminates power coupled to the microrings at every other microring resonance effectively doubling the FSR of the filter. A 48-nm-offset is introduced in the outer arms to enhance mode matching at the curvature change. [Design by M.R. Watts]

unchanged but the bus-to-ring coupling is canceled out by the interferometric coupling scheme at every other microring resonance effectively doubling the FSR of the microring filter. The FSR doubling can be applied to any of the microring filters reported in Sec. 3.4.

A schematic of a second-order microring-filter with doubled FSR is presented in Fig. 3.18. Designed filter parameters are reported in Table 3.5. The optical path length between the coupling gaps must be twice as long in the outer arms as it is in the outer part

TABLE 3.5
DESIGNED FSR-DOUBLED FILTER PARAMETERS

h_{SiN}	n_{SiN}	h_{etch}	$w_{bus} = w_{ring}$	s_1	s_2	s_3	r	θ	ϕ
396 nm	2.181	600 nm	900 nm	146 nm	312 nm	48 nm	8004 nm	26.9°	18.1°

Lithographically defined dimensions were rounded to fit on the 6 nm scanning-electron-beam-lithography step-size grid to ensure consistent discretization of patterns.

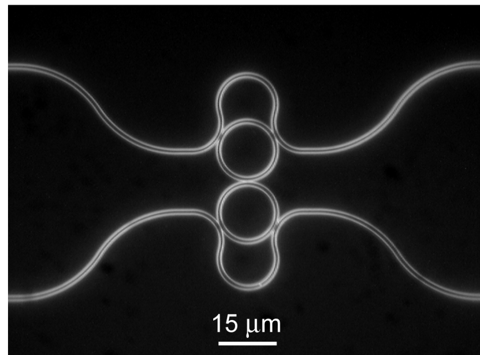

Fig. 3.19 Nomarski optical micrograph of an FSR-doubled filter. Each bright line represents an edge of a waveguide.

of the microrings. To achieve 30 dB extinction of the unwanted resonances, the path lengths must be matched to better than $\lambda/20$. E-beam proximity effects will create a waveguide-width disparity between the outer coupler arms and the outer ring-segments. This disparity will create a propagation-constant mismatch resulting in an optical-path-length mismatch. The path lengths can be corrected by increasing the SEBL dose on the outer arms and reduce the waveguide-width disparity. Alternatively, the outer coupler arms can be made longer to compensate for the path length mismatch. In fact, a path length change of $\lambda/20$ represents a dimensional change of about 45 nm in a waveguide. This required dimensional precision is easily obtained with the SEBL system. The absolute path length correction introduced this way has the advantage of being easy to predict. Nonetheless, it offers design complications in modifying the geometry of the device. Hence, SEBL dose-compensation was used in the demonstration. Finally, as seen in Fig. 3.18, precise 48-nm-offsets are introduced in the outer coupler-arms to enhance mode-matching at the curvature change and avoid loss.

The FSR doubled filters where fabricated as described in Sec. 3.3. A micrograph of an FSR-doubled filter is presented in Fig. 3.19. Waveguide design parameters are reported in Table 3.5. Fifteen devices were fabricated with various dose-compensations

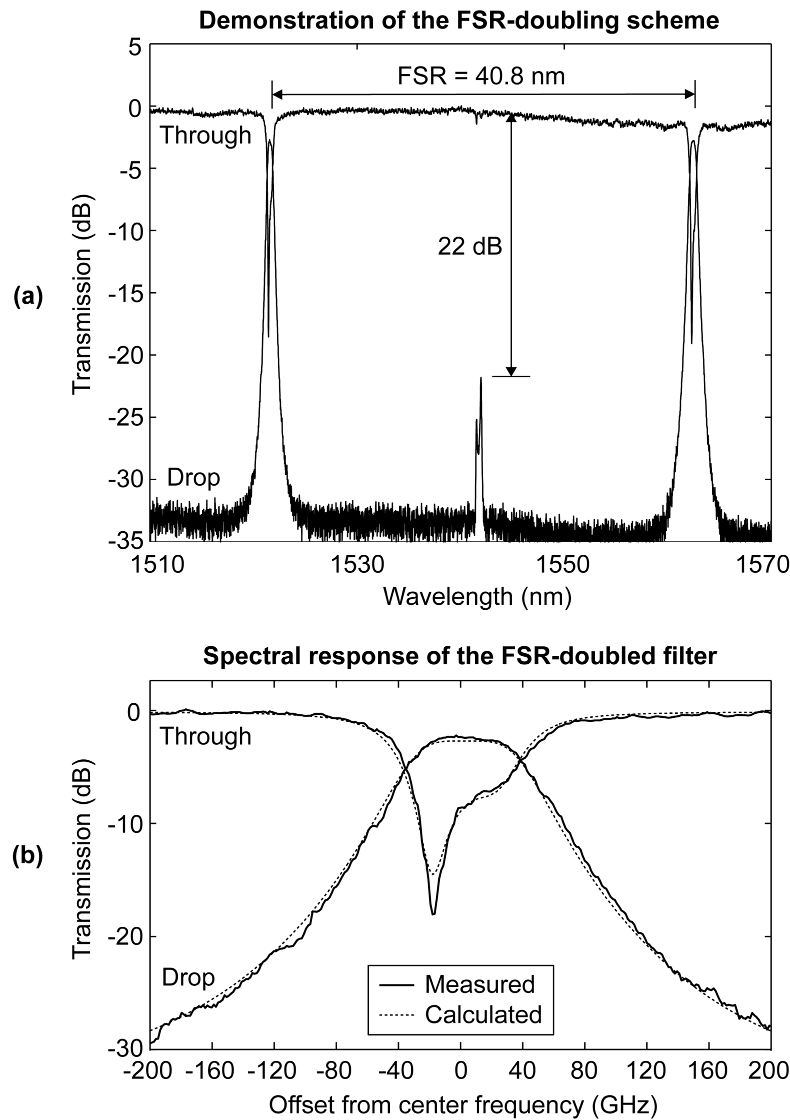

Fig. 3.20 Spectral response of an FSR-doubled filter. (a) Wide spectral scan demonstrating the FSR-doubling scheme. The extinction of the unwanted resonance reached 22 dB instead of the 30 dB desired as dose-compensation of the outer arms was not sufficient to appropriately match the interferometer-arms path lengths. (b) Narrow spectral scan. The two microrings of the filter showed a frequency mismatch of ~20 GHz most probably due to an error in the digital-to-analogue converter of the SEBL.

of the outer coupler-arms. The best spectral response obtained is shown in Fig. 3.20. The dose-compensation range (0 to 14.5% dose increase on the outer arms) was insufficient to offer adequate matching of the path lengths of the interferometer arms. Nonetheless, a

22 dB extinction of the unwanted resonance was achieved demonstrating the FSR-doubling scheme.

Surprisingly, the spectral response of the filters was not symmetric. The asymmetry was indicative of a ~20 GHz resonance-frequency mismatch between the two microring resonators. This mismatch was repeatable and did not appear in the outer rings of the third-order filters. We believe it is due to an error in the digital-to-analogue converter (DAC) of the SEBL near the center of the SEBL field. Again, strict dimensional control is stressed to a level that is not measurable with standard nanofabrication means such as scanning-electron microscopy. The sensitivity of small optical resonators allows identifying lithographic problems not otherwise detectable.

3.6 CONCLUSION

In this Chapter, we presented the fabricated HIC microring add-drop filters. We demonstrated accurate bandwidth (within 5%), small drop loss (2.5 dB), large in-band extinction (>30 dB), large FSR (up to 40.8 nm), and polarization independent operation using an integrated polarization-diversity scheme.

Most of these achievements have never been reported in the literature. For the first time, frequency matching of microring-filters, more than 30 dB in-band extinction, integrated polarization diversity, and FSR doubling of microring filters was demonstrated.

In Parts II and III of the Thesis, we further investigate the two main challenges in fabrication of HIC microphotonic devices: sidewall roughness and dimensional accuracy. The present Chapter allowed us to illustrate the importance of these two themes. Part II and Part III can be applied to fabrication of any HIC microphotonic devices: from photonic-bandgap structures to microring filters.

PART II

Sidewall Roughness

Chapter 4 Roughness Characterization .... p. 71

Chapter 5 Roughness Optimization .... p. 85

Chapter 6 Roughness-Induced Optical Loss .... p. 97

In Part II, sidewall roughness, one of the two main challenges in fabrication of high-index-contrast microphotonic devices, is addressed. Roughness is characterized and optimized, and the roughness-induced optical loss is calculated. The spectral density of sidewall roughness is measured at various stages of fabrication. The roughness-generating fabrication steps are identified and optimized. The first three-dimensional analysis of scattering losses due to sidewall roughness is derived and used to estimate roughness-induced optical loss from spectral density measurements. The scattering-loss analysis allows us to identify waveguide cross-sections and optical-field polarizations minimizing scattering losses.

Chapter 4

Roughness Characterization

4.1 INTRODUCTION

As mentioned above, high refractive-index-contrast (HIC) material systems allow for small bending radii in microphotonic devices. Consequently, device size shrinks considerably and large-scale optical integrated circuits become possible. On the other hand, scattering losses due to line-edge roughness (LER) become substantial when index contrast increases and may even render devices unusable [20 - 24]. LER depends strongly on the parameters of the fabrication process used; as a result, process optimization can greatly improve device performance.

For process optimization, knowledge of the effects of individual fabrication steps on scattering losses is key. Thus, being able to track the expected scattering losses in a device while it is being fabricated would be extremely helpful. In fact, this can be done by measuring the spectral density of LER at several stages of fabrication. Then, the expected scattering losses can be calculated by employing one of the methods already established [20 - 23] or the improved scattering-loss analysis of Chapter 6. Hence, if one knows how a particular fabrication step affects the spectral density of LER, one knows how that step affects scattering losses in the device being fabricated. Note that very little

data on the spectral density of LER has been published [22, 24]. Moreover, the usual characterization of roughness with a simple standard deviation is not sufficient to obtain an adequate estimate of scattering losses.

In this chapter, we describe the evolution of LER during fabrication of HIC microphotonic devices. First, we present an efficient scheme for measurement of the spectral density of LER. Then, we use this method to estimate the impact on roughness of steps commonly encountered in the fabrication of HIC microphotonic devices.

The spectral density of LER is obtained from high-resolution micrographs acquired with a scanning-electron-microscope (SEM). First, line edges are detected in the micrographs. Then, various statistical methods are used to obtain an estimate of the spectral density. Finally, the measured spectral density is fit to a common roughness model.

The effects on roughness of liftoff, reactive-ion-etching (RIE) parameters and two non-chemically-amplified electron-beam resists are reported. Our fabrication processes were based on direct scanning-electron-beam-lithography (SEBL). In fact, feature size often becomes too small, and dimensional control too tight, in HIC microphotonic devices, for standard photolithography.

We found that resist type, liftoff processing, and RIE parameters can all have dramatic impacts on the spectral density of roughness. Of the two resists investigated, hydrogen silsesquioxane (HSQ) shows rougher edges than poly-methyl-methacrylate (PMMA). To obtain smooth sidewalls, an adequate sidewall polymerization is required during RIE. Moreover, a sharp resist profile is needed when liftoff is used. We show that the methods described in this paper can be used as an efficient process optimization tool for fabrication of HIC microphotonic devices.

4.2 ROUGHNESS MODEL

LER is frequently represented by a one-dimensional (1D) distribution with zero-mean called $f(z)$. As illustrated in Fig. 4.1, $f(z)$ represents the excursions of the real edge from an idealized straight edge. The nature of the roughness is described by the autocorrelation function of $f(z)$ defined by

$$R(u) = \langle f(z) f(z+u) \rangle \tag{4.1}$$

The spectral density of roughness is the Fourier transform of the autocorrelation function over 2π. In most cases, the autocorrelation function follows an exponential model

$$R(u) \approx \sigma^2 \, exp\left(-|u|/L_c\right) \tag{4.2}$$

where σ^2 is the variance, and L_c is the correlation length. Then, the spectral density becomes

$$S(\Lambda) \approx \frac{\sigma^2 L_c}{\pi\left(1 + L_c^2 \Lambda^2\right)} \tag{4.3}$$

where Λ is the spatial radial frequency.

In integrated-optical waveguides, top and bottom walls can be polished and are

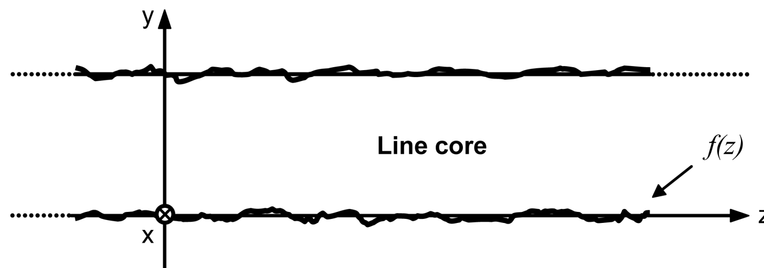

Fig. 4.1 Top view of a line with rough edges. Roughness is described by a 1D distribution with zero mean called $f(z)$.

considered smooth. Only sidewalls are considered rough. In most cases, sidewall roughness appears as vertical stripes. Then, it can be approximated by a 1D distribution and represented by the same roughness distribution $f(z)$. With microphotonic devices, only a restricted band of spatial frequencies contributes to scattering losses. This band is given by

$$\beta - \frac{2\pi}{\lambda_{clad}} < \Lambda < \beta + \frac{2\pi}{\lambda_{clad}} \tag{4.4}$$

where β is the propagation constant in the waveguide, and λ_{clad} is the wavelength in the cladding [20]. For high-index-contrast waveguides, this represents spatial periods between 0.5 and 6 μm. Scattering losses are proportional to σ^2 and follow a complex function of L_c. For the range of L_c usually observed, scattering losses increase when L_c increases.

4.3 MEASURING ROUGHNESS: METHODOLOGY

To estimate the spectral density of roughness, we first acquire micrographs with an SEM, viewing the structures from the top. Then, we obtain $f(z)$ from the micrographs and use various statistical methods to estimate the spectral density. Finally, we fit the spectral-density estimates to the exponential model of Sec. 4.2.

4.3.1 Acquiring Micrographs

To adequately determine roughness statistics, the size of the micrographs must meet two criteria. First, the pixel size of the micrograph, the sampling interval of our data, must be less than one-tenth of the expected correlation length, L_c [25]. Second, the micrographs must be large enough for the sampling to span at least $60\,L_c$. As L_c is usually between

20-80 nm, we used a pixel size of 1.3 nm and micrographs containing 3072 by 2304 pixels. A pixel size of 1.3 nm is below the spatial resolution of an SEM. Therefore, spatial frequencies on the order of a pixel size will not be detected. However, the position of an edge can be detected with better precision than the resolution of the system. Since the roughness statistics often vary along a line edge, one usually needs to take about ten micrographs at different locations to get a good spectral-density estimate.

Noise in micrographs can bias the measurements, so extensive averaging is needed. Moreover, an integration algorithm is favored over a slow scan, since the latter converts mechanical noise into artificial LER. Special care must be taken when analyzing the LER of materials such as PMMA, which can be affected by the electron beam, i.e., a compromise must be found between averaging the signal and damaging the material.

4.3.2 Obtaining $f(z)$ from the micrographs

To obtain the roughness distribution, $f(z)$, noise in the micrographs is first further reduced using an adaptive two-dimensional Wiener filter [26]. Then, edges are detected using the Canny method [27]. Finally, an edge is selected, rotated and scaled to obtain $f(z)$.

4.3.3 Obtaining a spectral density estimate from $f(z)$

We have used three different statistical methods to obtain a spectral-density estimate from $f(z)$:

1. direct autocorrelation function fitting,
2. Blackman-Tukey procedure [28, 29],
3. autoregressive model fitting [29, 30].

The autoregressive model fitting is the most refined procedure and is described in detail

below. It provides smoother spectra with better resolution than traditional fast Fourier transforms. However, it can be unstable and may provide erroneous results. Hence, the first and the second method are also used to increase our confidence in the spectral estimates. In general, the three techniques should provide similar results.

The first step in any of these methods is to calculate $R(u)$, the autocorrelation function defined in (4.1). Note that micrographs provide data in the form of equally spaced records. Hence, only discreet values of z and u are allowed. We refer to these as z_s and u_t, where *s* and *t* are integers. As LER may vary with position, $R(u_t)$ is calculated on several micrographs, taken at various locations, and then averaged. At this point, one can fit $R(u_t)$ to the exponential model defined in (4.2). Then, the spectral density estimate is given by (4.3). This approach corresponds to the direct autocorrelation function fitting. It provides a rough estimate, but its outcome is easy to interpret. The Blackman-Tukey procedure is described in [28] and [29].

In an autoregressive model, $f(z_s)$ is assumed to follow

$$f(z_s) = I(s) + \sum_{m=1}^{M} a_M(m) f(z_{s-m})$$

where M is the autoregressive order, $a_M(m)$ are the autoregressive coefficients and $I(s)$ is a white noise sequence called innovation. In essence, a point on a line edge is given by a linear combination of previously measured points plus an innovation. The autoregressive coefficients can be found from $R(u_t)$. Once the coefficients are known, the spectral density estimate is given by

$$S_e(\Lambda) = \frac{\varepsilon^2(M)\Delta z}{2\pi \left| 1 - \sum_{m=1}^{M} a_M(m) exp(-i\Delta z\Lambda) \right|^2} \tag{4.5}$$

where $\varepsilon^2(M)$ is the variance of the innovation, and Δz is the pixel size.

The main difficulty in autoregressive model fitting is finding the autoregressive order, M, that fits the data the most accurately. We found the scheme proposed by Akaike [29, 30] to be the most efficient for this purpose. There, the best M is the one providing the minimum final-prediction-error (ξ_{FPE}). The ξ_{FPE} is defined as the expected mean-squared-prediction-error of the autoregressive model when it is used to predict $f(z_s)$.

A detailed recursive method [29] for determining M, $\varepsilon^2(M)$ and $a_M(m)$ is now presented. Assume that $\varepsilon^2(0) = R(0)$ and $a_0(0) = 0$. Then, compute $\varepsilon^2(M), a_M(m)$, and $\xi_{FPE}(M)$ for $M = 0,1,\ldots,L$ using recursively

$$a_{M+1}(M+1) = \left(R(u_{M+1}) - \sum_{m=1}^{M} a_M(m) R(u_{M+1-m}) \right) \Big/ \varepsilon^2(M)$$

$$a_{M+1}(m) = a_M(m) - a_{M+1}(M+1) a_M(M+1-m) \qquad (m = 1,2,\ldots,M)$$

$$\varepsilon^2(M+1) = \varepsilon^2(M)\left[1 - \left(a_{M+1}(M+1)\right)^2\right]$$

$$\xi_{FPE}(M) = \left[(N+M+1)/(N-M-1)\right]\varepsilon^2(M)$$

where N is the number of points in $f(z_s)$. Adopt M that minimizes $\xi_{FPE}(M)$. Then, use the corresponding $\varepsilon^2(M)$ and $a_M(m)$ to calculate the spectral density using (4.5). In these calculations, L should be large enough so that a steady increase of $\xi_{FPE}(M)$ is observed for high M values. However, it must not exceed $0.5N$. Usually, L on the order of $2N^{1/2}$ is appropriate.

4.3.4 Fitting the spectral density estimate to the roughness model

Once a spectral-density estimate is available, it is fit to the exponential model, defined in (4.3), using the Gauss-Newton method [31]. Fitting the spectral density to a model makes comparison between experiments easier and simplifies the scattering losses calculations. When the spectral density does not follow the exponential model accurately,

the fit must be made around the narrow radiating spectrum defined in (4.4). Then, the exponential model can be used as a good approximation of the spectral density for calculating scattering losses.

4.4 EXPERIMENT

We have performed a set of experiments to study the evolution of LER during fabrication and to evaluate the measurement methodology described in Sec. 4.3. All SEM micrographs were acquired with a Raith 150 SEBL system. High dimensional accuracy was obtained by calibrating the deflection of the e-beam to the movement of the interferometric stage. To prevent charging, all the samples were covered with a thin layer of Au-Pd (2-3 nm) sputtered from the top. The coverage of the vertical sidewalls is negligible and we did not observe variations in LER measurements due to the Au-Pd layer such as reported in [32]. All LER measurements were taken on one-micron-wide lines.

4.4.1 Evolution of LER during fabrication of HIC microphotonic devices

We have taken several LER measurements at various stages of fabrication for the process described in Sec. 3.3 and for possible alternatives. The fabrication process was first qualitatively optimized to provide vertical and smooth sidewalls.

First, Si wafers were oxidized to form a 2.5-um-thick layer of thermal oxide. Then, a 330-nm-layer of silicon-rich silicon nitride (SiN) was deposited using low-pressure-chemical-vapor-deposition (LPCVD). Next, a 200-nm-layer of PMMA was spun on the double layer. In addition, a 60-nm-layer of Aquasave, a water-soluble conductive polymer from Mitsubishi Rayon, was spun on the PMMA to prevent charging. The PMMA was then exposed at 30 KeV using the Raith 150 SEBL system. The Aquasave

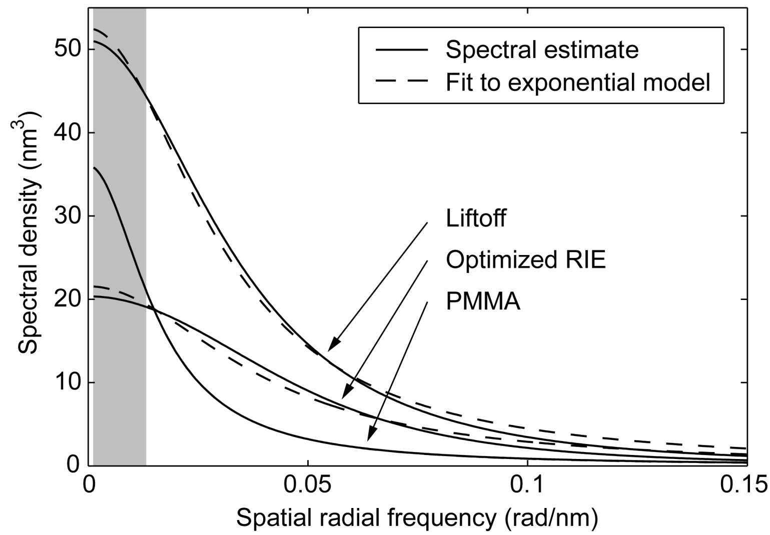

Fig. 4.2 Evolution of LER during fabrication of HIC microphotonic devices. Spectral density estimates were obtained using autoregressive model fitting. Then, the estimates were fit to an exponential model of roughness. The shaded area highlights spatial frequencies responsible for scattering losses. For PMMA, the fit to the exponential model overlaps the spectral estimate

was removed, and the PMMA was developed for 60 sec at 21°C using a solution of isopropanol (IPA) and methyl iso-butyl ketone (MIBK) in a 2:1 ratio. Next, 50 nm of Ni was evaporated on the structure, and a liftoff was performed by removing the non-exposed PMMA in hot 1-methyl-2-pyrrolidinone (NMP). Then, a Plasmatherm 790 was used to define the waveguides with a 440-nm-deep RIE. A pressure of 10 mT, a bias of 250 V, and a gas mixture of CHF_3-O_2 in a 16:3 ratio were used. Finally, the Ni hardmask was removed using a commercial wet Ni etchant of type TFB.

LER measurements were taken on PMMA lines, Ni lines after liftoff and etched waveguides. Results are presented in Table 4.1, and plots of spectral density estimates are shown in Fig. 4.2.

4.4.2 Study of resist

We have compared the LER of two non-chemically-amplified e-beam resists: HSQ and PMMA. HSQ is a negative e-beam resist, while PMMA is a positive one. The two resists were exposed at 50 KeV using an IBM VS2A SEBL system with a VS6 column. Generally, wafers were prepared as described in Sec. 4.4.1. Once again, Aquasave was used to prevent charging and removed just before resist development.

To measure the LER of HSQ, we used Si wafers with 2.5 um of SiO_2, 330 nm of SiN, 130nm of HSQ, and 60 nm of Aquasave. The 130-nm-layer of HSQ was spun on. After exposure by the e-beam, the HSQ was developed in Shipley MF-CD-26 for 25 min at 21°C. For high contrast in HSQ, high e-beam dose and long development time were used. The LER of HSQ is sensitive to under-development. We cut the development time by three on some samples, and measured the LER of under-developed HSQ.

TABLE 4.1
SPECTRAL DENSITY OF LER AT VARIOUS STAGES OF FABRICATION

Stage of fabrication	σ^2 (nm^2)	L_c (nm)
PMMA	1.8	64
Liftoff	5.2	35
Optimized RIE	2.6	26
HSQ	4.7	20
Under-developed HSQ	9	21
Liftoff on rounded resist profile	12	33
High sputtering	5.0	30
Medium sputtering	4.2	35
Low sputtering	3.7	40
High polymerization	7.1	34
Low polymerization	4.9*	33*

The spectral estimates were fit to an exponential model of roughness, whose parameters are reported. Values with an asterix are not considered accurate. Optical scattering losses are proportional to σ^2 and follow a complex function of L_c. For the reported range of L_c, a smaller L_c represents smaller scattering losses.

Measurement results are shown in Table 4.1.

To measure the LER of PMMA, we used Si wafers with 2.5 um of SiO_2, 330 nm of SiN, 200 nm of PMMA, and 60 nm of Aquasave. The PMMA was exposed and later developed in the IPA-MIBK solution described above. LER measurement results were the same as those obtained in Sec. 4.4.1 by exposing PMMA at 30 KeV.

4.4.3 Study of RIE

We have investigated the effect of sputtering and sidewall polymerization on LER. Sputtering was controlled by changing the bias in RIE, while sidewall polymerization was varied by changing the gas ratio.

Si wafers with 330 nm of SiN, 200 nm of PMMA, and 60 nm of Aquasave were used as a starting point for this experiment. The resist was exposed at 30 KeV using the Raith 150 SEBL system. Then, the Aquasave was removed, and the PMMA developed using the IPA-MIBK solution previously described. The PMMA was over-developed to obtain a rounded profile and study its effect on LER. Next, 50 nm of Ni was evaporated, and a liftoff performed. Then, the samples were etched in various ways using the Plasmatherm 790. The pressure was kept at 10 mT. First, samples were etched for a constant depth of about 300 nm with a constant CHF_3-O_2 gas ratio of 16:3 sccm but with different biases of 125 V, 250 V and 375 V. As the bias increases, the sputtering increases, and the etching selectivity decreases. Next, samples were etched for a constant time with a constant bias of 250 V but with different CHF_3-O_2 gas flow ratios of 17:0 and 11:8 sccm. As the O_2 content increases, the sidewall polymerization decreases. In these last samples, a constant etch time was chosen, instead of a constant etch depth, to minimize LER variations due to sputtering. LER measurement results are presented in Table 4.1. The LER of PMMA was equivalent to the one previously obtained.

4.5 DISCUSSION

When presenting the measurement results, we did not indicate an explicit measurement error since it is problematic to evaluate. First, the accuracy of the spectral estimate obtained using the method proposed by Akaike [29, 30] is not yet precisely known. Moreover, $f(z)$ is not strictly a stationary series, as roughness may vary across the sample and from one sample to another. In general, parameters within 10% of one another should probably be considered identical.

In Table 4.1, some of the standard deviations ($\sqrt{\sigma^2}$) obtained are of the order of a pixel size. This is acceptable as long as the number of points used in measurements is high, in which case the edges of the Gaussian describing the transversal distribution of points are well defined and an appropriate estimate is possible.

In the exponential model, L_c gives an indication of the power balance between the low and the high spatial frequencies, while σ^2 is a global scaling factor. As L_c increases, more power goes to low frequencies, and less to high frequencies. Optical scattering losses are triggered by the low frequencies of roughness. In Table I, we see that sputtering increases mainly the high frequencies. Hence, it does not influence scattering losses as much as sidewall polymerization, which has a bigger effect on the spatial frequencies responsible for scattering losses. Therefore, an adequate level of sidewall polymerization appears to be the key RIE parameter for smooth sidewalls.

We observed qualitatively that lack of sidewall polymerization increases sidewall roughness dramatically. However, this is not shown in our LER measurements. In the etched samples with low sidewall polymerization, sidewall roughness was not a 1D distribution but varied along the height of the waveguide. The LER measurements were taken at the top of the waveguides. As a result, the sidewall roughness was underestimated. Excursions from the 1D distribution assumption were not observed on

other etched samples. Hence, special care must be taken when measuring the LER of waveguides defined by isotropic etching.

In contrast to HSQ, the LER of PMMA seemed to be independent of development time. However, LER after liftoff appeared sensitive to the PMMA profile and hence to PMMA development and exposure conditions.

4.6 CONCLUSION

We described a method for measuring the spectral density of LER from high-resolution micrographs. The method was then applied to estimate the influence of common fabrication steps on LER. We observed that PMMA offers a smoother edge than HSQ. Moreover, smooth sidewalls require adequate sidewall polymerization during RIE, and a sharp resist profile when liftoff is used. We confirmed that sidewall roughness could be improved dramatically by adjusting the fabrication parameters. The LER measured on waveguides described in Sec. 4.4.1 is significantly smoother than other data reported in the literature [22, 24]. The LER measuring methodology described in this paper is well suited for process optimization, which is further addressed in Chapter 5.

Chapter 5

Roughness Optimization

5.1 INTRODUCTION

In Chapter 4, we have presented a characterization method used to measure the spectral density of line-edge-roughness (LER). We have identified liftoff and sidewall polymerization at reactive-ion etching (RIE) as the key elements influencing sidewall roughness. In this Chapter, we focus on optimizing these two processes. We report on phenomena not addressed in the literature.

As liftoff is the main source of roughness, modifying the fabrication process to avoid it could improve sidewall smoothness significantly. An alternative is to use a hard negative resist acting as an appropriate etching mask. For this reason, we have investigated above hydrogen silsesquioxane (HSQ), a spin-on dielectric acting as a smooth and high-resolution negative resist. However, its edges were found to be as rough as the lifted off Ni hardmasks (see Table 4.1). In addition HSQ offers a much lower resist-contrast than poly-methyl-methacrylate (PMMA), the positive resist used for liftoff. Therefore, we decided to proceed with liftoff and optimize it even if it is the main source of roughness as it is still the best option we have.

5.2 LIFTOFF OPTIMIZATION

According to Chapter 4, liftoff is the fabrication step generating the most LER. This roughness is then transferred to the core material during RIE to form the biggest component of the sidewall roughness. At best, the LER of a lifted off hardmask line will conform to the resist. However, coarse material microstructure and coverage of the resist-sidewall with the evaporated material worsen the LER of the hardmask. The material microstructure can be managed with appropriate e-beam evaporation parameters and surface cleanliness. The resist-sidewall coverage depends on the geometry of the e-beam evaporator and the angle of the resist-sidewall. In most cases, the geometry of the evaporator cannot be altered and the resist-sidewall angle is the main liftoff optimization parameter.

With sufficiently high e-beam dose, an undercut can be created in the resist. Electrons backscattered by the core-material increase the dose delivered near the resist-dielectric inteface. This undercut is helpful in reducing sidewall coverage and, thus, LER. A sharper undercut can be obtained by using a double-layer resist with the most sensitive resist on the bottom of the double-layer. In our case, a double-layer was investigated with two PMMA resists of different molecular weights: 950 kg on top and 495 kg on the bottom. The lower the molecular weight is, the more sensitive the PMMA.

Ni, Cr and Al were investigated as hardmask materials. Of the three, Ni was found to provide the best liftoff results. Cr showed high enough stress to pull on the PMMA and alter the sidewall angle while Al was too soft to be used as a hardmask for our applications. The problem with liftoff of Cr is illustrated in Fig. 5.1. The thin Cr film resulting from sidewall coverage is partially sputtered during RIE and results in a significant roughening of the waveguide edge. As discussed in Chapter 3, Cr hardmasks need to be used in the two-layer fabrication process employed for the polarization

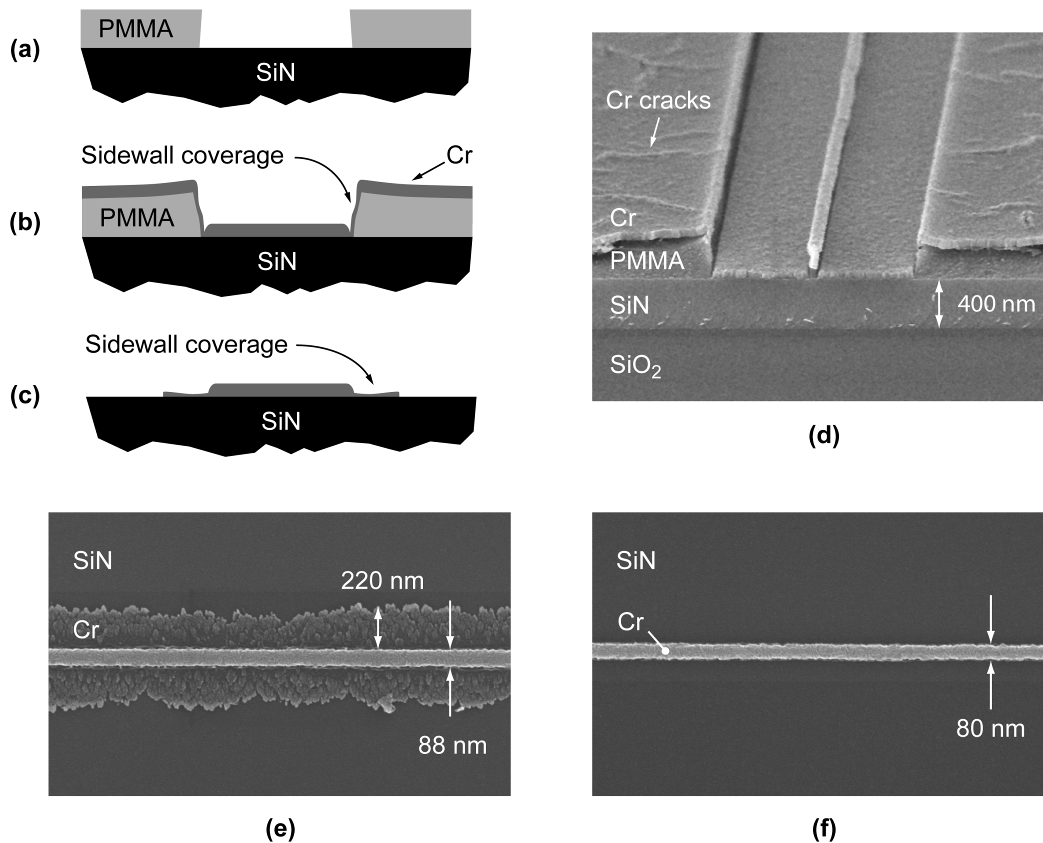

Fig. 5.1 Problems with liftoff of Cr. Starting from a sharp resist profile (a), the Cr is e-beam evaporated (b). The Cr film is under high tensile stress. It progressively deforms the resist profile allowing significant resist-sidewall coverage. (c) The resist is removed and the Cr film covering the sidewalls falls on the sides. The Cr film from the sidewalls is partially sputtered during RIE and generates significant roughness. (d) Cross-sectional electron micrograph of evaporated Cr on two 800-nm-wide PMMA lines. The Cr film on top of the resist shows severe cracking attributed to its high tensile stress. (e) Top-view electron-micrograph of a narrow Cr line after liftoff. The core of the line is about 55-nm-thick. The thin film on the sides must be 5- to 10-nm-thick to be clearly visible in the micrograph and its width corresponds to the height of the resist used. (f) Ultrasonic agitation during liftoff is usually not recommended as it roughens line-edges. In this case, however, it provides clean Cr lines by ripping the sidewall coverage.

independent filters so this problem had to be addressed. To obtain clean and fine Cr features, ultrasonic agitation had to be used at liftoff to rip the Cr film resulting from

sidewall coverage. Unfortunately, ultrasonic agitation also roughens the hardmask and provides for rougher sidewalls. This was illustrated in Fig. 3.15. As an alternative, a strong resist undercut could counter-act the effect of the Cr pulling on the resist and reduce sidewall coverage. However, to obtain acceptable Cr lines, the SEBL dose has to be increased to prohibitive levels resulting in a significant increase of the minimum feature size.

Surprisingly, the double-layer resist was found not to be useful for Ni liftoff. A sharp resist profile is desired but the undercut needs to be small. As shown on Fig. 5.2, for strong undercuts, a thin Ni layer is formed on the edge of the hardmask. This layer gets partially sputtered during RIE and worsens the sidewall roughness. The formation of the thin layer might be explained by the sizeable energy of the e-beam evaporated Ni atoms providing them with the needed surface mobility to diffuse into the region shadowed by the upper part of the resist. This secondary Ni line is also formed when exposing a single resist layer with high electron doses.

The impact on roughness of the evaporated Ni thickness and the evaporation rate was studied. The thickness was varied form 30 to 50 nm and the evaporation rate from 0.1 to 1 nm/s. No significant impact on the roughness of the hardmask was observed. On the other hand, the e-beam evaporator pump down time has shown to have a significant impact on the Ni microstructure. A finer microstructure was observed when the sample was pumped down for a longer time (two hours or more) but the microstructure seemed independent of the final vacuum pressure attained. The improvement of the microstructure was associated with a stronger resistance of the PMMA to 1-methyl-2-pyrrolidinone (NMP) at liftoff. At long pump downs, the PMMA dissolution rate in NMP was half that at short pump down. This suggests a densification of PMMA. At development, a notable amount of developer penetrates in the PMMA and softens the

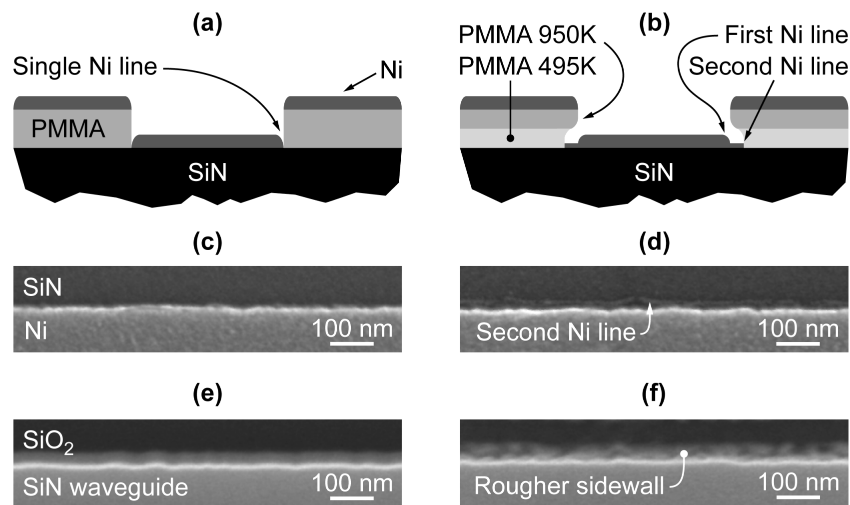

Fig. 5.2 Impact of resist profile on sidewall roughness. An undercut in the resist profile is desired but must be kept small. Schematic cross-section of evaporated Ni on (a) a single PMMA layer and (b) a double PMMA layer. Top-view electron micrograph of resulting Ni liftoff for (c) a single PMMA layer and (d) a double PMMA layer. A second Ni line appears if the resist undercut is too large. This second Ni line is partially sputtered during etching and contributes to increased sidewall roughness. Resulting waveguide sidewalls from a Ni hardmask (e) whitout and (f) with a secondary Ni line.

resist. This residual developer is one of the many possible molecules that may hinder the Ni microstructure as it evaporates from the PMMA in vacuum.

In the present work, a single layer of 950 kg PMMA was used. The e-beam dose was selected to be the highest one not triggering the formation of the thin secondary Ni layer (mostly between 240 and 310 μC/cm^2). The PMMA was developed in a 2 to 1 mixture of IPA to MIBK for 60 s at 21°C. A lower fraction of MIBK provides a higher-contrast developer but increases the LER of the PMMA and should be avoided [33]. Several other combinations of exposure dose, development time, and development strength were tried but were not found to improve the resist profile.

5.3 REACTIVE-ION ETCHING OPTIMIZATION

To obtain smooth and vertical sidewalls, adequate sidewall polymerization (passivation) and hardmask erosion are required. The sidewall polymerization is controlled through the amount of O_2 in the CHF_3-O_2 gas mixture. The more O_2 is used, the weaker is the polymerization. When the polymerization is too low, the sidewalls will be curved inwards and the hardmask undercut, which fosters mask erosion and roughness. When the polymerization is too high, the sidewalls will be straight but slanted with a wider base than top. A 16-to-3 sccm ratio of CHF_3 to O_2 was found optimal for SiN etching.

Mask erosion is know to be an important source of sidewall roughness. Surprisingly, it should not be strictly minimized. When using a Ni hardmask, the hardmask-to-SiN etching selectivity can be very high. We found that a controlled sputtering of the Ni hardmask can reduce sidewall roughness presumably by polishing the hardmask during the RIE. Using a Plasmatherm 790, a 500 V bias resulting in a power of about 300 W was found optimal. It reduced the SiN-to-Ni etching ratio to about 50-to-1.

The above etching parameters were used for fabrication of the multistage filters. For the polarization-independent filters, the gas mixture was modified to a 16-to-4 sccm ratio of CHF_3 to O_2 in order to provide more vertical sidewalls. Prior to the multistage filters, a bias of 250 V and a power of 400 W were used. It offered a small etching selectivity between SiN and SiO_2 enabling the use of a single gas ratio during RIE, but resulted in problematic sample heating and roughness repeatability. For the multistage filters, pure CHF_3 was used once the SiN-SiO_2 boundary was reached to achieve the required over-etch of 200 nm into SiO_2.

5.4 RESULTING SIDEWALL ROUGHNESS

The spectral density of sidewall roughness was measured using the technique described in Chapter 4. The measured data was fitted to an exponential model of the autocorrelation function of roughness. This model has already been presented in Sec. 4.2 and is repeated here for the reader's convenience. It is given by

$$R(u) \approx \sigma^2 \exp\left(-|u|/L_c\right),$$

where σ^2 is the roughness variance and L_c is the correlation length. A large L_c is indicative of strong representation of low spatial-frequencies in the spectral density of roughness. As scattering losses due to sidewall roughness are triggered by these low spatial frequencies of roughness, a small L_c is considered better (see Chapter 6).

Measured values of σ^2 and L_c are presented in Table 5.1. The roughness measurements were performed on bus-waveguides of actual filters. Fabrication of the three filter structures was separated by several months. The process was re-optimized to achieve smoother sidewalls on the later fabricated multistage filters. Electron micrographs illustrating the roughness obtained are presented in Figs. 5.3 and 5.4. The sidewall smoothness achieved is within the best reported [24, 34].

An increase in sidewall roughness was observed between the first third-order filters and the first frequency-compensated filters. Despite thorough re-optimization, the smoothness obtained on the first third-order filters was never later reproduced. This is

TABLE 5.1
MEASURED SIDEWALL ROUGHNESS ON FABRICATED FILTERS

Parameter	First Third-Order Filters	First Frequency-Matched Filters	Multistage Filters
σ^2	2.4 nm^2	3.5 nm^2	2.4 nm^2
L_c	25 nm	30 nm	35 nm

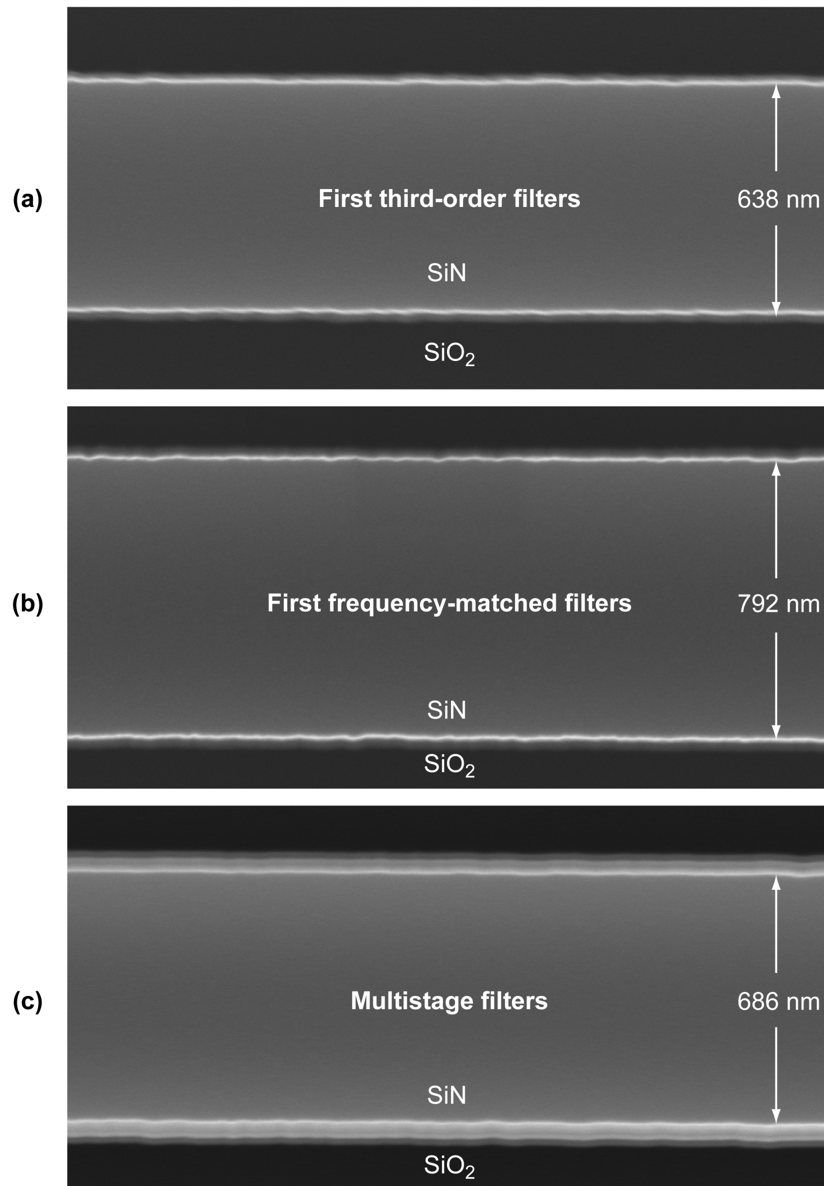

Fig. 5.3 Top-view electron-micrographs of various bus-waveguides showing the waveguide sidewalls corresponding to the measured spectral densities of sidewall roughness reported in Table 5.1. (a) Bus waveguide of first third order filters. (b) Bus waveguide of first frequency-matched filters. (c) Bus waveguide of multistage filters. A more slanted sidewall is observed in (c) resulting from the re-optimized RIE process.

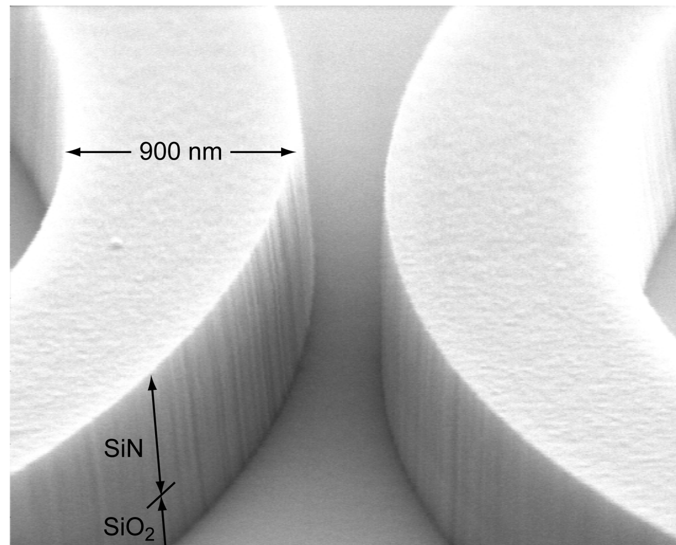

Fig. 5.4 Electron-micrograph of a ring-to-ring coupling gap showing sidewall roughness. The ring-waveguides are about 900-nm-wide and 600-nm-high. Sidewall roughness is formed of long striations and can be well approximated by a one-dimensional distribution. Special attention to the scanning-electron-microscope parameters is needed to see the roughness (without fine tuning of the parameters, the waveguide will appear perfectly smooth). The RIE parameters used were the ones of the re-optimized RIE process employed for etching of the multistage filters so the roughness statistics are similar to the roughness shown in top-view of Fig 5.3c.

believed to be associated to a change of the Ni target used at evaporation. The Ni target used first was not pure Ni as it was contaminated with time. This might have allowed for a smoother microstructure by reducing the magnetic component of the free energy of Ni that forces the material towards bigger grains. Note that there is no satisfactory proof for this hypothesis as the old Ni target is no longer available. Nonetheless, it illustrates the main problem with liftoff: its sensitivity to fabrication parameters.

5.5 CHEMICAL POLISHING

Chemical polishing may allow smoothing of fabricated waveguides. During chemical etching of a material, a boundary layer with a significant gradient of reactant-

concentration develops near the etched surface. If the thickness of the boundary layer is on the order of the roughness, the etching rate of peaks in the roughness will be faster than the etching rate of valleys and smoothing will occur [35]. The polishing efficiency is defined as the ratio of the etching rate of peaks to the etching rate of valleys. The polishing efficiency is a function of the etchant strength, viscosity, and agitation.

A polishing experiment was performed by etching one of the optical chips with the first frequency-matched filters in boiling 85% phosphoric acid for 5 min. About 30 nm of material was removed but no significant change was observed in the resulting roughness (except for the highest spectral components being affected) and propagation loss. The polishing efficiency must be very high to affect the long spatial periods of roughness generating radiation (0.5 to 6 μm) without etching a significant amount of material. The effective resolution of a fabrication process employing chemical polishing will be reduced by twice the amount of material etched. This is not a problem for isolated waveguides but it reduces the interest in chemical polishing for microring filters and other microphotonic devices requiring high lithographic resolution.

5.6 CONCLUSION

A sidewall roughness optimization strategy was presented. In Chapter 4, liftoff and RIE were identified as the process steps affecting roughness the most. In this Chapter, these process steps were optimized and phenomena not addressed in the literature described. The optimized sidewall roughness was measured and the smoothness achieved was found to be within the best reported. In Chapter 6, we develop the most accurate analysis of scattering losses due to sidewall roughness in microphotonic waveguides. It will allow us to better understand the scattering mechanism and further optimize the problem of

scattering losses by identifying field polarizations and waveguide cross-sections that are less sensitive to roughness.

Chapter 6

Roughness-Induced Optical Loss

6.1 INTRODUCTION

Scattering losses due to sidewall roughness often limit the performance of high-index-contrast microphotonic devices. Two-dimensional (2D) analyses of scattering losses in planar dielectric waveguides have been reported by several authors [20 - 22, 36 - 39]. It was suggested in [39] that a 2D analysis can be applied to rectangular waveguides by the use of the effective-index method [40]. First, the rectangular waveguides are reduced to effective slabs. Then, the 2D scattering loss analyses are applied. This approach was used in [24]. However, Haus [41] indicated that applying a 2D scattering loss theory to a rectangular waveguide assumes an incorrect radiation profile, as it considers the radiation pattern of a planar waveguide and not of the actual rectangular waveguide, and could result in an incorrect computation of power loss. This was confirmed in [23, 42]. In fact, the 2D analyses cannot predict how the waveguide cross-section affects the radiation efficiency. It is well known that scattering losses are smaller for wide and flat waveguides as the field overlap becomes smaller on the rough sidewalls. However, the

effect of the waveguide cross-section on the radiation pattern and, thus, on the total radiated power is unknown.

We present a leading order three-dimensional (3D) analysis of scattering losses due to sidewall roughness in straight rectangular dielectric waveguides, valid for any refractive-index-contrast and field polarization. An analysis of higher-than-leading order is not preferred as the spectral density of roughness that is required for loss estimates is difficult to measure accurately (see Chapter 4) and even more difficult to predict. Our goal is to improve the power loss estimate and, more importantly, to identify trends allowing design of useful waveguide cross-sections that minimize scattering losses for practical roughness statistics.

First, we present a simplified 3D scattering loss analysis, valid for low refractive index-contrast waveguides only. Sidewall roughness is considered as a volume current source and array factors are used to introduce significant mathematical simplifications. Then, the analysis is extended to all index-contrasts by taking into account the impact of reflections of the radiated field on the waveguide walls. Scattering-loss analyses are concerned with the ensemble average of power loss. That is, by the average loss experienced by a large number of waveguides with the same cross-section and roughness statistics.

We provide scattering loss estimates for a wide variety of waveguides. We show that the 2D analyses can overestimate scattering losses of small waveguides by an order of magnitude. We provide guidelines for design of waveguide cross-sections that are less sensitive to sidewall roughness. To our knowledge, this is the first analysis of scattering losses that explicitly considers how the radiation pattern is affected by the waveguide cross-section.

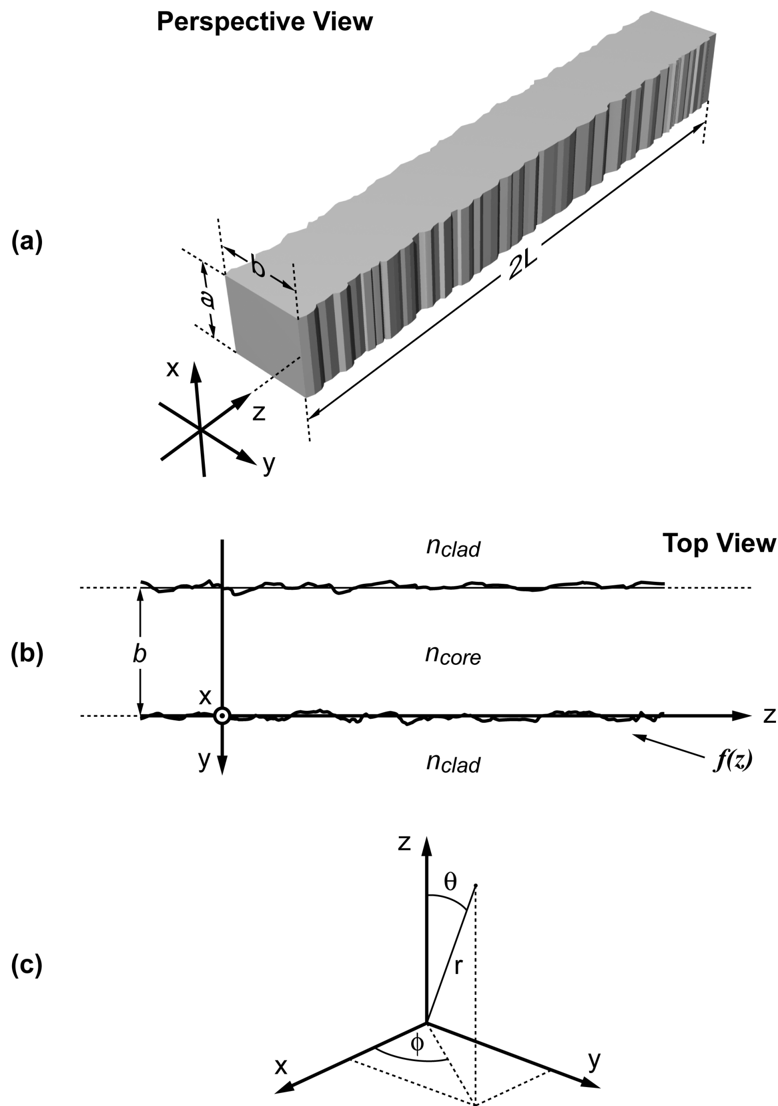

Fig. 6.1 (a) perspective view and (b) top view of a rough rectangular waveguide. The top and bottom walls are considered smooth and only the sidewalls are believed rough. The waveguide-core is surrounded by a uniform cladding of refractive index n_{clad}. (c) Spherical coordinate system used.

6.2 ROUGHNESS MODEL

A roughness model has already been presented in Sec. 4.2. However, to allow consistency with work already published in respective areas, the definition of the spectral

density of roughness is modified here by a factor of 2π and the coordinate system rotated. To eliminate any possible confusion, the modified roughness model is presented here in its entirety.

A rough rectangular waveguide is presented in Fig. 6.1a. The top and bottom walls can be polished and are considered smooth so only the sidewalls are considered rough. Most often, sidewall roughness appears as long vertical stripes. It is frequently represented by a one-dimensional (1D) distribution with zero-mean called $f(z)$. As illustrated in Fig. 6.1b, $f(z)$ represents the excursions of the real edge from an idealized straight edge. The nature of the roughness is described by the autocorrelation function of $f(z)$

$$R(u) = \langle f(z) f(z+u) \rangle ,$$

where the brackets represent the ensemble average. In most cases, the autocorrelation function can be well approximated (see [22] and Chapter 4) by an exponential model

$$\mathrm{R}(u) \approx \sigma^2 \exp\left(-|u|/L_c\right), \tag{6.1}$$

where σ^2 is the roughness variance and L_c is the correlation length. Roughness on both sidewalls is assumed to have the same statistical distribution but to be mutually uncorrelated. For scattering-loss analyses, the power spectral-density of roughness is of particular interest. It is given by the Fourier transform of the autocorrelation function [43]

$$\widetilde{R}(\xi) = \int_{-\infty}^{+\infty} R(u) \exp(i\xi u)\, du. \tag{6.2}$$

If the autocorrelation function is approximated by an exponential model, the spectral density of roughness becomes

$$\widetilde{R}(\xi) \approx \frac{2\sigma^2 L_c}{1 + L_c^2 \xi^2} \,. \tag{6.3}$$

Sec. 6.7.3 extends the present scattering-loss analysis to cases where some of the above assumptions are invalid.

6.3 VOLUME CURRENT METHOD

The present loss-analysis is based on the volume current method (VCM) [44]. The VCM considers variations of the dielectric constant as equivalent polarization current densities. In a source-free region, the wave equation becomes

$$\begin{aligned} &\vec{\nabla} \times \left(\vec{\nabla} \times \vec{E}\right) - \omega^2 \mu \varepsilon(\vec{r}) \vec{E} = 0 \\ &\Downarrow \\ &\vec{\nabla} \times \left(\vec{\nabla} \times \vec{E}\right) - \omega^2 \mu \varepsilon_I(\vec{r}) \vec{E} = \omega^2 \mu \left(\varepsilon(\vec{r}) - \varepsilon_I(\vec{r})\right) \vec{E} \\ &\qquad = i\omega\mu \vec{J}(\vec{r}) \,. \end{aligned}$$

Hence, deviations from an ideal dielectric profile $\varepsilon_I(\vec{r})$ are mathematically equivalent to current sources of the form

$$\vec{J}(\vec{r}) = -i\omega\left(\varepsilon(\vec{r}) - \varepsilon_I(\vec{r})\right)\vec{E} = -i\omega\,\delta\varepsilon(\vec{r})\,\vec{E} \,,$$

where $\vec{E}$ is the incident field on the imperfections. Most often, $\varepsilon_I(\vec{r})$ is chosen to be a uniform dielectric profile ε_1. Then, the radiation can be calculated using free-space dyadic Green's functions or, equivalently, the magnetic vector potential in the Lorenz gauge [45]. In the far field, the magnetic vector potential $\vec{A}$ becomes

$$\vec{A} = \frac{\mu}{4\pi}\left(\frac{e^{in_1 k_0 r}}{r}\right) \iiint \vec{J}(\vec{r}')\, e^{-in_1 k_0 \hat{r}\cdot\vec{r}'} dV' \,, \tag{6.4}$$

where k_0 is the free-space wavenumber, n_1 is the refractive index corresponding to ε_1, and the primes refer to the current-source-distribution position and volume. Then, the far-

field Poynting vector reduces to

$$\vec{S} = \hat{r}\frac{\omega n_1 k_0}{2\mu}\left|\hat{r}\times\vec{A}\right|^2 , \tag{6.5}$$

and the total radiated power is

$$P = \oiint \vec{S}\cdot\hat{r}\, dA .$$

Alternatively, a more involved $\varepsilon_I(\vec{r})$ can be employed as long as the corresponding dyadic Green's functions can be computed.

6.4 THREE-DIMENSIONAL ANALYSIS

6.4.1 Problem Decomposition

The decomposition of the scattering problem is shown in Fig. 6.2. The waveguide core is entirely considered as an equivalent polarization-current-density (Fig. 6.2a). As roughness is considered small compared to the waveguide, the guided mode of a perfectly smooth waveguide can be used as a good approximation of the field profile in the waveguide core [21, 44]. This mode can be expressed as

$$\vec{E}_g(\vec{r}) = \vec{\Phi}(x,y)\, e^{i\beta z},$$

where β is the propagation constant. The waveguide is then replaced by the following equivalent polarization current density

$$\vec{J}_{core}(\vec{r}) = -i\omega\varepsilon_0\left(n^2(\vec{r}) - n_{clad}^2\right)\vec{E}_g(\vec{r}) \ ,$$

where n_{clad} is the cladding refractive index, $n(\vec{r})$ is the refractive-index profile of the rough waveguide, and ε_0 is the free-space permittivity.

The guided mode of a straight and smooth waveguide does not contribute to the far field [21]. Consequently, one could remove the perfect waveguide from the calculation without altering the radiation result. Then, only the roughness remains (Fig. 6.2b), and the current distribution is given by

$$\vec{J}_{rough}(\vec{r}) = -i\omega\varepsilon_0 \left(n^2(\vec{r}) - n_I^2(\vec{r})\right)\vec{E}_g(\vec{r}),$$

where $n_I(\vec{r})$ is the refractive index profile of the perfectly smooth waveguide.

To compute the far field of $\vec{J}_{rough}(\vec{r})$, an important mathematical simplification can be introduced by using the concept of the array factor. An array factor is defined by dividing the far field of an array by the far field of one element of that array. The elements must all have the same radiation pattern but may have different phases and amplitudes. As illustrated in Fig. 6.2c, one could divide the roughness in rods of the height of the waveguide and of infinitesimal cross-section in the y-z plane. Then, the far field of the roughness ($\vec{E}_{rough}$) could be found by multiplying the far field of a single rod ($\vec{E}_{element}$) by the roughness array factor (F_{rough}) associated with the roughness distribution

$$\vec{E}_{rough} = \vec{E}_{element} F_{rough}.$$

The roughness array-factor can be found from existent 2D analyses of scattering losses in planar waveguides. A roughness array-factor of the 2D planar scattering problem $F_{rough,2D}$ can be defined by dividing the far field of a rough planar waveguide by the far field of an infinitely long rod with infinitesimal cross-section. Then, F_{rough} can be obtained from the revolution of $F_{rough,2D}$ around the z-axis. This is better understood when considering the array factor as the far field of an array of isotropic sources (Fig. 6.3). As the roughness of a straight waveguide forms a line array, the 3D roughness-array-factor will exhibit rotational symmetry around the axis defined by that array (z-axis in our case). Then, any section of the 3D line-array-factor intersecting the z-axis will be the 2D line-array-factor.

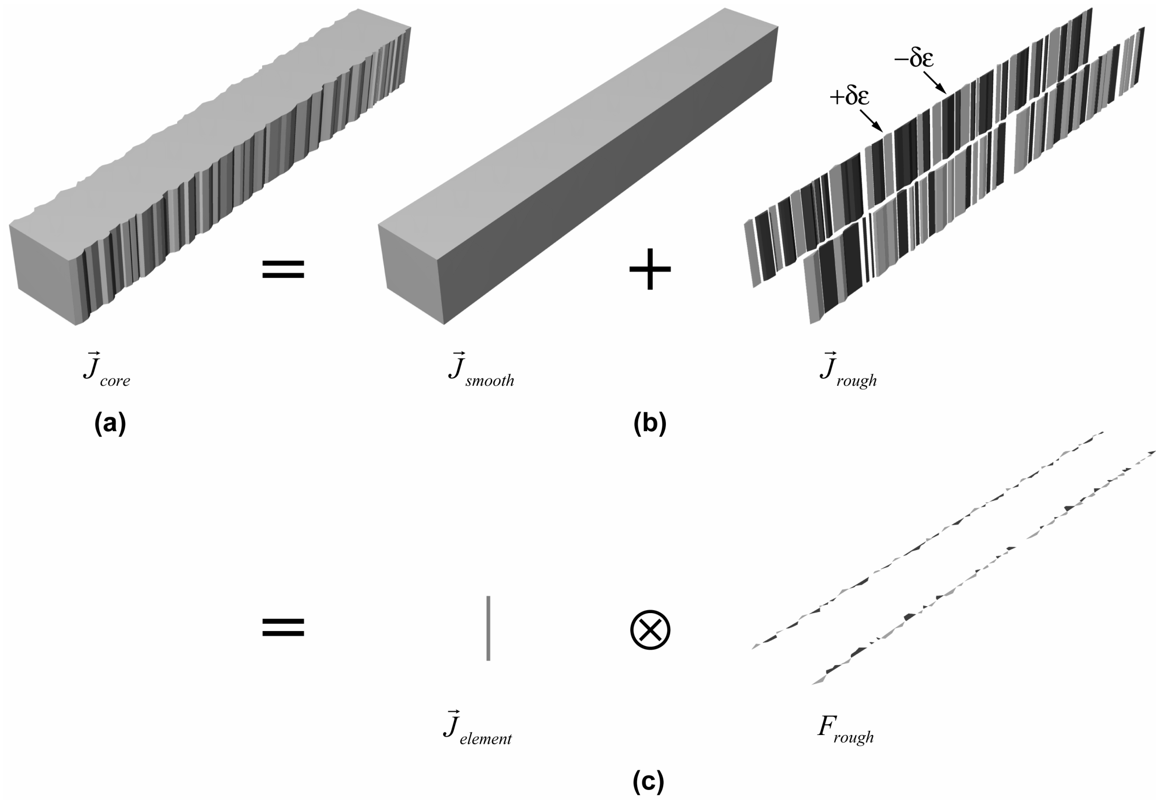

Fig. 6.2. Decomposition of the radiation problem. (a) The rough waveguide-core is replaced by an equivalent polarization current density. (b) A straight and smooth waveguide does not radiate and can be removed from the calculation leaving solely the roughness in the radiation problem. (c) The roughness is divided into rods of the height of the waveguide and of infinitesimal cross-section. A roughness array-factor is defined relating the far field of a single rod to the far field of the roughness.

The actual radiation pattern of the roughness will not show the rotational symmetry of the array as the field of an array element is not symmetric around the z-axis.

When starting from the far field of a rough planar waveguide given by Eq. 14 of [21], the ensemble average of the roughness power array-factor becomes

$$\left\langle \left|F_{rough}\right|^2 \right\rangle = \left\langle \left|F_{rough,2D}\right|^2 \right\rangle = 2\left(2L\right)\tilde{R}(\beta - n_{clad}k_0\cos\theta), \tag{6.6}$$

where $\tilde{R}$ is defined in (6.3), θ is defined in Fig. 6.1c, and $2L$ is the length of the rough waveguide. The factor of 2 in the front of (6.6) comes from the two radiating sidewalls.

As they are mutually uncorrelated, the powers are simply added when the ensemble average is taken. For straight rough waveguides, the phase matching condition between the guided and the radiated modes allows only a narrow range of spectral frequencies of roughness

$$\beta - n_{clad}k_0 < \xi < \beta + n_{clad}k_0 \tag{6.7}$$

to produce radiation losses [20].

The ensemble average of the far-field Poynting vector of the roughness-induced radiation is given by

$$\left\langle \vec{S}_{rough} \right\rangle = \vec{S}_{element} \left\langle \left| F_{rough} \right|^2 \right\rangle ,$$

where $\vec{S}_{element}$ is the far-field Poynting vector of a single rod with the height of the waveguide and an infinitesimal cross-section. The total power radiated per unit length of waveguide becomes

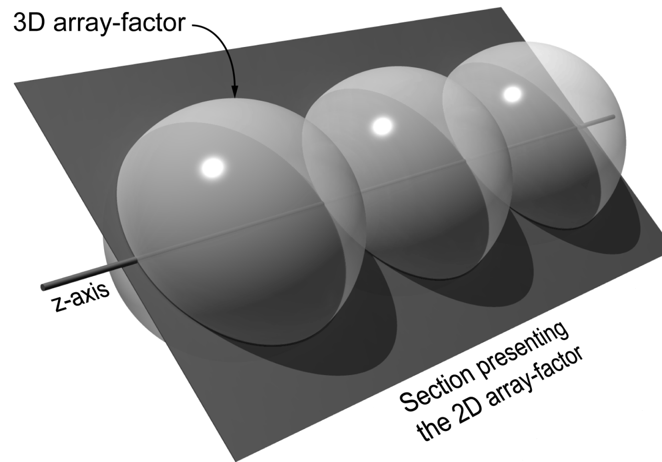

Fig. 6.3. Relation between 2D and 3D array-factors of line arrays. Array factors can be viewed as far fields of arrays of isotropic sources. Any section through the 3D array-factor including the axis of the line array will give the 2D array-factor.

$$\frac{P}{2L} = 2\oiint \left(\vec{S}_{element} \cdot \hat{r} \right) \tilde{R}(\beta - n_{clad} k_0 \cos\theta) \, dA \, .$$

$\vec{S}_{element}$ can be obtained from (6.4) and (8) using

$$\begin{aligned} \vec{J}_{element}(x) &= -i\omega\varepsilon_0 \left(n_{core}^2 - n_{clad}^2 \right) \vec{\Phi}(x,0) \, , \, -a/2 \le x \le a/2 \\ &= 0 \, , \, |x| > a/2 \end{aligned} \tag{6.8}$$

where n_{core} is the waveguide-core refractive-index, a is the waveguide height, and $\vec{\Phi}(x,0)$ is the electric field at the rough boundary on the side of the waveguide core. As one is only interested in the far field, one can use in $\vec{J}_{element}$ an approximate and analytically-convenient vertical-field-distribution

$$\vec{\Phi}(x,0) \approx v \, \vec{\Upsilon}(x) \; , \; -a/2 \le x \le a/2 \, ,$$

where we choose

$$v = \sqrt{\int_{-a/2}^{a/2} \left| \vec{\Phi}(x',0) \right|^2 dx'} \, ,$$

and where $\vec{\Upsilon}(x)$ is normalized to

$$\int_{-a/2}^{a/2} \left| \vec{\Upsilon}(x') \right|^2 dx' = 1 \, .$$

6.4.2 Impact of Waveguide Height, Field Polarization, Vertical Field-Shape, and Roughness Statistics.

Scattering losses for diverse field polarizations, vertical field-shapes, roughness statistics, and waveguide heights are presented in Fig. 6.4 and Fig. 6.5. The radiation loss is normalized to the loss found from the 2D theory of [21] (losses derived only for the x-polarization) to illustrate the effect of the diverse parameters on radiation efficiency. The roughness is assumed to follow the exponential model of (6.1). One can observe that the

2D theory strongly overestimates radiation of waveguides with small normalized heights. In fact, the 2D theory effectively assumes that the sources are of infinite height.

The vertical field-shapes used are shown in Fig. 6.5b. One can observe that the exact

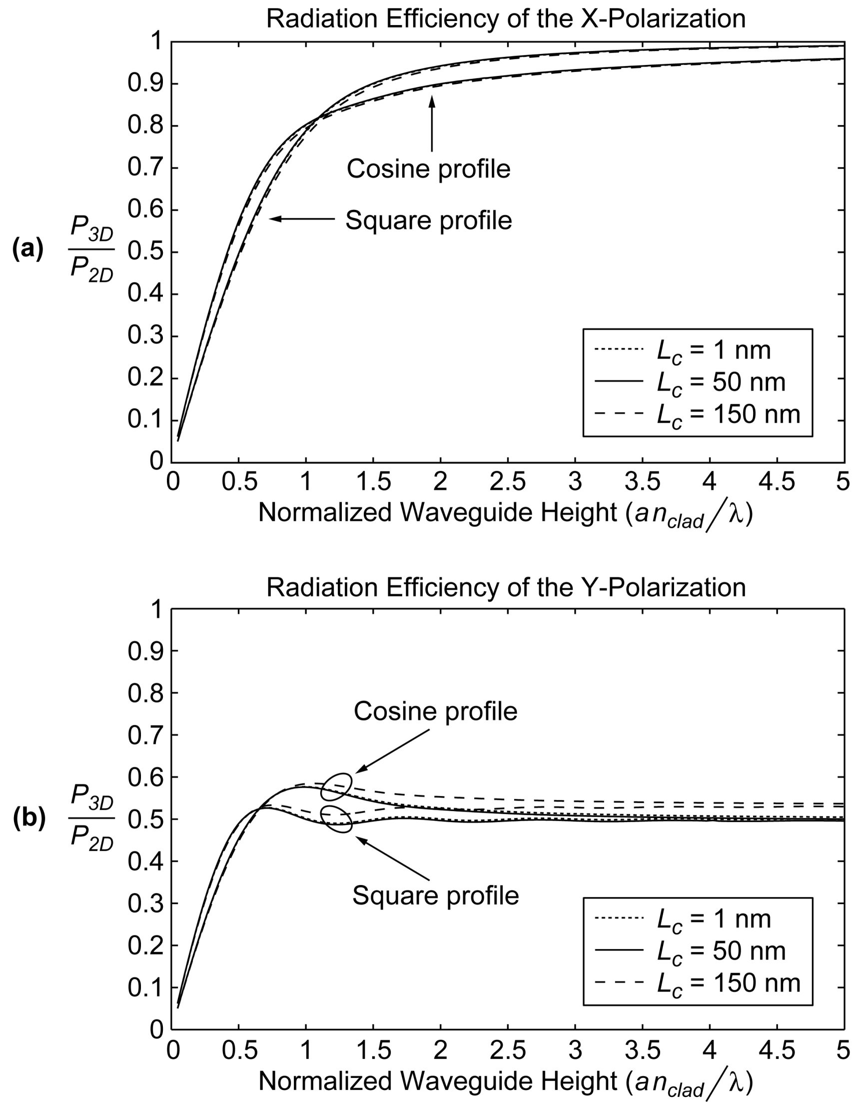

Fig. 6.4. Radiation efficiency of the (a) x-polarization and (b) y-polarization. A schematic of the vertical-field-profiles used is presented in Fig. 6.5b. Scattering losses obtained with the present 3D analysis are normalized to losses found using the 2D theory of [21] (losses only derived for the x-polarization). The plots were computed using n_{clad}=1.45, n_{core}=2.00 and b=800 nm. Nonetheless, these parameters have little influence on radiation efficiency in the present approximation.

field shape is not required for leading-order calculations as the difference between the power radiated by a crude square field-distribution and a realistic cosine field-distribution is relatively small. However, the field distribution cannot be completely neglected as shown by the small radiation efficiency of the sine distribution for small waveguide heights. The radiation efficiency of the sine distribution has only been calculated for the

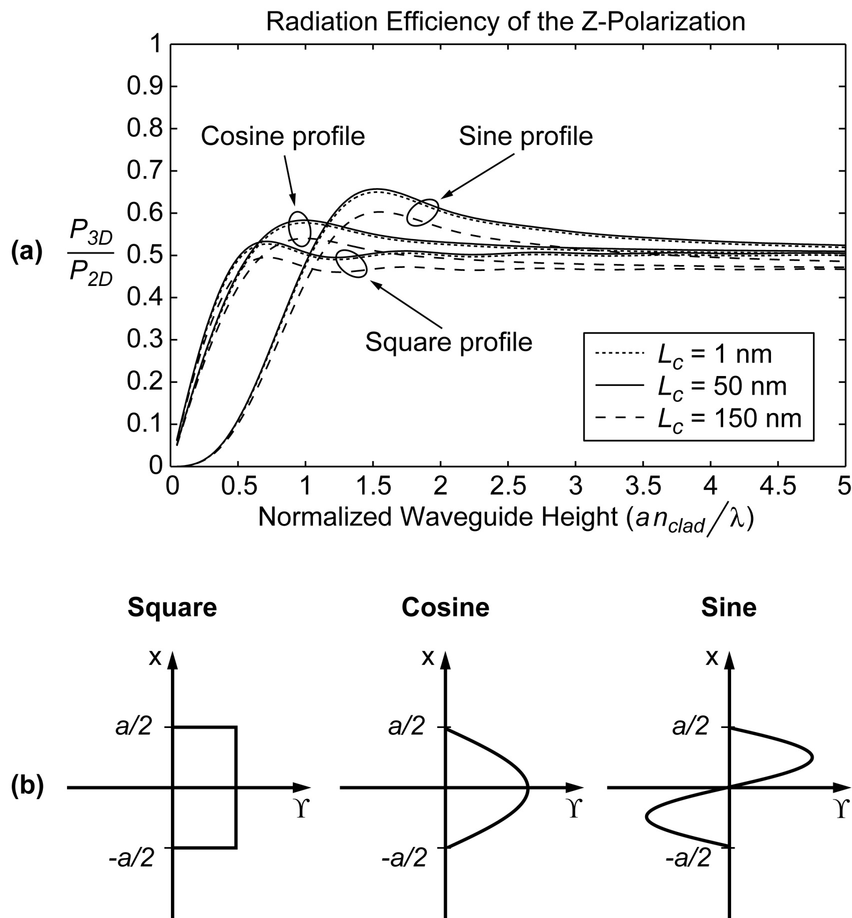

Fig. 6.5. (a) Radiation efficiency of the z-polarization for various vertical-field-shapes and roughness statistics. (b) Schematic of the vertical-field-profiles used. Scattering losses obtained with the present 3D analysis are normalized to losses found using the 2D theory of [21] (losses only derived for the x-polarization). The plots were computed using n_{clad}=1.45, n_{core}=2.00 and b=800 nm. Nonetheless, these parameters have little influence on radiation efficiency in the present approximation.

z-component of the field. When neglecting the third field-component (as further explained in Sec. 6.5), the z-component is the only one showing such distribution in monomode rectangular waveguides (i.e. in the TM-like mode).

Finally, roughness statistics do not show a major impact on radiation efficiency. Within practical values of L_c, the radiation efficiency changes by less than 15%. Moreover, σ^2 acts as a simple scaling factor and has no impact on the radiation profile.

To better understand how the radiation efficiency is affected by the field polarization and the vertical field-shape, one could separate $\vec{S}_{element}$ into

$$\vec{S}_{element} = \vec{S}_{pol} \left|F_{shape}\right|^2 , \tag{6.9}$$

where $\vec{S}_{pol}$ is the far-field Poynting vector of a single point-source and $\left|F_{shape}\right|^2$ is the power array-factor of the vertical field-shape. $\left|F_{shape}\right|^2$ can be defined by dividing the radiation of a single rod with infinitesimal cross-section by the radiation of an identically polarized point source ($\vec{S}_{element} \cdot \hat{r} / \vec{S}_{pol} \cdot \hat{r}$). Then, the power array-factor of the square vertical-field-shape becomes

$$\left|F_{square}\right|^2 = \frac{4\sin^2\left(\frac{1}{2} a \cos(\varphi)\sin(\theta) n_{clad} k_0\right)}{a \cos^2(\varphi)\sin^2(\theta)\, n_{clad}^2 k_0^2} ,$$

the power array-factor of the cosine vertical-field-shape becomes

$$\left|F_{cos}\right|^2 = \frac{8\, a\, \pi^2 \cos^2\left(\frac{1}{2} a \cos(\varphi)\sin(\theta)\, n_{clad} k_0\right)}{\left(\pi^2 - a^2\cos^2(\varphi)\sin^2(\theta)\, n_{clad}^2 k_0^2\right)^2} , \tag{6.10}$$

and the power array-factor of the sine vertical-field-shape becomes

$$\left|F_{sin}\right|^2 = \frac{32\, a\, \pi^2 \sin^2\left(\frac{1}{2} a \cos(\varphi)\sin(\theta)\, n_{clad} k_0\right)}{\left(4\pi^2 - a^2\cos^2(\varphi)\sin^2(\theta)\, n_{clad}^2 k_0^2\right)^2} . \tag{6.11}$$

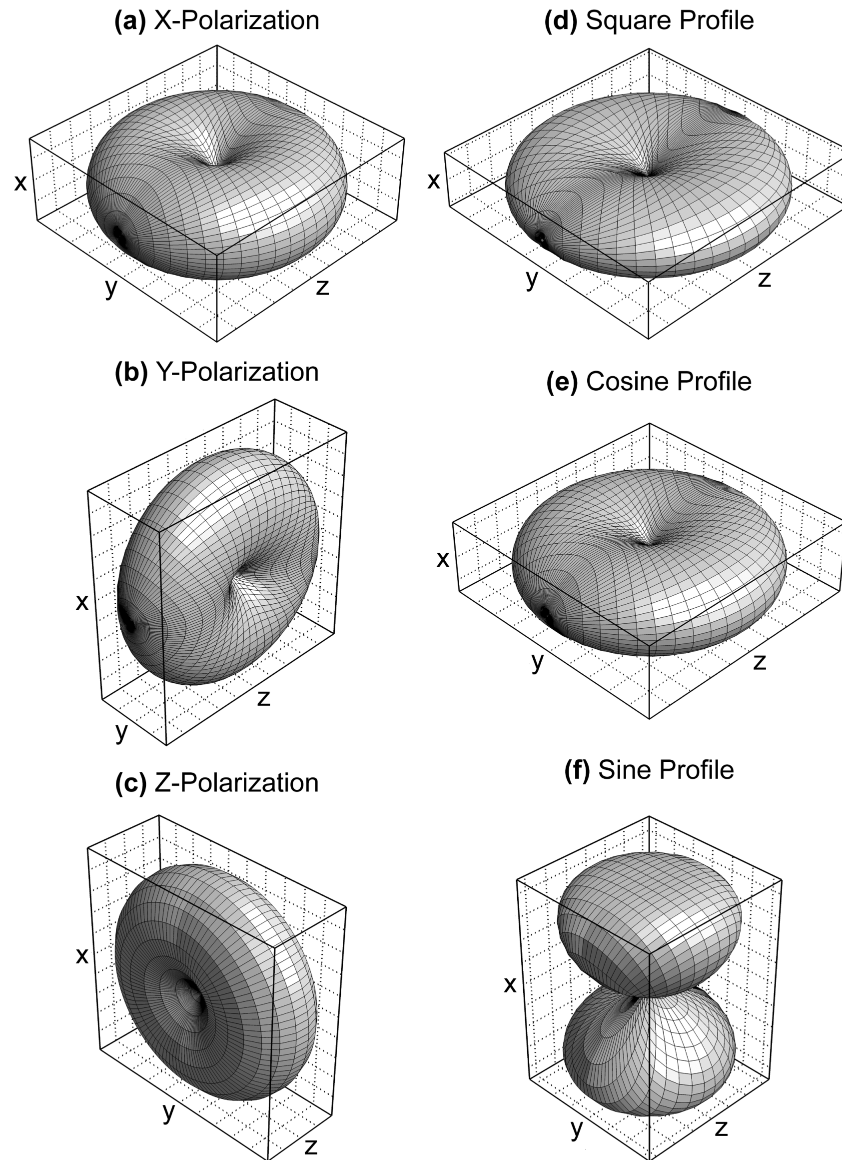

Fig. 6.6. Radiation profile of a point source with (a) x-polarization, (b) y-polarization, and (c) z-polarization. Form of the power array-factor corresponding to a (d) square, (e) cosine, and (f) sine vertical-field-shape. The radiation profile of a source with a given polarization and vertical-field-shape is given by the multiplication of the proper point-source radiation-profile with the proper vertical-field-shape array-factor. For instance, the high radiation efficiency of the x-polarization shown in Fig. 6.4a is consistent with the x-polarized point source having a radiation profile well matched to the array factors of the square and cosine vertical-field-shape.

where ϕ is defined in Fig. 6.1c. The above array factors and the radiation profiles of point sources with diverse polarizations are plotted in Fig. 6.6. The radiation profile of a source element with a given polarization and vertical-field-shape can be found from (6.9). The results are consistent with Figs. 6.4 and 6.5. The radiation profile of the x-polarization is the best matched to the array factors and exhibits the highest radiation efficiency. The radiation profiles of the y- and the z-polarizations are not as well matched to the array factors and show lower radiation efficiencies than the x-polarization. It is not obvious from Fig. 6.6 why the sine vertical-field-shape provides for inefficient radiation in small waveguides. This is because the array factors are plotted for a normalized waveguide height of 1 for which the sine profile has comparable efficiency to the square and cosine profiles.

The impact of L_c on radiation is illustrated in Fig. 6.7, where the roughness power-array-factor $\left\langle \left|F_{rough}\right|^2 \right\rangle$ is plotted for diverse values of L_c. This power-array-factor is an off-centered ellipsoid of revolution around the z-axis. The larger is the L_c, the more elongated is the ellipsoid along the z-axis with the off-center favoring forward scattering. A large L_c is indicative of strongly represented low spectral-frequencies in the spectral density of roughness. Low spectral-frequencies foster forward scattering at shallow angles.

In this section, we have presented a 3D analysis of scattering losses in microphotonic waveguides. We have derived array factors for the roughness distribution and diverse vertical field-shapes. This allowed us to introduce important mathematical simplifications and to clearly separate the effects of the roughness statistics, the vertical field-shape, and the field polarization on scattering losses. We have shown that the 2D theory strongly overestimates losses of small waveguides. However, as is, the present analysis is strictly valid for low-index-contrast waveguides only as it does not take into account reflections

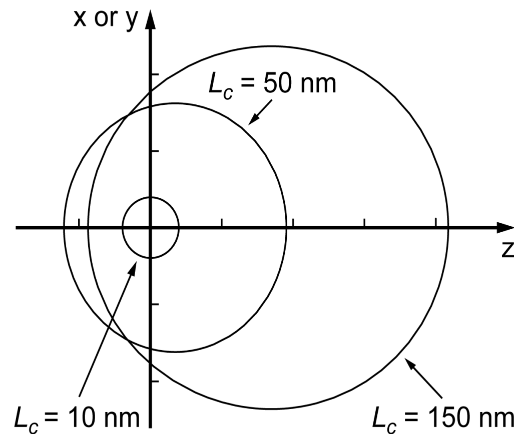

Fig. 6.7 . Cross-section of the roughness power-array-factor for practical values of L_c. The array factor is an ellipsoid of revolution around the z-axis. The exponential model of (6.1) is assumed. σ^2 is a simple scaling factor and does not change the shape of the array factor. For larger L_c, the magnitude of the array factor is greater as more of the roughness is in the range of spatial-frequencies responsible for loss (6.7). Moreover, a large L_c indicates strong low spatial-frequencies of roughness. These are responsible for shallow angles of scattering and explain a more elongated array-factor favoring forward scattering.

of the radiated field from the waveguide boundaries. This is addressed in Sec. 6.5, where the validity of the present analysis is extended to all index-contrasts.

6.5 HIGH INDEX-CONTRAST

6.5.1 Rationale

In the analysis of Sec. 6.4, the waveguide-width and the index-contrast have no explicit effect on the radiation pattern (the width has only a small effect through β in F_{rough}). The effect was lost when we assumed the field in the core to be the guided mode of a perfectly smooth waveguide. It is true that the field in the rough waveguide differs only slightly from the guided mode of the smooth waveguide. Thus, using that guided mode is a proper approximation to compute the field intensity at the rough sidewalls. However, it

results in neglecting the scattered field in the waveguide core and can provide for an inappropriate radiation pattern. In this section, the effect of the waveguide core on the radiation profile is restored, and the validity of the present scattering-loss analysis is extended to all index-contrasts.

To consider the effect of the waveguide core on the radiation profile, the dielectric distribution of Fig. 6.8a needs to be used instead of the uniform dielectric of Sec. 6.4. In short, a smooth waveguide-core is introduced between the radiating sources. The problem is solved using the dyadic Green's functions of the new dielectric distribution. The exact

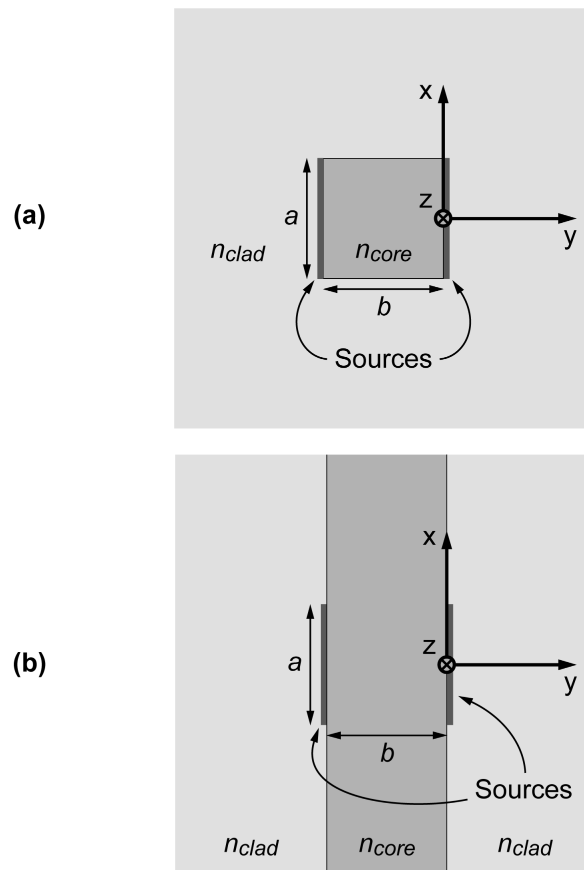

Fig. 6.8. (a) Actual and (b) approximated dielectric distribution used for computation of the radiation profile. (b) is a good approximation of (a) as the sources are right next to waveguide and the extra core material in (b) only affects the radiation profile in small angular intervals near the top and the bottom of the 3D sources.

dyadic Green's functions of this distribution are not analytically known. Fortunately, as the sources are right next to the waveguide, using the dyadic Green's functions of the layered medium [46] shown in Fig. 6.8b is a proper approximation. In fact, the excess core material in the layered medium changes the radiation profile notably only in small angular intervals near the top and the bottom of the 3D sources.

The array factors derived in free space in Sec. 6.4 can be directly applied to the new radiation problem. This is shown conceptually by using the VCM. If one computes the field generated in the core material by a single array element $\vec{J}_{element}(x)$, one can replace the core material by an equivalent polarization-current density associated with the array

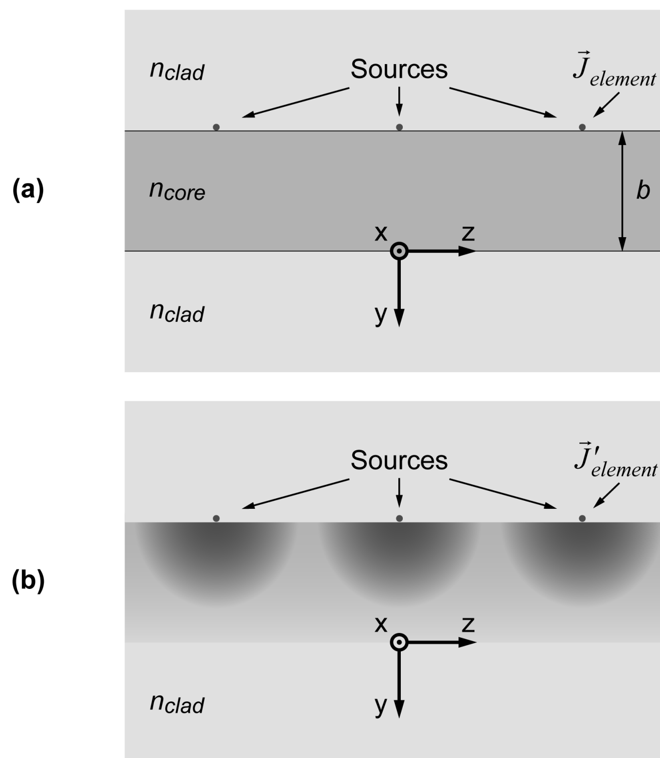

Fig. 6.9 (a) Sources in a one-layer medium. (b) Equivalent case to (a) but in free-space found by defining new sources using the volume-current-method. As the array factors derived in free-space can be applied to the sources presented in (b), and (a) and (b) are mathematically equivalent, the array factors can also be applied to the sources presented in (a).

element. Hence, by using an updated current source $\vec{J}'_{element}(\vec{r})$ as the array element, one can remove the core material and get back to the uniform dielectric where the array factors were derived. This is illustrated in Fig. 6.9. As the case of Fig. 6.9a is perfectly equivalent to Fig. 6.9b, the array factors derived in Sec. 6.4 can all be applied to this new radiation problem. However, the array factors cannot be used to compute the field in the core material (even if very far from $\vec{J}_{element}(x)$) as it is part of the source region of $\vec{J}'_{element}(\vec{r})$ and the array factors can only be used in the far field of $\vec{J}'_{element}(\vec{r})$.

In summary, the array factors derived in a uniform dielectric of index n_{clad} can still be applied to sources in some non-uniform dielectric-profiles given that all sources have the same radiation profile (the same dielectric neighborhood) and the far-field radiation is computed in regions far from n_{core}.

The scattering losses will be obtained by first computing the dyadic Green's functions of the layered medium of Fig. 6.8b. Then, the far field of a point source will be calculated and the appropriate array factors will be applied to obtain the radiation profile of the rough sidewalls. Alternatively, one could obtain the correct radiation profile for a single current element next to the actual waveguide numerically and apply the roughness array factor to obtain the radiated power.

6.5.2 Dyadic Green's Functions in One-Layer Media

6.5.2.1 Coordinate System

The layered medium of interest to scattering loss analysis is often referred to as a one-layer medium. It is presented in Fig. 6.10 along with a general layered medium and the coordinate system used in this section. In Sec. 6.4, the coordinate system was chosen to be consistent with previous 2D scattering loss analyses. In the present section, the coordinate system is rotated around the x-axis to be consistent with previous work on

radiation in planarly layered media [46, 47]. This greatly simplifies the link between the present and prior work and eases the task of reproducing the present analysis. The new Cartesian coordinates are x_c, y_c, and z_c. They are related to x, y, and z by

$$x_c = x,\ \ y_c = -z,\ \text{and}\ \ z_c = y.$$

The new spherical coordinates are r_c, θ_c, and φ_c. They are related to x_c, y_c, and z_c in the same way r, θ, and φ are related to x, y, and z (see Fig. 6.10c).

6.5.2.2 Dyadic Green's Functions in Layered Media

In a source-free region of the planar layered medium of Fig. 6.10a, the dyadic Green's functions are given by [46]

$$\bar{\bar{G}}(\vec{r}_c,\vec{r}_c') = \frac{i}{8\pi^2}\int_{-\infty}^{\infty}\int_{-\infty}^{\infty}\left[\bar{\bar{M}}(\vec{k}_s,\vec{r}_c,\vec{r}_c') + \bar{\bar{N}}(\vec{k}_s,\vec{r}_c,\vec{r}_c')\right]\frac{dk_x dk_y}{k_{mz_c}\left|\vec{k}_s\right|^2}, \tag{6.12}$$

where

$$\begin{aligned} \bar{\bar{M}}(\vec{k}_s,\vec{r}_c,\vec{r}_c') &= \left(\vec{k}_s \times \hat{z}_c\right)\left(\vec{k}_s \times \hat{z}_c\right)e^{i\vec{k}_s\cdot(\vec{r}_s-\vec{r}_s')}F_{\pm}^{TE}(z_c,z_c')\ \text{and} \\ \bar{\bar{N}}(\vec{k}_s,\vec{r}_c,\vec{r}_c') &= \left(\frac{\vec{k}_{n\pm}\times\vec{k}_s\times\hat{z}_c}{i\omega\varepsilon_n}\right)\left(\frac{\vec{k}_{m\pm}\times\vec{k}_s\times\hat{z}_c}{-i\omega\mu_m}\right)e^{i\vec{k}_s\cdot(\vec{r}_s-\vec{r}_s')}F_{\pm}^{TM}(z_c,z_c') \end{aligned} \tag{6.13}$$

are the vector wave functions. Also,

$$\begin{aligned} &k_{iz_c} = \sqrt{k_i^2 - k_s^2},\ \vec{k}_s = k_{x_c}\hat{x}_c + k_{y_c}\hat{y}_c, \\ &\vec{k}_{i\pm} = \vec{k}_s \pm k_{iz_c}\hat{z}_c,\ \text{with} + \text{for}\ z_c > z_c',\ - \text{for}\ z_c < z_c', \end{aligned}$$

and k_i is the free-space wavenumber in region i. The primed coordinates refer to the source position. Note there is a typo at p. 413 of [46] that is fixed in the corresponding expression in (6.13). Moreover,

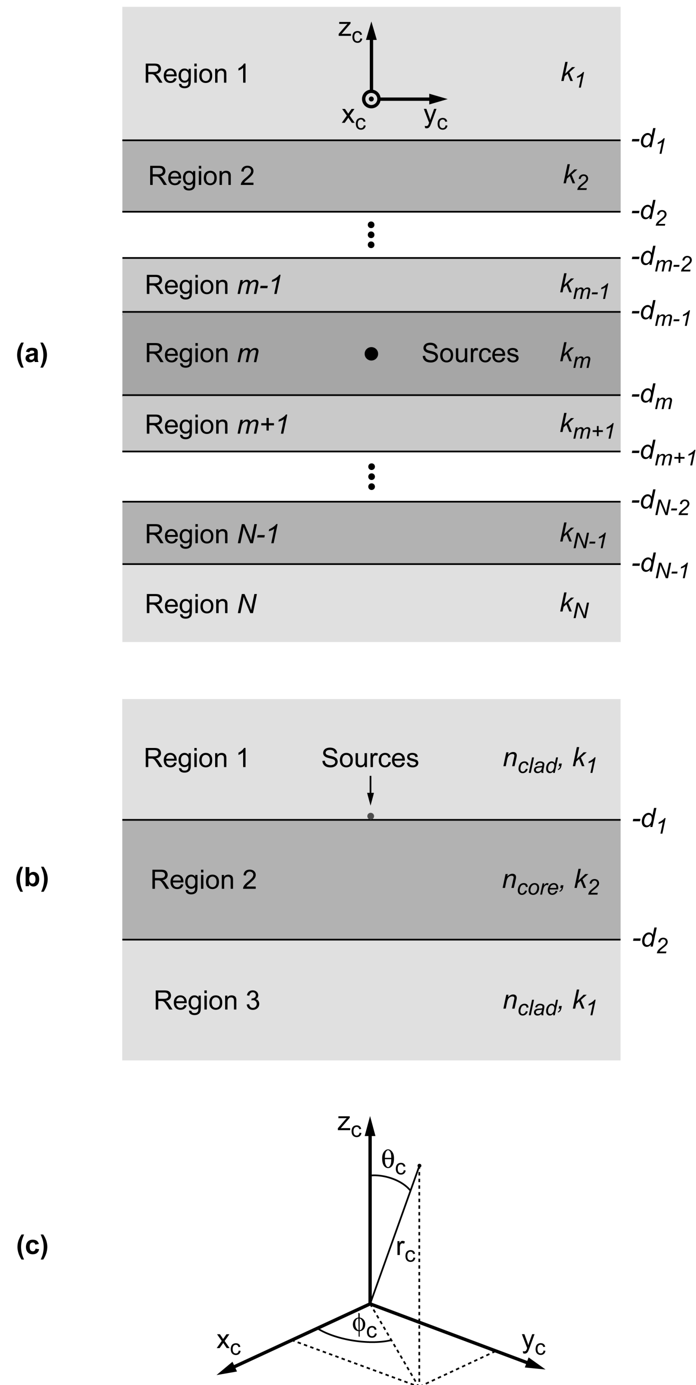

Fig. 6.10. (a) General planar layered-medium. (b) The one-layer medium of interest for scattering loss calculations. (c) Rotated coordinated system used in this section.

$$
\begin{aligned}
F_+(z_c, z_c') = & \left[e^{ik_{nz_c} z_c} + e^{-ik_{nz_c}(z_c+2d_{n-1})} \widehat{R}_{n,n-1} \right] e^{ik_{nz_c} d_n} \widehat{T}_{mn} e^{-ik_{mz_c} d_{m-1}} \\
& \cdot \left[e^{-ik_{mz_c} z_c'} + e^{ik_{mz_c}(z_c'+2d_m)} \widehat{R}_{m,m+1} \right] \tilde{M}_m \tilde{M}_{n+}', \\
& z_c \in \text{region } n,\ z_c' \in \text{region } m,\ n < m,\ z_c > z_c', \\
F_-(z_c, z_c') = & \left[e^{-ik_{nz_c} z_c} + e^{ik_{nz_c}(z_c+2d_n)} \widehat{R}_{n,n+1} \right] e^{-ik_{nz_c} d_{n-1}} \widehat{T}_{mn} e^{ik_{mz_c} d_m} \\
& \cdot \left[e^{ik_{mz_c} z_c'} + e^{-ik_{mz_c}(z_c'+2d_{m-1})} \widehat{R}_{m,m-1} \right] \tilde{M}_m \tilde{M}_{n-}', \\
& z_c \in \text{region } n,\ z_c' \in \text{region } m,\ n > m,\ z_c < z_c',
\end{aligned}
$$

with

$$
\begin{aligned}
\tilde{M}_i &= \left[1 - \widehat{R}_{i,i+1} \widehat{R}_{i,i-1} e^{2ik_{iz_c}(d_i - d_{i-1})} \right]^{-1}, \\
\tilde{M}_{i+}' &= \left[1 - \widehat{R}_{i,i+1}' \widehat{R}_{i,i-1} e^{2ik_{iz_c}(d_i - d_{i-1})} \right]^{-1}, \\
\tilde{M}_{i-}' &= \left[1 - \widehat{R}_{i,i+1} \widehat{R}_{i,i-1}' e^{2ik_{iz_c}(d_i - d_{i-1})} \right]^{-1},
\end{aligned}
$$

express the z-variation of the solution [47]. $\widehat{R}$ and $\widehat{T}$ are the generalized reflection and transmission coefficients. While $\widehat{R}$ is computed from the given layer to the end of the layered medium, $\widehat{R}'$ is computed from the given layer to the source layer only. The generalized reflection and transmission coefficients are found from

$$
\begin{aligned}
\widehat{R}_{i,i+1} &= \frac{R_{i,i+1} + \widehat{R}_{i+1,i+2} e^{2ik_{i+1,z_c}(d_{i+1} - d_i)}}{1 + R_{i,i+1} \widehat{R}_{i+1,i+2} e^{2ik_{i+1,z_c}(d_{i+1} - d_i)}}, \\
\widehat{R}_{ij} &= -\widehat{R}_{ji} \ , \\
\widehat{T}_{ij} &= \prod_{s=i}^{j-1} \frac{T_{s,s+1} e^{ik_{s,z_c}(d_s - d_{s-1})}}{1 - R_{s+1,s} \widehat{R}_{s+1,s+2} e^{2ik_{s+1,z_c}(d_{s+1} - d_s)}},
\end{aligned}
\tag{6.14}
$$

where R and T are the Fresnel reflection and transmission coefficients. They are given by

$$R_{ij}^{TE}=\frac{\mu_j k_{iz_c}-\mu_i k_{jz_c}}{\mu_j k_{iz_c}+\mu_i k_{jz_c}},\ T_{ij}^{TE}=\frac{2\mu_j k_{iz_c}}{\mu_j k_{iz_c}+\mu_i k_{jz_c}},$$
$$R_{ij}^{TM}=\frac{\varepsilon_j k_{iz_c}-\varepsilon_i k_{jz_c}}{\varepsilon_j k_{iz_c}+\varepsilon_i k_{jz_c}},\ T_{ij}^{TM}=\frac{2\varepsilon_j k_{iz_c}}{\varepsilon_j k_{iz_c}+\varepsilon_i k_{jz_c}},$$

where TE refers to waves in the layered medium with no z_c-component of the electric field and TM to waves with no z_c-component of the magnetic field. In (6.13), the TE reflection and transmission coefficients need to be used for $F_{\pm}^{TE}$, and the TM reflection and transmission coefficients need to be used for $F_{\pm}^{TM}$.

6.5.2.3 Leading-Order Solution

Once the adequate reflection and transmission coefficients are computed, the leading order of (6.12) can be found from the method of stationary-phase in two dimensions [48]. The leading order of an integral of the form

$$I=\int_{-\infty}^{+\infty}\int_{-\infty}^{+\infty} e^{irf(k_x,k_y)} g(k_x,k_y)\, dk_x dk_y$$

is given by

$$I\simeq\frac{2\pi e^{irf(k_{x0},k_{y0})} g(k_{x0},k_{y0}) e^{\frac{1}{4}i\pi(\delta+1)\zeta}}{r\sqrt{\left|\frac{\partial^2 f}{\partial k_x^2}\frac{\partial^2 f}{\partial k_y^2}-\left(\frac{\partial^2 f}{\partial k_x \partial k_y}\right)^2\right|_{\substack{k_x=k_{x0}\\ k_y=k_{y0}}}}},\quad r>>1,$$

where

$$\zeta=\operatorname{sgn}\left(\left(\frac{\partial^2 f}{\partial k_y^2}\right)_{\substack{k_x=k_{x0}\\ k_y=k_{y0}}}\right),$$

$$\delta = \operatorname{sgn}\left(\left(\frac{\partial^2 f}{\partial k_x^2}\frac{\partial^2 f}{\partial k_y^2} - \left(\frac{\partial^2 f}{\partial k_x \partial k_y}\right)^2\right)_{\substack{k_x = k_{x0} \\ k_y = k_{y0}}}\right),$$

and k_{x0} and k_{y0} are the stationary-phase points. These are points where

$$\left(\frac{\partial f}{\partial k_x}\right)_{\substack{k_x = k_{x0} \\ k_y = k_{y0}}} = \left(\frac{\partial f}{\partial k_y}\right)_{\substack{k_x = k_{x0} \\ k_y = k_{y0}}} = 0.$$

Applying the method of stationary-phase to the dyadic Green's function in a one-layer medium, we find the stationary-phase points to be

$$k_{x_c,0} = \frac{k_i\left(x_c - x_c'\right)}{\left|\vec{r}_c - \vec{r}_c'\right|},\ k_{y_c,0} = \frac{k_i\left(y_c - y_c'\right)}{\left|\vec{r}_c - \vec{r}_c'\right|}.$$

Then, the leading order of the needed dyadic Green's function in the one-layer medium shown in Fig. 6.10b is given by

$$\overline{\overline{G}}_{1,1}(\vec{r}_c, \vec{r}_c') \simeq \frac{e^{i\left(\vec{k}_{1+,0}\bullet(\vec{r}_c - \vec{r}_c')\right)} k_{1z_c,0} \left(\begin{array}{r}\overline{\overline{C}}_M\left(1 + \widehat{R}_{1,2}^{TE} e^{2ik_{1z_c,0}\left(d_1 + z_c'\right)}\right) \\ + \overline{\overline{C}}_{N+}\left(1 + \widehat{R}_{1,2}^{TM} e^{2ik_{1z_c,0}\left(d_1 + z_c'\right)}\right)\end{array}\right)}{4\pi k_1 \left|\vec{k}_{s0}\right|^2 \left(z_c - z_c'\right)},$$

$\vec{r}_c$ and $\vec{r}_c' \in$ region 1,

$$\overline{\overline{G}}_{1,3}(\vec{r}_c, \vec{r}_c') \simeq -\frac{e^{i\left(\vec{k}_{1-,0}\bullet(\vec{r}_c - \vec{r}_c') + k_{1z_c,0}(d_1 - d_2)\right)} k_{1z_c,0} \left(\overline{\overline{C}}_M \widehat{T}_{1,3}^{TE} + \overline{\overline{C}}_{N-} \widehat{T}_{1,3}^{TM}\right)}{4\pi k_1 \left|\vec{k}_{s0}\right|^2 \left(z_c - z_c'\right)},$$

$\vec{r}_c \in$ region 3, $\vec{r}_c' \in$ region 1,

where

$$k_{iz_c,0} = \sqrt{k_i^2 - k_{s0}^2},$$
$$\vec{k}_{s0} = k_{x_c,0}\hat{x}_c + k_{y_c,0}\hat{y}_c,\ \vec{k}_{i\pm,0} = \vec{k}_{s0} \pm k_{iz_c,0}\hat{z}_c,$$
$$\overline{\overline{C}}_M = \left(\vec{k}_{s0} \times \hat{z}_c\right)\left(\vec{k}_{s0} \times \hat{z}_c\right),$$
$$\overline{\overline{C}}_{N\pm} = \left(\vec{k}_{1\pm,0} \times \vec{k}_{s0} \times \hat{z}_c\right)\left(\vec{k}_{1\pm,0} \times \vec{k}_{s0} \times \hat{z}_c\right)\Big/ k_1^2,$$

and the generalized reflection and transmission coefficients are given by (6.14).

6.5.3 Scattering Losses

Once the dyadic Green's function is computed, the electric field is given by

$$\vec{E}(\vec{r}_c) = i\omega\mu \iiint \overline{\overline{G}}(\vec{r}_c, \vec{r}_c') \cdot \vec{J}(\vec{r}_c') dV',$$

and the far-field Poynting vector is given by

$$\vec{S}(\vec{r}_c) = \frac{1}{2}\mathrm{Re}\left\{ \vec{E}(\vec{r}_c) \times \left(\frac{k_1}{\omega\mu} \hat{r} \times \vec{E}^*(\vec{r}_c) \right) \right\}. \tag{6.15}$$

The scattered power is most easily obtained by first computing the far-field Poynting vector of a point source and then applying the appropriate array factors derived in Sec. 6.4. The far field of a point source $\vec{J}_{pol}$ at the origin reduces to

$$\vec{E}_{pol}(\vec{r}_c) = i\omega\mu\, \overline{\overline{G}}(\vec{r}_c, \vec{0}) \cdot \vec{J}_{pol}\,. \tag{6.16}$$

Then, the ensemble average of the roughness far-field Poynting vector is given by

$$\left\langle \vec{S}_{rough} \right\rangle = \left| F_{shape} \right|^2 \left\langle \left| F_{rough} \right|^2 \right\rangle \vec{S}_{pol}\,,$$

and the scattering losses per unit length of waveguide are given by

$$\frac{P}{2L} = \oiint \left(\frac{\left\langle \vec{S}_{rough} \right\rangle}{2L} \cdot \hat{r} \right) dA\,. \tag{6.17}$$

The coordinate system needs to be considered when using the array factors of Sec. 6.4. As the vertical field-shape array-factors $\left|F_{shape}\right|^2$ exhibit rotational symmetry around the x-axis, their expressions are unchanged when using either r, θ, and φ or r_c, θ_c, and φ_c. On the other hand, the ensemble average of the roughness power array-factor in r_c, θ_c, and φ_c becomes

$$\left\langle \left|F_{rough}\right|^2 \right\rangle = 2\left(2L\right)\tilde{R}(\beta + n_{clad} k_0 \sin(\theta_c)\sin(\varphi_c)). \tag{6.18}$$

In the present analysis, only the two main field components of the first TE-like and TM-like modes are considered and their vertical distributions at the rough boundaries are approximated with cosine and sine vertical field-profiles as shown in Fig. 6.11. The power in the third field component is usually small and we redistribute it among the first two components. The far-field Poynting vector of the TE-like mode reduces to

$$\left\langle \vec{S}^{TE}_{rough} \right\rangle = \frac{\left|F_{cos}\right|^2 \left\langle \left|F_{rough}\right|^2 \right\rangle \left(\vec{S}_y + \gamma_{zy}\vec{S}_z\right)}{1+\gamma_{zy}}, \tag{6.19}$$

where

$$\gamma_{zy} = \int_{-a/2}^{a/2} \left|\vec{\Phi}(x',0)\cdot\hat{z}\right|^2 dx' \Big/ \int_{-a/2}^{a/2} \left|\vec{\Phi}(x',0)\cdot\hat{y}\right|^2 dx'$$

is the power ratio of the z- to the y-component at the rough sidewall. Moreover, $\left|F_{cos}\right|^2$ is given by (6.10), $\left\langle \left|F_{rough}\right|^2 \right\rangle$ is given by (6.18), and $\vec{S}_y$ and $\vec{S}_z$ are given by (6.16) and (6.15) when using

$$\vec{J}_{pol,y} = \vec{J}_{pol,z_c} = -i\omega\varepsilon_0\left(n_{core}^2 - n_{clad}^2\right) v\ \hat{z}_c \text{, and}$$

$$\vec{J}_{pol,z} = \vec{J}_{pol,-y_c} = i\omega\varepsilon_0\left(n_{core}^2 - n_{clad}^2\right) v\ \hat{y}_c \text{ .}$$

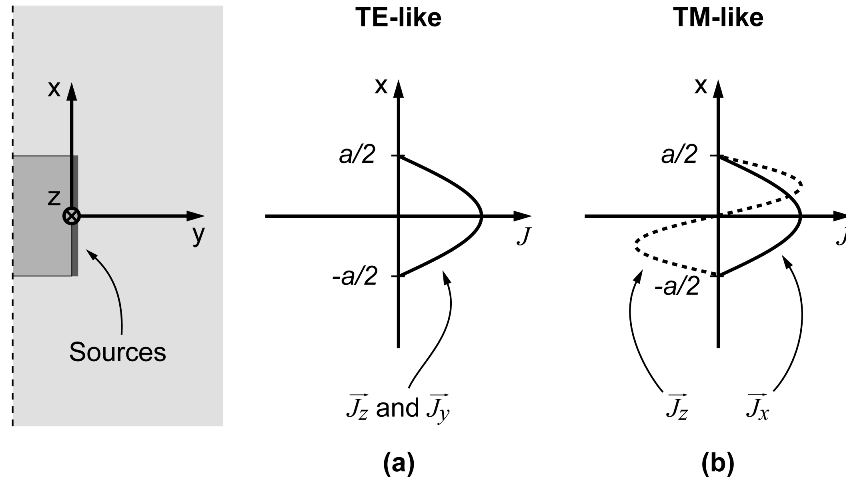

Fig. 6.11. Vertical profile of the current sources used to approximate the shape of the first (a) TE-like and (b) TM-like mode at the rough boundary. Only the two main-field-components of each mode are considered. The schematic on the far left shows half a waveguide for easier understanding of the sources.

The far-field Poynting vector of the TM-like mode reduces to

$$\left\langle \vec{S}_{rough}^{TM} \right\rangle = \frac{\left\langle \left|F_{rough}\right|^2 \right\rangle \left(\left|F_{cos}\right|^2 \vec{S}_x + \gamma_{zx} \left|F_{sin}\right|^2 \vec{S}_z \right)}{1+\gamma_{zx}}, \tag{6.20}$$

where

$$\gamma_{zx} = \int_{-a/2}^{a/2} \left|\vec{\Phi}(x',0)\cdot\hat{z}\right|^2 dx' \Big/ \int_{-a/2}^{a/2} \left|\vec{\Phi}(x',0)\cdot\hat{x}\right|^2 dx'$$

is the power ratio of the z- to the x-component at the rough sidewall. Moreover, $\left|F_{cos}\right|^2$ is given by (6.10), $\left|F_{sin}\right|^2$ is given by (6.11), $\left\langle \left|F_{rough}\right|^2 \right\rangle$ is given by (6.18), and $\vec{S}_x$ is given by (6.16) and (6.15) when using

$$\vec{J}_{pol,x} = \vec{J}_{pol,x_c} = -i\omega\varepsilon_0 \left(n_{core}^2 - n_{clad}^2\right) v \, \hat{x}_c \, .$$

Finally, scattering losses are computed for each mode by using (6.17) with (6.19) and (6.20).

In this section, we presented a 3D analysis of scattering losses due to sidewall roughness in microphotonic waveguides valid for all index-contrasts. The radiation profile was approximated by the one of a one-layer medium. First, the needed dyadic Green's functions were computed. Then, the far-field Poynting vector of a point source was obtained and appropriate array factors were applied to find the far-field Poynting vectors of the first TE-like and TM-like modes. These can be numerically integrated to obtain the radiation loss. This integration is performed in Sec. 6.6 where numerical results of scattering losses are presented.

6.6 NUMERICAL RESULTS

Using the analysis derived in Sec. 6.5, scattering losses for SiON, Si_3N_4, and Si waveguides buried in a SiO_2 cladding are computed for various waveguide cross-sections and field polarizations. The results are presented in Figs. 6.12 to 6.17, where the exponential model of roughness presented in (6.3) is employed with $L_c = 50\,\text{nm}$. The propagation constant β and the mode profile were numerically computed using a vectorial mode-solver. The mode profile provided v, γ_{zy} and γ_{zx}. However, the approximate sine and cosine vertical field-profiles were employed for the loss calculations. The integration of the radiation profile of each mode (see (6.17)) was performed using an adaptive lobotto quadrature [49].

In Figs. 6.12 to 6.14, to illustrate radiation efficiency, the calculation results are normalized to scattering losses obtained with the 2D analysis of [21] (losses derived only for the x-polarization). We believe a factor of 2 could be missing at Eq. 16a of [21]. However, this does not compromise the results of [39] as an extra factor of 2 is present at Eq. 9 of [39]. The numerically computed propagation constant and field intensity at the sidewalls were used in the 2D calculation.

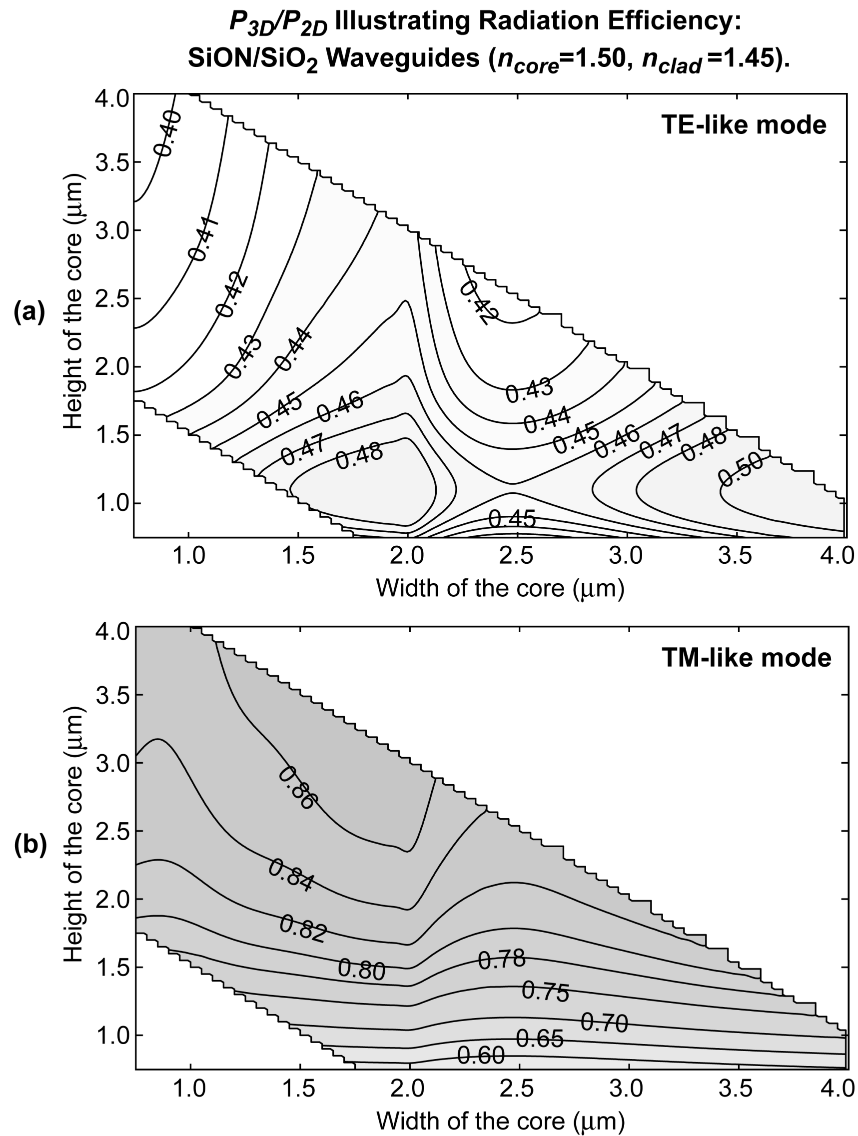

Fig. 6.12 Radiation efficiency of (a) the TE-like mode and (b) the TM-like mode of SiON (n_{core}=1.50) waveguides embedded in a SiO_2 (n_{clad}=1.45) cladding. $\lambda = 1550\,\text{nm}$ and an exponential model of roughness with $L_c = 50\,\text{nm}$ are assumed. To illustrate how the radiation efficiency changes with the waveguide cross-section, the scattering losses obtained with the present 3D analysis are normalized to the losses found from 2D theory of [21] (losses only derived for the x-polarization). For instance, the loss in the TE like mode is less than half of the loss predicted by the 2D theory.

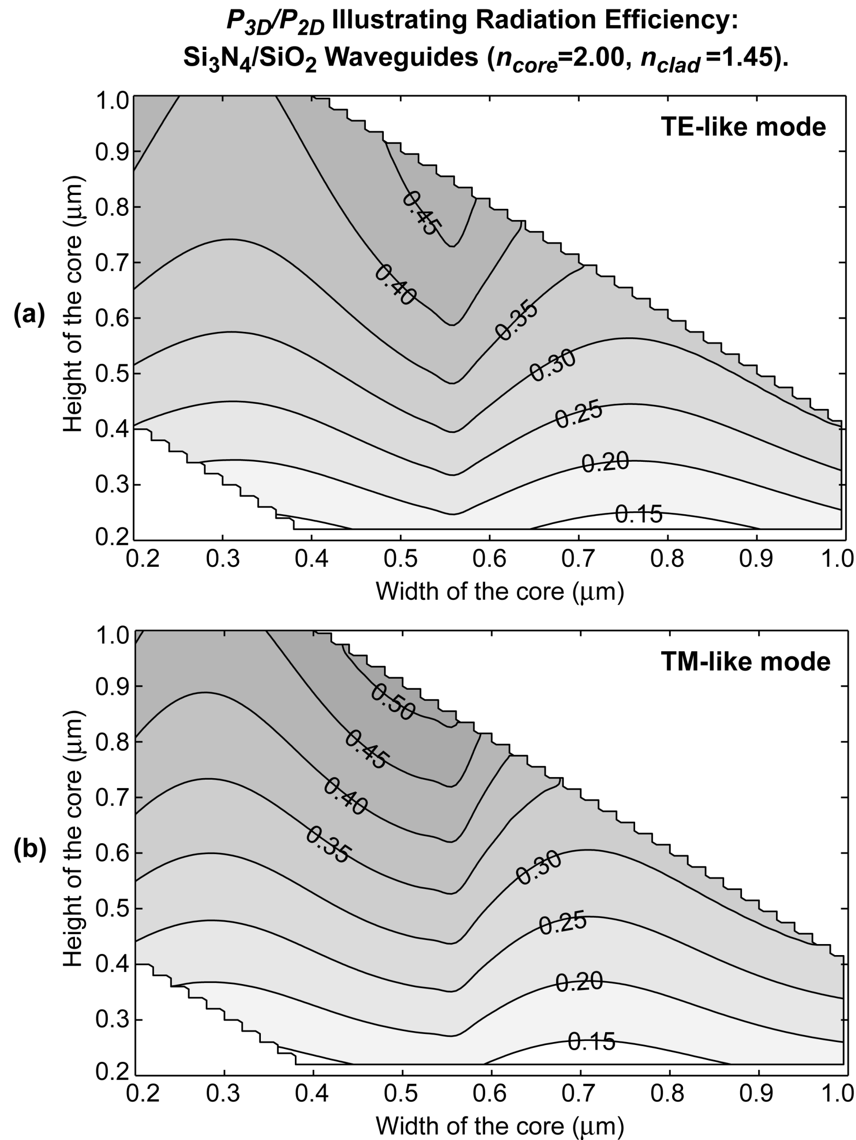

Fig. 6.13 Radiation efficiency of (a) the TE-like mode and (b) the TM-like mode of Si_3N_4 (n_{core}=2.00) waveguides embedded in a SiO_2 cladding. $\lambda = 1550\,\text{nm}$ and an exponential model of roughness with $L_c = 50\,\text{nm}$ are assumed. To illustrate how the radiation efficiency changes with the waveguide cross-section, the scattering losses obtained with the present 3D analysis are normalized to the losses found from 2D theory of [21] (losses only derived for the x-polarization).

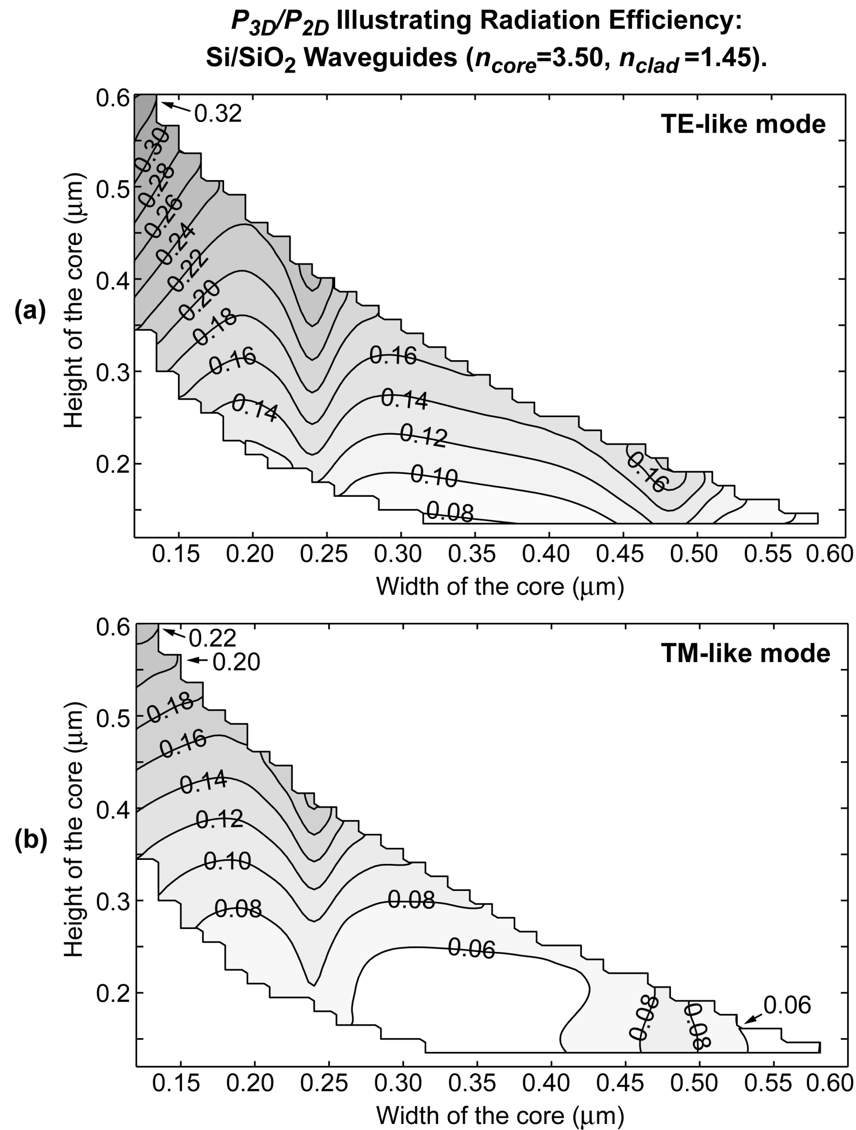

Fig. 6.14 Radiation efficiency of (a) the TE-like mode and (b) the TM-like mode of Si (n_{core}=3.50) waveguides embedded in a SiO_2 cladding. $\lambda = 1550\,\text{nm}$ and an exponential model of roughness with $L_c = 50\,\text{nm}$ are assumed. To illustrate how the radiation efficiency changes with the waveguide cross-section, the scattering losses obtained with the present 3D analysis are normalized to the losses found from 2D theory of [21] (losses only derived for the x-polarization). For instance, the loss in the TM-like mode of a 200-nm-high and 400-nm-wide Si waveguide is less than 6% of the loss predicted by the 2D theory.

In Figs. 6.15 to 6.17, we report the expected scattering losses in dB/cm normalized to the roughness variance in nm^2. The loss in dB/cm can be restored by multiplying the appropriate factor given in the figure by the expected roughness variance in nm^2. In Figs. 6.12 to 6.17, the calculation domain is restricted to monomode waveguides with acceptable mode confinement.

Finally, Fig. 6.18 shows the effect of L_c on scattering losses for the three index-contrasts investigated. The scattering losses are normalized to scattering losses obtained for the given waveguide with $L_c = 50\,\text{nm}$.

6.7 DISCUSSION

6.7.1 Trends

As shown in Fig. 6.14b, the 2D theory can over-estimate scattering losses of small waveguides by more than an order of magnitude. Even so, it is relatively appropriate for the TM-like mode of tall SiON waveguides. Note that the 2D theory used as reference was derived for the x-polarization only and is, hence, only expected to be appropriate for the TM-like modes of our waveguides. It has also been used to normalize the radiation of the TE-like mode to provide an adequate comparison between radiation efficiencies of TE- and TM-like modes. From Figs. 6.15 to 6.17, we see that the index contrast has the strongest influence of all waveguide parameters on scattering losses, which vary by 5 orders of magnitude (in dB scale) within the three cases investigated. The main difference between trends in Figs. 6.12 to 6.14 and Figs. 6.15 to 6.17, is that Figs. 6.15 to 6.17 include the trends of the field-intensity at the rough sidewalls, which are normalized out in Figs. 6.12 to 6.14.

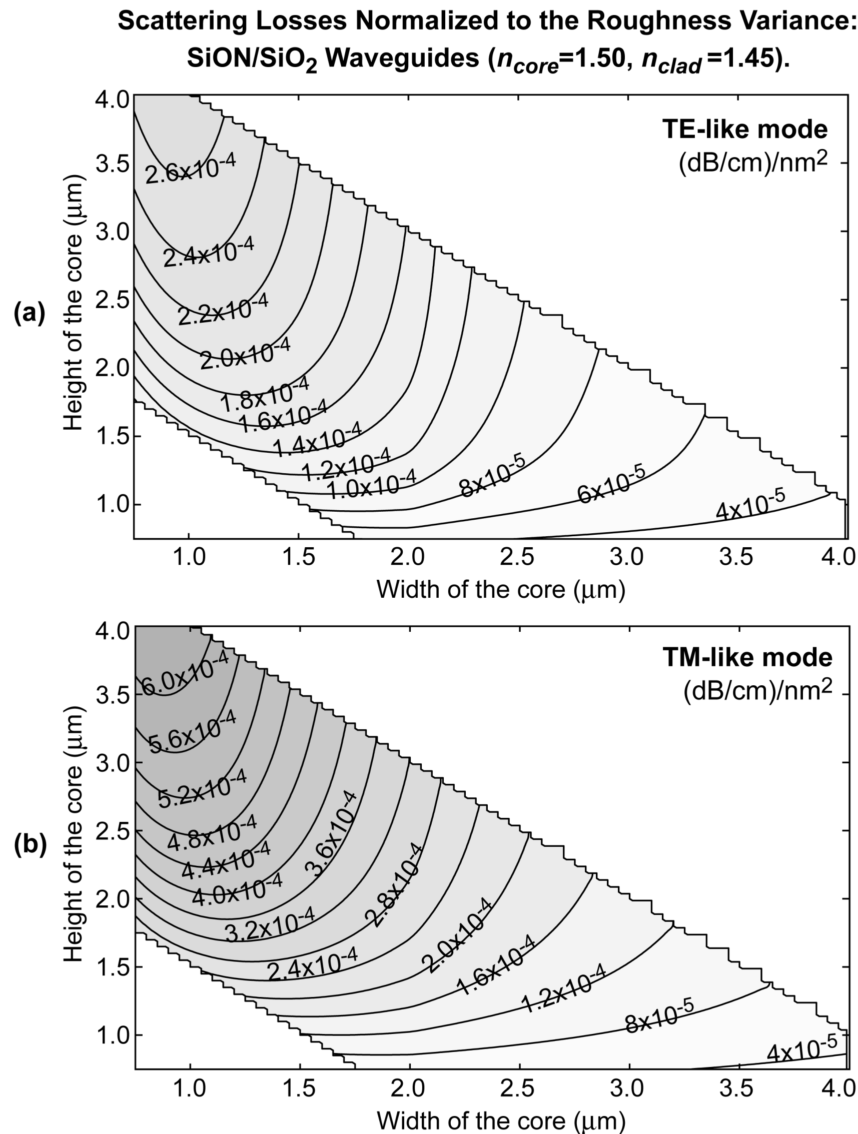

Fig. 6.15 Scattering losses in dB/cm normalized to the roughness variance in nm^2 for (a) the TE-like mode and (b) the TM-like mode of SiON (n_{core}=1.50) waveguides embedded in a SiO_2 (n_{clad}=1.45) cladding. $\lambda = 1550\,\text{nm}$ and an exponential model of roughness with $L_c = 50\,\text{nm}$ are assumed. The scattering losses can be restored by multiplying the given quantity by the expected variance in nm^2. For instance, if one expects $\sigma^2 = 10\,\text{nm}^2$, the expected loss in the TM-like mode of a 2-µm-high and 2-µm-wide SiON waveguide will be around 0.028 dB/cm.

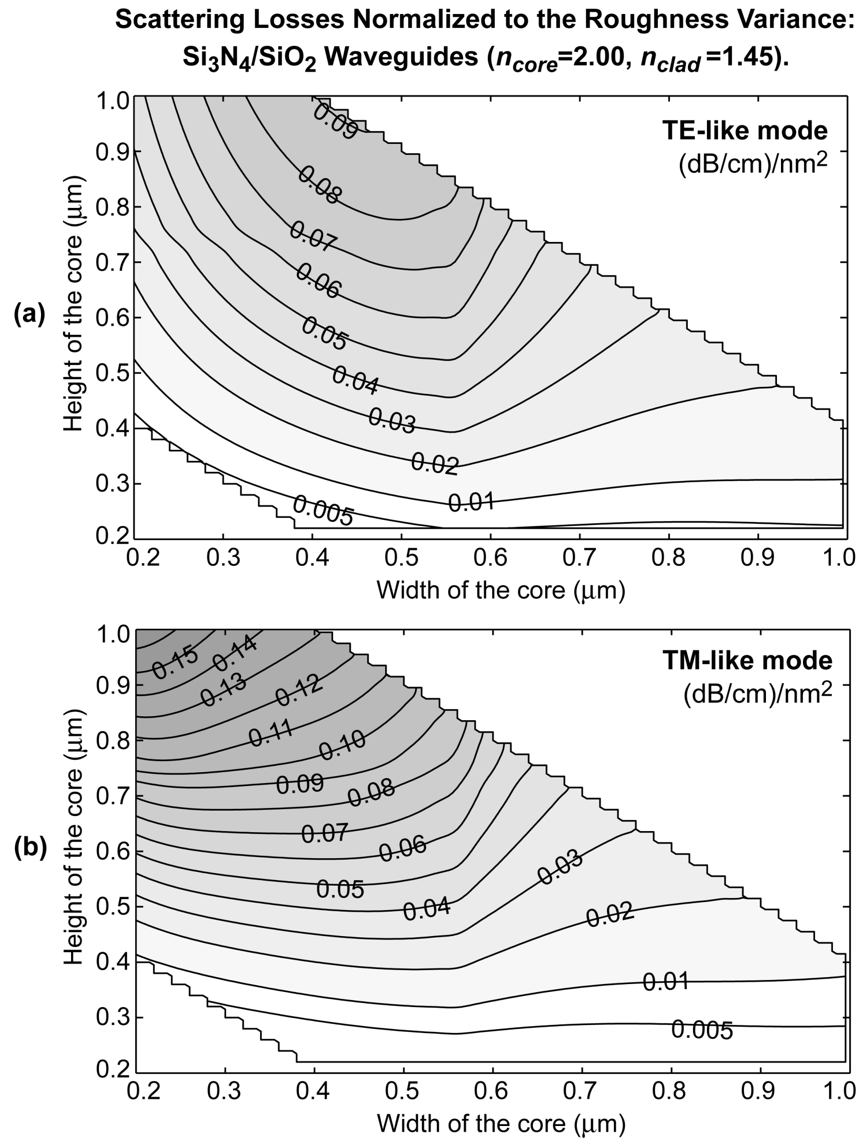

Fig. 6.16 Scattering losses in dB/cm normalized to the roughness variance in nm^2 for (a) the TE-like mode and (b) the TM-like mode of Si_3N_4 (n_{core}=2.00) waveguides embedded in a SiO_2 (n_{clad}=1.45) cladding. $\lambda = 1550\,\text{nm}$ and an exponential model of roughness with $L_c = 50\,\text{nm}$ are assumed. The scattering losses can be restored by multiplying the given quantity by the expected variance in nm^2.

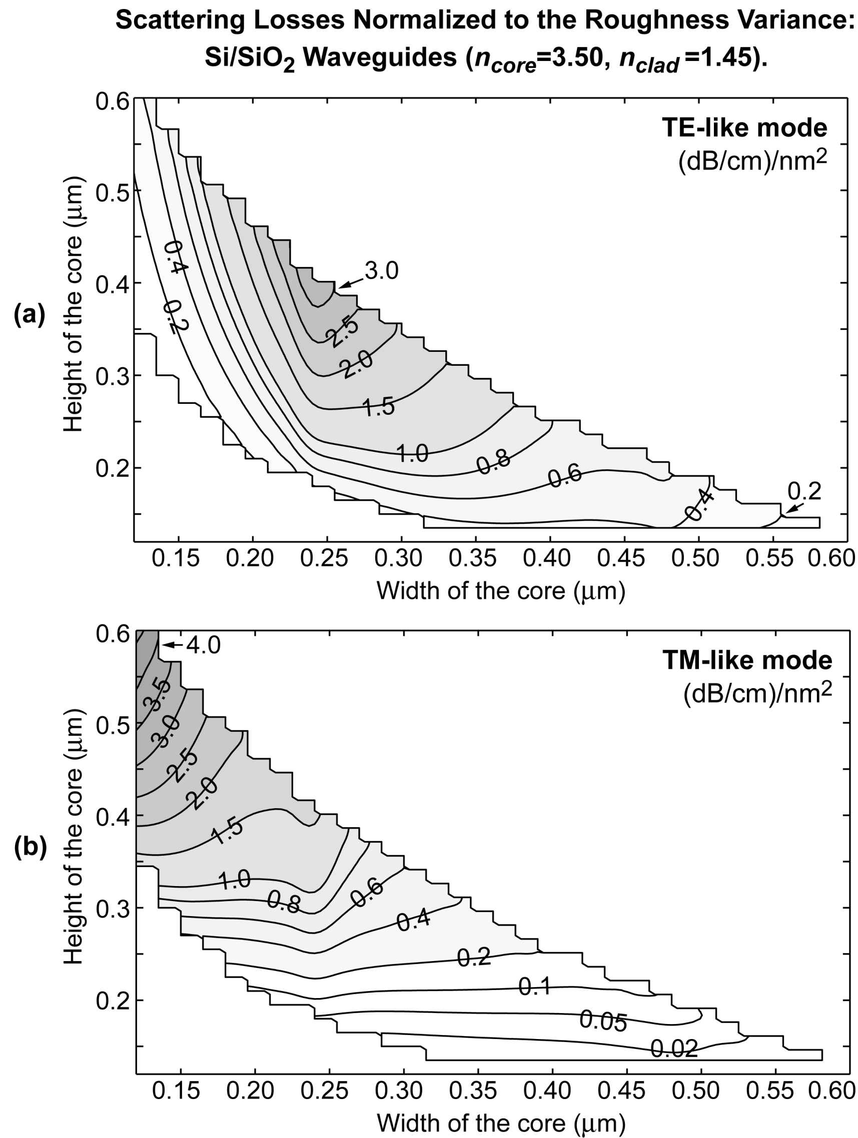

Fig. 6.17 Scattering losses in dB/cm normalized to the roughness variance in nm^2 for (a) the TE-like mode and (b) the TM-like mode of Si (n_{core}=3.50) waveguides embedded in a SiO_2 (n_{clad}=1.45) cladding. $\lambda = 1550\,\text{nm}$ and an exponential model of roughness with $L_c = 50\,\text{nm}$ are assumed. The scattering losses can be restored by multiplying the given quantity by the expected variance in nm^2. For instance, if one expects $\sigma^2 = 10\,\text{nm}^2$, the expected loss in the TE-like mode of a 200-nm-high and 400-nm-wide Si waveguide will be around 7 dB/cm.

Within a given index contrast, the radiation efficiency and the scattering losses are mainly influenced by the waveguide height. The radiation efficiency can change by a factor of 4 (Fig. 6.14a) and the scattering losses (in dB scale) can change by a factor of 20 (Fig. 6.17b) with stronger radiation for tall sidewalls. The importance of the waveguide height was already illustrated in Figs. 6.4 and 6.5 and is consistent with the present findings. For instance, the maximum in radiation efficiency observed for the TE-like mode of 1.2-μm-high SiON waveguides (Fig. 6.12a) is consistent with the maximum in radiation efficiency of the y-polarization with cosine-field-profile shown in Fig. 6.4b.

The waveguide width has a smaller effect on the radiation efficiency than the height. Nonetheless, the width produces radiation efficiency oscillations with stronger radiation for 1.9- and 3.8-μm-wide SiON-waveguides, 0.55-μm-wide Si_3N_4-waveguides, and 0.24- and 0.48-μm-wide Si-waveguides. Moreover, the width has a strong influence on the power radiated through the field-intensity at the rough sidewalls.

Scattering losses show significant polarization dependence. For SiON waveguides, the polarization dependence is dominated by the radiation efficiency, which is higher for the TM-like mode. The TM-like mode is mainly x-polarized while the TE-like mode is mainly y-polarized. From Fig. 6.4, we see that the radiation efficiency of the x-polarization is about twice the radiation efficiency of the y-polarization and is consistent with the TM-like-mode radiation being about twice the TE-like-mode radiation. In contrast, for Si waveguides, the radiation efficiency of the TM-like mode is about half of the radiation efficiency of the TE-like mode. From Fig. 6.4, we see that the radiation efficiencies of the x- and y-polarizations are about the same for small waveguides and cannot account for this polarization dependence. Nonetheless, the high index-contrast provides for a strong z-component of the field. From Fig. 6.5a, for small waveguides, we see that the cosine-field-profile of the z-component of the TE-like mode offers much

stronger radiation than the sine-field-profile of the z-component of the TM-like mode. This dominates the polarization dependence of the radiation efficiency. For the actual scattering losses, the polarization dependence in Si waveguides is dominated by the field-intensity at the sidewalls. When using the VCM, one is interested in the field intensity at the sidewalls but only from the side of the waveguide core. For the TE-like mode, it drops dramatically in Si waveguides narrower than 0.25 μm.

If scattering losses are a concern, tall and narrow Si_3N_4- and Si-waveguides should be avoided when using the TM-like mode while close-to-square Si_3N_4- and Si-waveguides should be avoided when using the TE-like mode. For SiON waveguides, employing the TE-mode with wide waveguides will minimize scattering losses. In any index contrast, when both modes are employed, considerable polarization-dependent loss may be experienced.

The impact of L_c on scattering losses is depicted in Fig. 6.18. As shown in Sec. 6.4.2, L_c has a small effect on the radiation pattern and, thus, on radiation efficiency. However, it has a significant impact on the total loss. For practical values of L_c the larger is the L_c, the stronger are the roughness spatial-frequencies responsible for scattering losses (see (6.7)), and the stronger is the radiation.

Proper comparison between calculation results and experimental loss measurements found in literature is difficult as a rigorous characterization of roughness statistics and propagation loss is needed. Furthermore, one has to be reasonably confident that the propagation-loss is scattering-loss limited. Nonetheless, we can say that the presented calculation results are consistent with experiments partly reported in [50].

As with all scattering-loss analyses, the present analysis is more accurate for computing low scattering-losses than for computing high scattering-losses. In fact, it is in part a perturbative approach as the field at the sidewalls and the propagation constant of

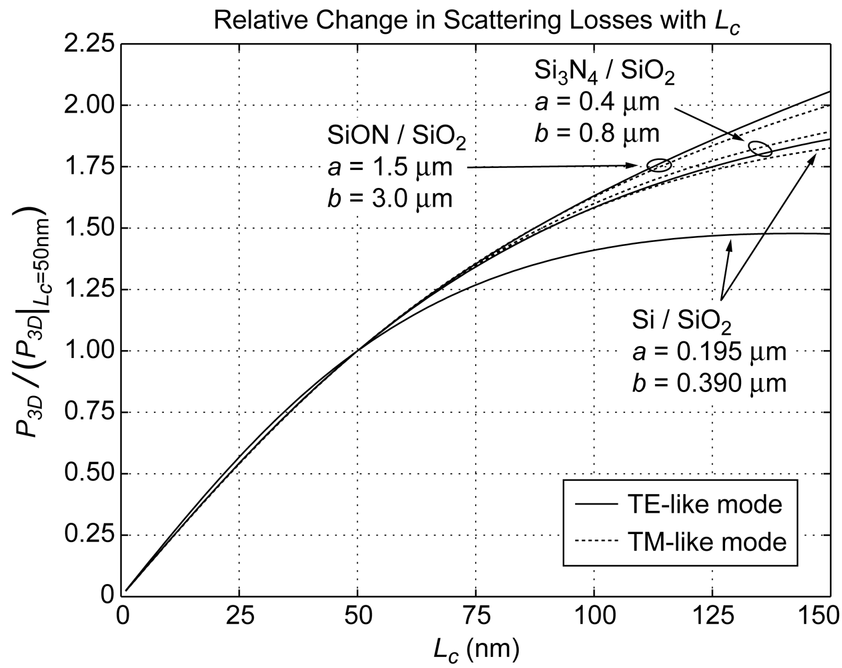

Fig. 6.18 Impact of L_c on scattering losses. Three waveguides are investigated: a 1.5-µm-high and 3.0-µm-wide SiON (n_{core}=1.50) waveguide, a 0.4-µm-high and 0.8-µm-wide Si_3N_4 (n_{core}=2.00) waveguide, and a 0.195-µm-high and 0.390-µm-wide Si (n_{core}=3.50) waveguide. All waveguides are surrounded by a SiO_2 (n_{clad}=1.45) cladding. Scattering losses are normalized to the losses obtained with $L_c = 50\,\text{nm}$ for the waveguide cross-section and mode investigated.

the rough waveguide are assumed unchanged from the case of a perfectly smooth waveguide. Thus, the roughness amplitude needs to be sufficiently small not to alter the guided-mode-shape significantly. In practice, this is not a limiting factor as the accuracy of the loss estimate, even for high-loss waveguides, will be limited by the difficulty to accurately predict and measure the spectral density of sidewall roughness.

6.7.2 Quick Scattering-Loss Estimates.

A wide variety of graphs were generated for the reader to be able to obtain scattering-loss estimates without handling of the derived mathematical expressions. We now present three approaches to obtain quick estimates of power loss. In all cases, an estimate of the

expected roughness statistics is required. It can be obtained by using the method presented in Chapter 4. Otherwise, an exponential model of roughness with $\sigma^2 = 10\,\text{nm}^2$ and $L_c = 50\,\text{nm}$ can be a fair estimate of roughness statistics for current optimized fabrication processes.

If the waveguide of interest falls within one of the three cases thoroughly studied in Sec. 6.6, an estimate can be obtained by using Figs. 6.15 to 6.18. First, the expected scattering losses are obtained by multiplying the expected σ^2 by the scattering losses normalized to the roughness variance obtained from Figs. 6.15 to 6.17. This loss estimate will be valid for $L_c = 50\,\text{nm}$. For other L_c, the loss estimate can be approximately corrected by multiplying it by the appropriate correction factor of Fig. 6.18.

For low index-contrast waveguides (lower index-contrast than the $SiON/SiO_2$ waveguides investigated in Sec. 6.6), a loss estimate can be obtained by integrating eq. 16a of [21], multiplying by two, and applying the appropriate correction factor of Figs. 6.4 and 6.5. The field at the rough sidewalls can be obtained from a mode solver or from the effective-index method [40]. For very low index-contrast waveguides, the z-component of the mode can usually be neglected. Otherwise, it can be taken into account by performing a weighted average of the appropriate correction factors of Figs. 6.4 and 6.5. The weights should reflect the power in each component at the rough boundary normalized to the total power at the rough boundary.

For high-index contrast waveguides with complex dielectric-profiles, a loss estimate could be obtained by first numerically calculating the radiation profile of a single current-element next to the waveguide (of the form of (6.8)) using 3D far-field finite-difference-time-domain simulations [51] and, then, applying the roughness power-array-factor of (6.6) or (6.18).

6.7.3 Extension of the Roughness Model

For simplicity, we considered the top and bottom walls to be perfectly smooth and the two sidewalls to have the same roughness statistics and to be mutually uncorrelated. The ensemble average of power loss due to two uncorrelated rough surfaces is simply the addition of the power loss due to each individual surface. Thus, in the present analysis, both sidewalls can have different roughness statistics. The resulting loss will be found by adding one-half of the loss obtained with the present analysis using the first roughness statistics to one-half of the loss obtained with the present analysis using the second roughness statistics.

Any roughness on the top and the bottom walls may also be treated with the present analysis if it can be considered as mutually uncorrelated and uncorrelated to the sidewall roughness. This assumption holds in most cases as the top and bottom roughness mostly comes from the deposition process and the sidewall roughness comes from the patterning process. It is only in select polycrystalline materials that the top or bottom roughness may be partially correlated to the sidewall roughness. When uncorrelated, the top and bottom roughness can be considered by adding the scattering losses due to the top and bottom walls to the scattering losses due to sidewall roughness. The scattering losses due to the top and bottom walls can be calculated with the present analysis by turning the waveguide on the side and considering it as sidewall roughness (with top and bottom considered smooth).

In summary, the present analysis can be employed to estimate scattering losses even if both sidewalls are known to have different roughness statistics or the top and bottom walls are known to be notably rough.

6.7.4 Propagation Loss in Fabricated Filters

6.7.4.1 Propagation Loss Analysis

The propagation loss in fabricated microring filters was estimated to be around 10 dB/cm from fits of the filter spectral response. More accurate measurements on large rings with 45-μm-radii and 900-nm-wide ring-waveguides indicated a propagation loss of 9 ± 1 dB/cm for the TE-like mode and 7 ± 2 dB/cm for the TM-like mode. In addition, the cut-back method was used to evaluate propagation loss on paperclip structures and provided a loss measurement of 10 ± 5 dB/cm for the TE-like mode and 6 ± 5 dB/cm for the TM-like mode of 900-nm-wide waveguides, and 8 ± 4 dB/cm for the TE-like mode and 5 ± 4 dB/cm for the TM-like mode of 700-nm-wide waveguides.

From the scattering loss computations of Sec. 6.6 and the spectral density measurements of Sec. 5.4, the scattering losses due to sidewall roughness are expected to be below 1 dB/cm. Moroever, the top-surface roughness of the waveguides was measured with an atomic-force microscope (AFM) and a roughness variance of 0.25 nm^2 was found. Such variance is expected to generate negligible scattering losses due to top-surface roughness independently of its correlation length.

The absolute propagation loss is more difficult to accurately predict and measure than the relative propagation loss between waveguide modes. In particular, the present scattering-loss analysis does not take into account reflections of the radiated field at the air-to-SiO_2 boundary as the analysis was derived for over-clad rectangular waveguides. To enhance the confidence in our analysis, we investigate the measured and calculated ratios (in dB scale) of the TE-like-mode loss to the TM-like-mode loss. Results are summarized in Table 6.1. In short, the polarization dependence of propagation loss point towards material loss and not scattering losses as being the dominant source of loss. Hence, the index contrast of SiN waveguides is not high enough for scattering losses to

TABLE 6.1
MEASURED AND EXPECTED POLARIZATION DEPENDENCE OF PROPAGATION LOSS

Parameter	TE loss over TM loss (in dB scale)
Measured ratio	1.5
Ratio predicted from sidewall roughness	3.0
Ratio predicted from top surface roughness	0.53
Ratio predicted from material loss	1.5

be the limiting loss mechanism when the fabrication process is well optimized.

Fabrication and characterization of shallow-etched ridge SiN waveguides confirmed material loss as being the main source of loss. In shallow-etched ridge waveguides, the field overlap with the small sidewalls is negligible so scattering losses are always small. Therefore, the propagation loss is limited by the material loss and was measured to be 8 ± 2 dB/cm at 1510 nm and 7 ± 2 dB/cm at 1610 nm. This is consistent with the loss measured on filter waveguides and confirms material loss as being the main source of loss.

6.7.4.2 Potential Sources of SiN Material Loss

Near-infrared optical loss in silicon-rich silicon-nitride has not been notably investigated in the literature. This material is mainly used for its mechanical properties in micro-electro-mechanical systems so more attention is given to its mechanical and electrical properties. On the other hand, stoichiometric silicon nitride (Si_3N_4) has attracted significant attention for microphotonic devices and propagation loss below 1 dB/cm was reported in the literature [52]. Therefore, at first sight, the SiN material loss should be

related to the excess Si in the material.

In general, material loss is due to one of the two following causes. First, the optical wave can be scattered by refractive index inhomogeneity. The scattering can be analyzed by coupling of modes as is scattering due to sidewall roughness and the mode-matching condition of (6.7) needs to be satisfied. Hence, the index inhomogeneity must have spectral components with spatial periods approximately between 0.5 and 6 μm to generate loss. Second, the material may absorb optical photons to reach a higher energy state. This is of particular importance when the photon energy corresponds approximately to the transitional energy required between two electronic or vibrational energy states of the material.

One of the best ways to identify the cause of loss is to look at its spectral signature. Loss due to scattering is spectrally broad and grows monotonically towards the short wavelengths (in the spectral range of interest). Loss due to absorption usually shows a sharper spectral signature with a clearly defined loss peak. The loss measured in the shallow-etched SiN waveguides is mostly spectrally flat in the 1510-1610 nm spectral range investigated. It slowly decreases from 8 ± 2 dB/cm at 1510 nm to 7 ± 2 dB/cm at 1610 nm.

The energy of optical photons in the C-band is around 0.8 eV and their frequency usually corresponds to the resonant frequencies of atomic bonds stretching. Of particular interest are the N-H bonds which have been widely studied in silicon nitrides and oxynitrides deposited by chemical vapor deposition as they show an absorption peak around 1510 nm (changes with material composition) [53]. This absorption peak is relatively spectrally sharp, however, and the material loss should significantly decreases by 1610 nm. This is not observed in our SiN and point toward N-H bond not being the main loss mechanism.

Concentrating on the possible effects of the excess Si in the material, two possibilities come to mind. First, Si nanocrystals have been proposed as a possible source of loss by scattering in SiN [54]. Under special annealing condition, the excess Si may precipitate and create the index inhomogeneity required for optical loss [55]. Second, the electronic bandgap of SiN is around 3-4 eV (1-2 eV smaller than in stoichiometric nitride) [56]. As SiN is an amorphous material, the band gap is not well defined. Hence, there is an absorption tail expanding far from the bandgap. Nonetheless, the absorption tail should be negligible in the near infrared. However, dangling Si-bonds due to the excess Si in the material can form defect states in the electronic bandgap. These states could have a broad spectral signature and create sufficient electronic absorption to explain the optical loss.

At this early stage, electronic defect states seem the most probable cause of material loss in SiN. To further investigate the problem, wide (~ 600 to 2000 nm) spectral loss measurements are needed. These have not yet been available as various waveguide structures are required for the various wavelengths and a new laser source is needed for characterization.

6.7.5 Scattering Losses in Microring Resonators

The scattering loss analysis derived in this Chapter is, strictly speaking, valid for straight rectangular waveguides only. For microring resonators, a new roughness array-factor is required as the radiation pattern of a microring is different from the one of a straight waveguide. The array factor could be derived from the analysis of scattering losses in microring resonators derived in [57]. Moreover, the radiation pattern of single roughness element would need to be re-derived for cylindrically layered media. Then, updated loss contour maps can be computed. This is left for future work. In this section, we discuss the

expected qualitative changes in scattering resulting from the waveguide curvature.

In bent waveguides, the spatial frequencies of roughness generating loss are not limited to the spectral band defined by the mode-matching condition of (6.7). The spatial frequencies of (6.7) radiate the most effectively but all spatial frequencies can now create loss through tunneling radiation. The efficiency of tunneling radiation decreases rapidly for spatial frequencies away from the spectral band defined at (6.7) and for decreasing waveguide curvature. Hence, tunneling radiation is not expected to change the loss by scattering radically but needs to be taken into account for appropriate loss estimates.

Scattering losses in microring waveguides will be quantitatively different from losses in straight waveguides. However, the major loss trends reported in Sec. 6.7.1 should remain mostly unchanged. In particular, power loss is still expected to be mainly influenced by index-contrast and waveguide-height. Interestingly, a small waveguide height is expected to increase tunneling radiation, which should partially offset the decrease in power loss at small waveguide heights due to the drop of radiation efficiency for short radiating elements.

6.7.6 Scattering Losses due to Lithographic Discretization

Maskless lithography systems operate by filling grids of pixels. The minimum pixel-size is usually defined by the resolution of the digital-to-analog converter and the field-size used. Often, writing speed concerns impose a larger pixel-size than the minimum so a multiple of the minimum pixel-size is used. When exposing a waveguide at an angle with the lithographic grid, deterministic sidewall roughness will be introduced. This is illustrated in Fig. 6.19. The roughness spectral components responsible for loss are easily transferred by replication techniques such as photolithography and nano-imprint lithography. Hence, lithographic discretization is as much of a concern for mask

manufacturing as it is for direct writing.

In this section, we estimate an upper-bound of loss induced by lithographic pixelization. The 3D analysis derived in Sec. 6.5 cannot be directly applied to the present case. First, the roughness on the two sidewalls is strongly correlated. Then, the spectral density of roughness due to lithographic discretization is not continuous but rather formed of isolated spectral peaks. In short, a new roughness array-factor is required. The new array factor can be derived from the 2D theory of [36] and an appropriate 3D estimate obtained. To obtain an upper bound of loss, however, a 2D estimate is sufficient. This is done in present work to coarsely estimate the effect and the full 3D estimate is left for future work.

The lithographic pixel size is usually well below 100 nm (6 nm in the fabricated filters of Chapter 3). The spectral components of roughness responsible for optical loss have spatial periods between 0.5 and 6 μm. Hence, the major spectral components of deterministic roughness (with spatial periods on the order of a pixel) do not radiate. It is the low spectral components created by arrangements of pixels that are responsible for

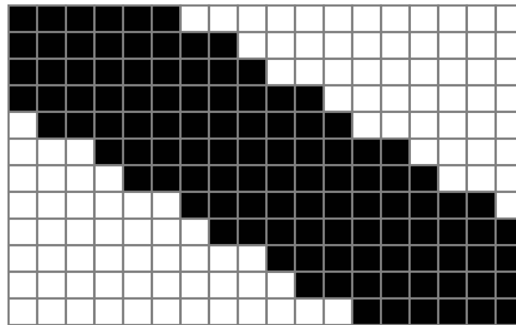

Fig. 6.19 Illustration of deterministic roughness introduced by lithographic pixelization. The lithographic grid is filled-in to define a waveguide. The pixel size is exaggerated for clarity. When the waveguide is at an angle with the grid, deterministic sidewall roughness is introduced and can generate optical loss. As the beam size is usually bigger than the pixel size, the high spectral components of roughness will be washed out in practice and the line will appear smoother than depicted.

optical loss. When the slope of a waveguide with respect to the lithographic grid is described by a simple fraction (1/2, 2/3, 3/5, etc.), there will be no spectral components with long-enough spatial periods to generate loss. Therefore, when the angle between the waveguide and the lithographic grid reaches 45, 33.69, or 30.96 degrees, for instance, there will be no radiation. Lithographic discretization is a concern when the slope of the waveguide with respect to the lithographic grid is described by a complex fraction (121/1813 for example). Then, the spectral components required for loss will be present in the resulting waveguide.

Preliminary calculations showed that, for common fabrication parameters used in direct-write scanning e-beam lithography, loss induced by lithographic pixelization is most often at least one order of magnitude smaller than loss due to stochastic sidewall roughness. As expected, the loss is strongly oscillating when the angle between the waveguide and the lithographic grid is scanned.

6.8 CONCLUSION

We have presented a leading order 3D analysis of scattering losses due to sidewall roughness in straight rectangular dielectric-waveguides, valid for any refractive-index-contrast and field polarization. We have generated a wide variety of graphs to allow quick scattering-loss estimates without handling of the derived mathematical equations. We have identified radiation trends and suggested waveguide cross-sections less sensitive to scattering losses. To our knowledge, this is the first scattering-loss analysis that explicitly considers how the radiation pattern is affected by the waveguide cross-section.

PART III

Dimensional Accuracy

Chapter 7 Pattern Fidelity .... p. 147

Chapter 8 Process Calibration: Absolute Dimensional Control .... p. 153

Chapter 9 Frequency Matching: Relative Dimensional Control .... p. 159

In Part III, dimensional accuracy, the second main challenge in fabrication of high-index-contrast microphotonic devices, is addressed. First, the scanning-electron-beam lithography (SEBL) writing strategy is optimized to achieve appropriately smooth curves. Then, absolute and relative dimensional controls are tackled. A process calibration method providing an absolute dimensional control of 5 nm is presented. Dimensional variations in microring filters resulting from e-beam proximity effects are calculated. Dimensional disparities between microrings are compensated by offsetting the corresponding SEBL exposure dose. Microring resonators with average ring-waveguide widths matched to 26 pm to a desired relative width-offset are reported.

Chapter 7

Pattern Fidelity

7.1 INTRODUCTION

The first concern in dimensional accuracy is pattern fidelity. That is, the correctness of the overall shapes. In many circumstances, one may obtain locally an appropriate dimensional control but globally an incorrect shape. Shape control is central for large scale dimensional control, waveguide smoothness, and waveguide-curvature control. Mistakes in waveguide curvature or smoothness may generate significant propagation loss.

7.2 SEBL WRITING STRATEGY

Scanning electron-beam lithography (SEBL) systems are often designed with exposure of rectangular elements in mind (Manhattan geometry). When fabricating the smooth curves required in microphotonic applications, special attention must be given to the e-beam scanning strategy. In many vector-scan systems, a line is exposed by first deflecting the e-beam to a position at a given distance from one of the desired edges of the line to be exposed. Then, the e-beam is continuously scanned toward the edge of the line of interest. The e-beam is turned on (blanker deactivated) at the time the scanning is

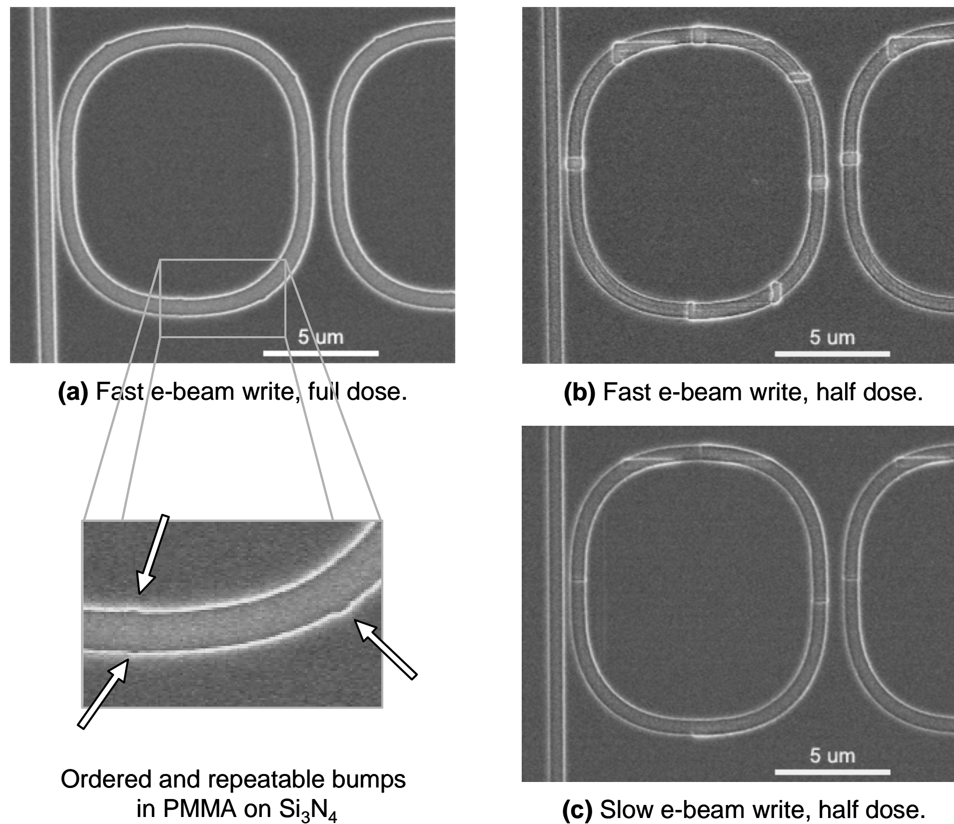

Fig. 7.1 Electron micrographs demonstrating e-beam deflection errors introduced by the Raith 150. Racetrack resonators were written in PMMA on Si_3N_4. (a) A fast write speed generates 50-to-100-nm-bumps on the racetracks. (b) The low-dose exposure shows that the bumps are mainly due to double-exposed resist (c) A slow write speed reduces the deflection errors.

expected to have reached the desired start of the line and turned off (blanker re-activated) at the time the scanning is expected to have reached the desired end of the line. Any error in the expected position of the e-beam in time during scanning will result in turning the beam on and off at the wrong moment and will affect the position and the length of the line. These errors are particularly important in low end systems like the Raith 150.

Electron micrographs demonstrating the deflection problems are presented in Fig. 7.1. Racetrack resonators were exposed at two different speeds. The slower write shows smaller writing errors. The errors are better seen when the SEBL dose used is

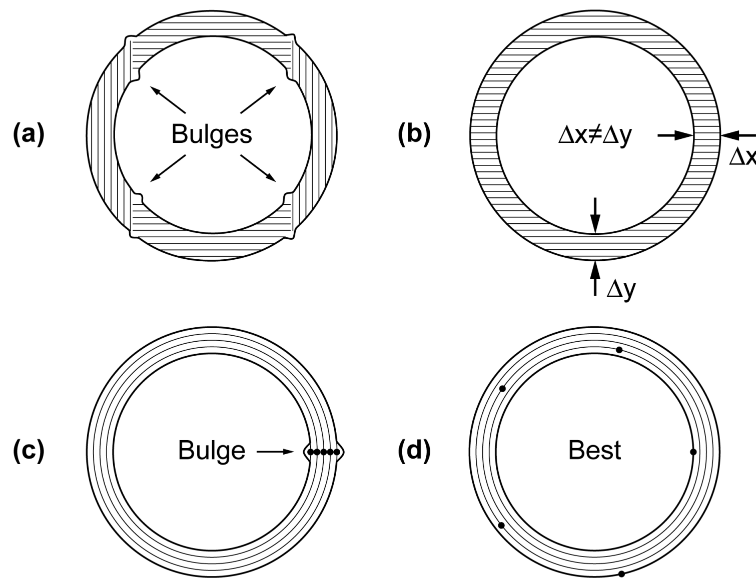

Fig. 7.2 E-beam vector-scanning strategies for microrings and observed problems in practice. (a) Default writing strategy in many vector-scan e-beam lithography systems. Bulges appear at the intersections between vertically and horizontally scanned lines. (b) Scanning the e-beam in only one axis removes the bulges but affects the width uniformity of the microrings. (c) Defining the microring with circular single pixel lines offers the best results but a bulge may appear near the starting/stopping point of the circular lines. (d) Angularly distributing the starting/stopping points removes the bulge.

small so double-exposed regions become clearly visible. We conducted a tedious experiment to re-calibrate the parameters used by the Raith 150 to compensate for deflection errors. However, the statistical confidence intervals on the parameters obtained were too large to warrant a clear improvement of the features. Therefore, we turned towards slow writing speeds and optimization of the e-beam movement to make deflection errors minor. The writing speed can be slowed down by using a small e-beam aperture, which reduces the e-beam current.

Fig. 7.2 shows four scanning strategies and the observed problems in practice. The scanning strategy can be controlled in most SEBLs by laying out the pattern with single-pixel lines. For best results, the pattern should be defined with circular single-pixel lines. As the SEBL makes errors at the connecting point where the line is started and ended, the

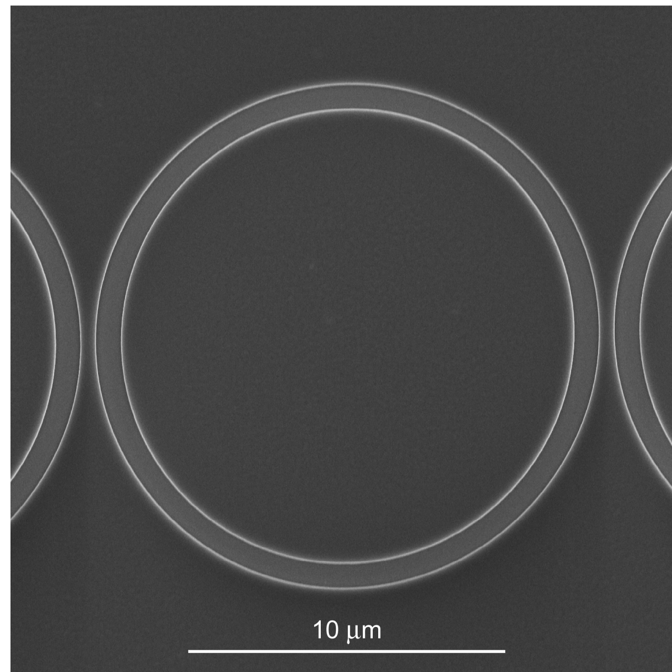

Fig. 7.3 Micrograph of a lithographically perfect microring exposed in PMMA on SiN with a Raith 150 using the writing strategy presented in Fig. 7.2d.

starting points of the single-pixel lines should be angularly distributed to avoid formation of a bulge. A smooth microring exposed in PMMA with the optimized writing strategy of Fig. 7.2d is shown in Fig. 7.3.

The geometry of the ring can also be affected by e-beam proximity effects as addressed in Chapters 8 and 9. To keep the ring smooth, standard proximity correction algorithms should be avoided as they divide the ring in small areas of different doses, which can stress the SEBL towards higher pattern inaccuracy. Instead, this problem is better addressed by exposing dummy structures to render the dose distribution more uniform. The impact of proximity effects on feature size is characterized below in Figs. 8.1, 9.4 and 9.8.

7.3 CONCLUSION

The SEBL writing strategy was addressed to achieve the required pattern fidelity. E-beam deflection problems were identified and resulting writing errors resolved. The scanning strategy presented in Fig. 7.2d should be applied whenever shape accuracy is critical. For instance, it was employed in the fabrication of bus-waveguides in the FSR-doubled filters presented in Sec. 3.5. The arcs forming the outer regions of the interferometric couplers were exposed with arced-single pixel lines with alternating angular direction of writing.

Chapter 8

Process Calibration:

Absolute Dimensional Control

8.1 INTRODUCTION

Absolute dimensional control is required in microphotonic filters to obtain an accurate filter bandwidth, filter shape, and absolute filter frequency. In this Chapter, a process calibration technique is presented. An absolute dimensional control of 5 nm is demonstrated. Such dimensional control is sufficient to achieve the needed correctness in filter shape and bandwidth. However, it represents a potential error of 100-200 GHz on the absolute filter frequency. This is more than an order of magnitude higher than what can be tolerated. Hence, post-fabrication trimming of the absolute filter frequency cannot be omitted. Nonetheless, with 5 nm absolute dimensional control and appropriate dimensional uniformity over an optical chip, this trimming can be performed simply by adjusting the global operational temperature of the optical chip.

8.2 PROCESS CALIBRATION

Strict dimensional control can be obtained by process calibration. Hence, it is limited by the repeatability of the fabrication process and the accuracy of the dimensional measurement technique used for calibration. The e-beam dose is chosen for optimal sidewall smoothness. Then, the critical dimensions are measured and the patterns are dimensionally biased in the SEBL layout to obtain the desired dimensions at device fabrication. To ensure consistent discretization of patterns, all dimensions must be chosen to be multiples of the SEBL step size. The dimensional repeatability of the fabrication process is enhanced when using a high-contrast resist and when measuring the e-beam current at regular intervals during long writes to ensure a uniform dose distribution across the wafer. The larger the chemical contrast of the resist is, the smaller the dimensional changes induced by SEBL dose, resist-developer strength, and development-time variations are. Similarly, high lithographic resolution enhances dimensional repeatability. For a given feature size, higher lithographic resolution will provide higher exposure-contrast (sharper dose profile). The higher the exposure contrast is, the smaller the dimensional changes induced by variations in the resist-clearing dose are. This is further investigated below and illustrated in Fig. 9.4. The clearing dose is defined as the minimum exposure dose required for the resist developer to dissolve the entire resist thickness in a given development time. Variations in resist clearing-dose can be due to variations in resist sensitivity (molecular-weight variations of PMMA), resist-developer strength, and resist development time.

Accurate dimensional measurements can be obtained by using the SEBL in scanning-electron-microscope (SEM) mode and calibrating the deflection of the e-beam to the movement of the interferometric stage. Such calibration can be accurate to 10^{-4} or better. Without it, usual dimensional measurement on standard SEMs can only be trusted

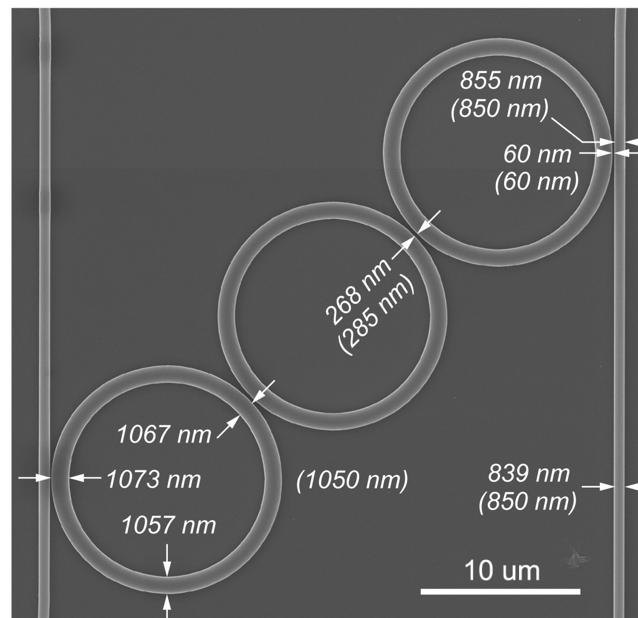

Fig. 8.1. Impact of e-beam proximity effects on absolute dimensional control. Ring-waveguide width variations are further investigated in Chapter 9. Measured and desired (in parenthesis) dimensions are presented. If proximity effects are not sufficiently corrected, the process calibration must focus on the most critical dimensions. When compared to resulting waveguide-widths, the ring-to-bus gaps are wider than expected. This is attributed to weak sidewall passivation in high-aspect-ratio trenches.

to within a 5% error. In our case, the measurement accuracy is limited by mechanical vibrations during data acquisition and sidewall roughness. The measurement error is of the order of 5 nm on micron-size features.

Optical resonators are much more sensitive to dimensional variations than the dimensional measurement accuracy. Some lithographic problems can only be observed through optical characterization of fabricated filters. For instance, as mentioned in Sec. 3.5, we have observed a repeatable frequency mismatch of ~ 20 GHz between microring resonators in second-order filters. A similar problem was observed in fourth-order filters but not in third-order filters. We expect this to be an error in the digital-to-analog converter of the Raith 150 resulting in a wrong spacing between two or more horizontal lines of pixels near the middle of the write field.

8.3 RESULTING DIMENSIONAL CONTROL

The fabrication process was calibrated to provide a correct bus-to-ring coupling coefficient, which required an accurate coupling gap, bus-waveguide width, and ring-waveguide width in the bus-to-ring coupling regions. Dimensional measurements for the first frequency-matched filters and multistage filters are presented in Table 8.1. Strict dimensional control is demonstrated to within the measurement error (~ 6-8 nm for these measurement, can be as low as 5 nm for straight isolated waveguides). As e-beam proximity correction algorithms were not applied, dimensional inaccuracies reaching 15 nm were observed on less critical parts of the structures. The impact of e-beam proximity effects on feature size in the first third-order filters is shown in Fig. 8.1. There, dimensional variations reached 20 nm. The impact of proximity effects on the microring shape of the first frequency-matched and the multistage filters is investigated in Sec. 9.4 and 9.5.

To save time and meet internal deadlines, the process calibration for all filters but the polarization-independent ones was performed by measuring the dimensions of the Ni

TABLE 8.1
PROCESS CALIBRATION PERFORMANCE

Parameter	First Frequency-Matched Filters		Multistage Filters	
	Measured dimension	Dimensional error	Measured dimension	Dimensional error
w_{bus}	804 nm	0 nm	704 nm	+2 nm
w_{ring}	802 nm	-2 nm	899 nm	-1 nm
d_1	103 nm	+1 nm	124 nm	+4 nm

The bus and ring waveguide widths were calibrated and measured at the bus-to-ring coupling region. Dimensions are reported at mid-waveguide height for the first frequency –matched filters and at the waveguide-top for multistage filters. The measurement error is about 6-8 nm.

hardmask and not of the etched waveguides. This approach was found effective as the hardmask dimensions were indistinguishable from the waveguide dimensions until the RIE process was re-optimized to improve sidewall smoothness (just before fabrication of multistage filters). The power was reduced from 400 to 300 W and the bias was increased from 250 to 500 V. This reduced sample heating while keeping the Ni-to-SiN etching-selectivity mostly unchanged. The resulting RIE process provided more slanted sidewalls (~ 86 degrees) and the hardmask dimensions corresponded to dimensions at the top of the etched waveguides in the multistage filters and not at the mid-height of the waveguides. Therefore, in order to express the performance of the dimensional calibration itself, the dimensional measurements in Table 8.1 are reported at mid waveguide-height for the first frequency-matched filters and at waveguide-top for the multistage filters. The latter waveguides were about 26 nm larger at the mid-height than at the top when isolated. In the high-aspect-ratio bus-to-ring coupling gap, the sidewalls were more vertical and the coupling gap was reduced at mid-height by about 16 nm. This is attributed to weak sidewall polymerization in high-aspect-ratio trenches.

8.4 CONCLUSION

A process calibration technique yielding an absolute dimensional control of 5 nm was presented. In research laboratories, where process repeatability can be an issue, a calibration must be performed before each device fabrication to compensate for processes drifting in time. Special attention must be given to drifting of the resist clearing dose and the RIE parameters. The PMMA molecular weight varies from batch to batch changing the clearing dose. Moreover, the flow controllers regulating the gas ratios in the RIE may drift out of calibration and affect the sidewall polymerization during etching and, in turn, the waveguide dimensions.

Chapter 9

Frequency Matching: Relative Dimensional Control

9.1 INTRODUCTION

Strict relative dimensional control is required in high-index-contrast microphotonic filters to limit ripple and dispersion, and to achieve sufficient in-band extinction. The resonant frequencies of coupled dielectric resonators must be matched to 1/20 of the filter bandwidth for best filter performance. For 40 GHz filters, it means the resonance frequencies of adjacent resonators must be matched to 10^{-5}. For microring resonators, this represents a relative dimensional control on the average ring-waveguide widths of at least 0.1 nm. In this Chapter, we develop techniques to achieve the required relative resonant frequency control. The roots of resonant frequency shifts are investigated. The effect of the scanning-electron-beam lithography (SEBL) exposure dose is thoroughly analyzed via simulations and experiments. Microring resonators with average ring-waveguide widths matched to 26 pm to a desired relative width-offset are reported (frequency matched to better than 1 GHz).

9.2 FREQUENCY MATCHING STRATEGY

Frequency mismatch between microring resonators can be due to coupling-induced frequency shifts (CIFS) [15], e-beam proximity effects, SEBL discretization errors, SEBL intra-field distortions, and SEBL digital-to-analog-converter errors.

As optical and imprint lithography masks are usually made by SEBL, all of the above mechanisms are expected to introduce frequency shifts even if the microrings are fabricated using optical or imprint lithography instead of SEBL. However, when optical projection lithography is used, the dimensional errors on the mask will be reduced by the demagnification factor of the projection system (usually 4 or 5X). Proximity-correction algorithms are typically applied in mask manufacturing. However, even if they help reduce frequency shifts due to e-beam proximity effects, they cannot eliminate these shifts as they correct the electron-beam dose distribution to first order only [58], which is insufficient for frequency matching.

The SEBL discretization errors can be eliminated by choosing all device dimensions

Fig. 9.1 Frequency matching strategies. (a) The SEBL dose of the middle ring is increased to precisely widen the middle-ring waveguide. (b) A secondary non-resonant ring is introduced at the center of the middle ring to increase the effective index of the middle ring-waveguide. Both methods lower the resonant frequency of the middle ring to match it to the outer rings. (a) is particularly useful if a maskless lithography technique such as SEBL is used and can be applied in either mask manufacturing or direct device writing. (b) is particularly useful for photolithography or nano-imprint lithography when little control is exerted on the mask manufacturing process.

to be multiples of the SEBL step size. All the remaining repeatable frequency shift sources can be compensated by properly adjusting the middle-microring resonant-frequency. The dimensional alteration required for such a correction is much smaller than the SEBL step size and cannot be obtained by changing the middle ring dimensions in the SEBL layout. However, such a small, precise, and accurate dimensional alteration can be introduced by changing the e-beam dose of the middle microring. By increasing the middle-ring dose, the width of the ring waveguide is increased slightly and the middle-ring resonance-frequency can be lowered to match it to the outer microrings. This dose-compensation can be introduced when using direct-write SEBL or when fabricating a lithographic mask for optical or imprint lithography.

When optical or imprint lithography is used and little control is exerted on the mask fabrication, the middle-microring resonant-frequency can be adjusted by changing the effective index of the ring waveguide without attempting to precisely correct its dimensions. A secondary non-resonant ring can be introduced in the center of the middle microring to increase its effective index and lower its resonance frequency to match it to the outer rings.

The two frequency correction approaches are illustrated in Fig. 9.1. In the present work, only e-beam dose-compensation was used.

9.3 PROXIMITY FUNCTION

The exact e-beam dose-compensation required for frequency matching of the microrings is best found empirically by fabricating and optically characterizing a number of filters with various dose-compensations. However, to reduce the number of empirical iterations needed and better understand the underlying physical phenomena, the e-beam proximity function is desired. It allows us to estimate the frequency mismatch due to the e-beam

proximity effects and the dose-compensation needed for frequency matching. These two quantities cannot be usefully estimated from dimensional measurements, which lack the required accuracy.

The proximity function was found empirically using two different methods. First, large rings (Fig. 9.2a) were exposed with various inner radii and e-beam doses [59]. The rings were inspected with an SEM and the minimum ring-dose required to fully develop the resist in the middle of a ring with a given inner radius was noted. Second, isolated dots (Fig. 9.2b) were exposed with various e-beam doses and their radii measured with an SEM [60]. All exposures were performed on the multilayer of interest (Fig. 3.2a) with a Raith 150 SEBL operating at 30 KeV. The PMMA was developed with 3:1 IPA:MIBK, a higher-contrast developer than the one used for microring fabrication, as resist contrast was more important for this application than line-edge smoothness. The samples were coated with a thin (2-3 nm) layer of Au-Pd to prevent charging during the SEM analysis.

The proximity function $f(r)$ is a monotonically decreasing function normalized so

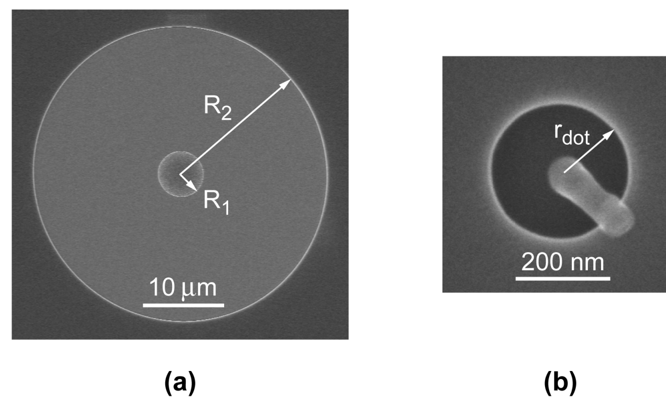

Fig. 9.2 Two empirical method used to obtain the e-beam proximity function. (a) Large rings were exposed with various inner radii and doses. The lowest ring-dose clearing the center of the ring was noted. (b) Dots were exposed with various doses and their radii measured. The pole in the middle of the dot (fallen on its side) is characteristic of PMMA exposed at high doses where it becomes highly cross-linked and insoluble to the resist developer.

$$\int_0^\infty f(r)2\pi r dr = 1 \tag{9.1}$$

where r is the distance from the center of the e-beam to the point of interest. Most often, it is assumed to follow a double-Gaussian model [61]

$$f_0(r) = \frac{1}{\pi(1+\eta)}\left(\frac{1}{\alpha^2}\exp\left(\frac{-r^2}{\alpha^2}\right) + \frac{\eta}{\beta^2}\exp\left(\frac{-r^2}{\beta^2}\right)\right), \tag{9.2}$$

where $\alpha < \beta$ and where the first Gaussian accounts for forward electron-scattering and the second Gaussian accounts for backward electron-scattering.

The experimental results obtained with the large rings are presented in Fig. 9.3a. The required ring exposure dose D to reach, at the center of the ring, the resist clearing dose D_0 is given by

$$\begin{aligned} D &= \frac{D_0}{\int_{R_1}^{R_2} f(r)\,2\pi r dr} \\ &\simeq \frac{D_0}{\int_{R_1}^{\infty} f(r)\,2\pi r dr}\ ,\ R_2 > 3\beta\ , \end{aligned} \tag{9.3}$$

where R_1 and R_2 are the inner and outer ring-radii, respectively. Most often, R_2 is chosen to be large enough for the upper limit of the integration to be approximated by infinity. $R_2 = 18\ \mu m$ was used in the present experiments.

The experimental results obtained with the dots are presented in Fig. 9.3b. The dot dose d_{dot} and the dot radius r_{dot} are related to the proximity function by

$$f(r_{dot}) = \frac{D_0}{d_{dot}}\left(10^{-8}\,\tfrac{cm^2}{\mu m^2}\right), \tag{9.4}$$

where r_{dot} is expressed in μm, $f(r)$ is expressed in μm^{-2}, D_0 is expressed in $\mu C/cm^2$, and d_{dot} is expressed in μC.

Exposing large rings was found to be particularly useful for probing the proximity function at long interaction lengths (R_1 > 1um). For small R_1, identifying the needed ring-dose accurately is difficult as a particle can be mistaken for remaining resist. On the other hand, exposing dots was found particularly useful for short to medium interaction lengths (40 nm < r_{dot} < 1 um). For longer interactions, the exposure contrast becomes too low at the clearing dose for the edge of the PMMA dots to be well defined (an even higher contrast resist would be required). Below 40 nm, the measurements are also difficult as the feature size gets close to the resist resolution and the shape of the dots is affected by imperfect stigmation of the e-beam.

The experimental data was least-square fit to the double-Gaussian model of (9.2). The best fit is shown with dotted lines in Fig. 9.3. The fitted parameters are presented in Table 9.1. As $f(r)$ could not be probed at sufficiently short interaction lengths, $\alpha = 0.015\mu m$ was assumed from simulation data provided by the SEBL manufacturer. The resulting fit looks acceptable in Fig. 9.3a but, in Fig. 9.3b, where the discrepancy is amplified by the logarithmic scale, the double-Gaussian model looks obviously inappropriate. A similar tail in the proximity function has been reported in [60] where it was found to be possibly due to scattering in the resist, high energy secondary electrons, and tails in the incident e-beam distribution. In addition, the proximity function was simulated in [62] for the multilayer and e-beam energy of interest and a similar tail was observed.

The double-Gaussian model can be corrected by adding a tail function $\tau(r)$. Then, the proximity function becomes

$$f_1(r) = \frac{f_0(r) + \tau(r)}{1 + \int_0^\infty \tau(r) 2\pi r dr}. \tag{9.5}$$

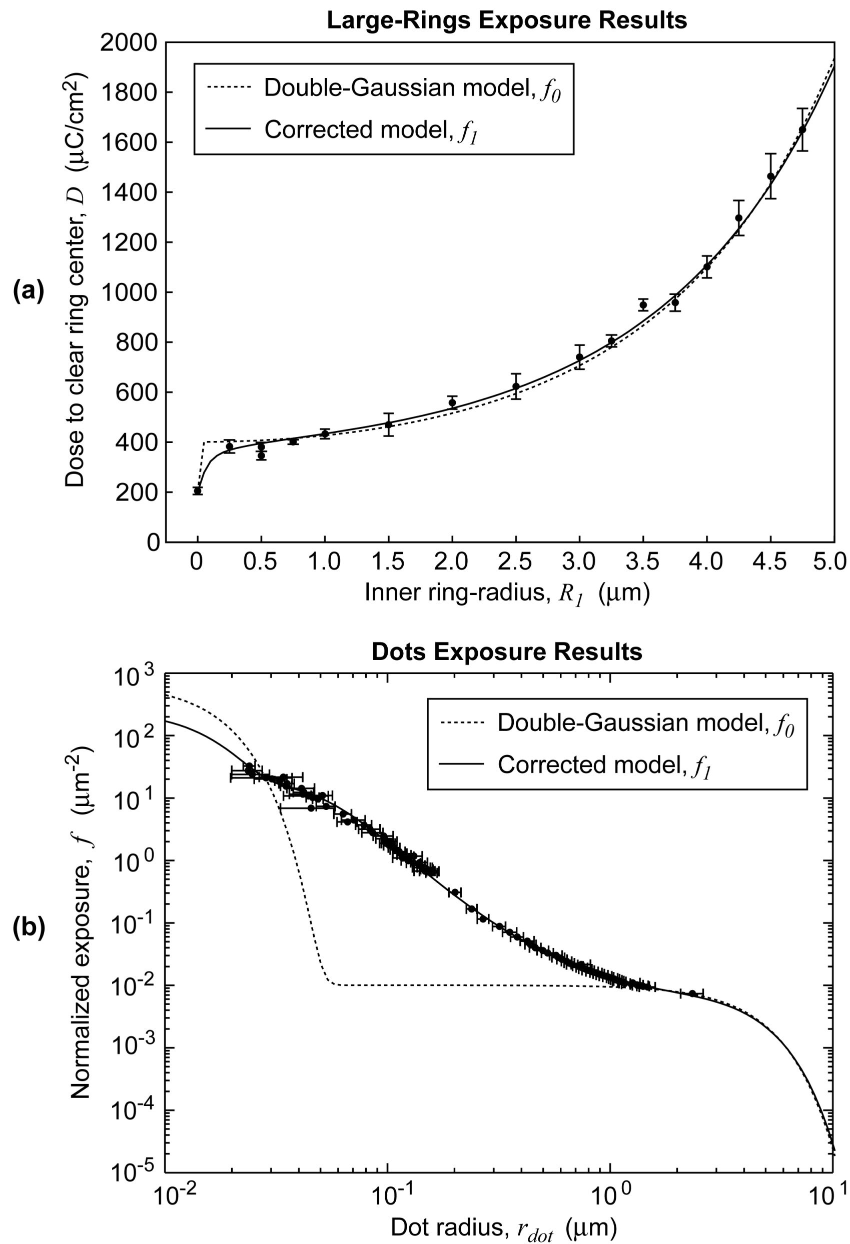

Fig. 9.3 Experimentally obtained e-beam proximity function. (a) Results obtained with large ring exposures. (b) Results obtained with dot exposures. The standard double-Gaussian model of the e-beam proximity function is not appropriate as seen in (b). The model was corrected with a tail function presented in (9.6). The fitted parameters are reported in Table 9.1.

Form Fig. 9.3b, we see that the tail could be fit to a polynomial in logarithmic space. In fact, a simple exponential is not sufficient. Hence, we choose the tail function to be of the form

$$\tau(r) = \exp\begin{pmatrix} t_4\left(\ln(r)\right)^4 + t_3\left(\ln(r)\right)^3 \\ + t_2\left(\ln(r)\right)^2 + t_1\left(\ln(r)\right) + t_0 \end{pmatrix}, \tag{9.6}$$

where t_4, t_3, t_2, t_1, and t_0 are the fitting parameters. The best fit to this corrected double-Gaussian model is shown with the solid lines on Fig. 9.3. The fitted parameters are reported in Table 9.1.

9.4 FAST PROXIMITY EFFECTS COMPUTATION

To define arbitrary structures, the SEBL exposes sets of discreet points (pixels). The dose at a given location $D(x, y)$ will be given by the summation of the contributions of all exposed points weighted by the proximity function

$$D(x, y) = \sum_i q_i f_1(\sqrt{(x - x_i)^2 + (y - y_i)^2}) \ , \tag{9.7}$$

where x and y define the location at which the dose is sought, x_i and y_i define the position of an exposed point, and q_i is the dose delivered at that point. When the SEBL step-size is smaller than the proximity function parameter α, (9.7) is well approximated by a two-dimensional (2D) convolution

$$\begin{aligned} D(x, y) &= Q \otimes \otimes f_1 \\ &= \int_{-\infty}^{+\infty}\int_{-\infty}^{+\infty} Q(x', y') f_1(\sqrt{(x - x')^2 + (y - y')^2})\, dx'\, dy' , \end{aligned} \tag{9.8}$$

where Q is the dose profile laid out in the SEBL. For arbitrary patterns, the 2D convolution needs to be computed numerically. However, even with the best algorithms,

a numerical 2D convolution requires a large number of operations and is not well suited for computation of small dimensional changes in large structures like microring resonators. For microring filters, the following semi-analytical method can greatly simplify the computational problem. It takes advantage of the fact that microring filters are formed of one-dimensional (1D) elements. Microrings are 1D elements in cylindrical coordinates and infinitely-long straight-bus-waveguides are 1D elements in Cartesian coordinates. Bus waveguides can be assumed infinitely long and straight if they extend straight to more than $3\beta\,(\sim 12\mu m)$ above and below *y*. Then, the dose profile resulting from exposing with unit dose a bus waveguide centered at the origin is given by

$$F_{bus}(x) = \int_{-w_{bus}/2}^{+w_{bus}/2} f(x - x')\,dx' , \tag{9.9}$$

and the dose profile resulting from exposing with unit dose a microring centered at the origin is given by

TABLE 9.1
E-BEAM PROXIMITY FUNCTION FITTED PARAMETERS

Parameter	Double-Gaussian model $f_0(r)$	Corrected model $f_1(r)$
β	3.99 µm	4.08 µm
η	1.02	2.52
t_0		-4.935
t_1		-2.734
t_2		-0.786
t_3		-0.565
t_4		-0.108

$\alpha = 0.015\mu m$ was assumed from simulation data provided by the SEBL manufacturer. t_4, t_3, t_2, t_1, and t_0 are provided for r expressed in µm. The 95% confidence interval on β and η is respectively ±0.1 µm and ±0.1. Parameters are provided with a sufficient number of digits to accurately reproduce Fig. 9.3.

$$F_{ring}(r) = \int_{R-w_{ring}}^{R} \int_{0}^{2\pi} f(\sqrt{r'^2 + r^2 - 2r'r\cos\theta})\, r'dr' \,. \tag{9.10}$$

The above form of convolution in cylindrical coordinates is valid when the convolved functions are angularly invariant [63]. The complete dose-profile is now given by

$$\begin{aligned} D(x,y) = &\sum_j Q_j\, F_{bus}(x - x_j) \\ &+ \sum_k Q_k\, F_{ring}(\sqrt{(x-x_k)^2 + (y-y_k)^2})\,, \end{aligned} \tag{9.11}$$

where Q_j and Q_k are the area doses defined in the SEBL layout for each element (ring or bus waveguide), x_j defines the middle of each bus waveguide, and x_k and y_k define the center of each microring.

9.5 PREDICTED MICRORING SHAPES

Using the fast proximity-effects computation presented above, the dose profile was computed for the first frequency matched filters and the multistage filters. The shape of the microrings and all relative dimensions will follow approximately the contours of constant dose corresponding to the clearing dose of the resist. However, the absolute dimensions of the microrings will be consistently offset from these contours by the fabrication process.

The microring shape is a function of the SEBL area dose used. A given SEBL area dose (the minimum-proximity-effects dose or MPE dose) will minimize the width variations in all microrings. In the present case, it is obtained when the SEBL exposure dose used is about three times the clearing dose of the resist. In Figs 9.4 and 9.5, the clearing-dose contours are plotted for various SEBL doses expressed as relative offsets from the MPE dose. As expected, the ring waveguides are wider for higher e-beam doses. The largest ring-waveguide widths are obtained near the small bus-to-ring coupling gaps

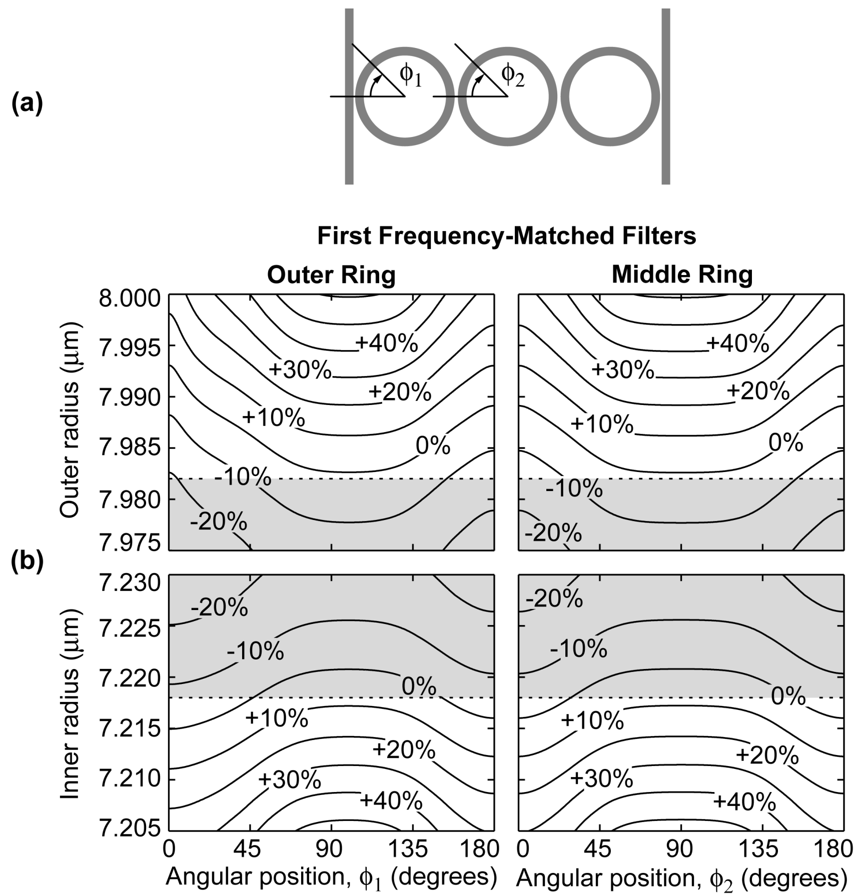

Fig. 9.4 Resist clearing-dose contours for various SEBL area-doses expressed as relative offsets from the dose minimizing the width variations in all ring-waveguides of a filter. The ring-waveguide edges will follow the clearing dose contours but will be consistently offset by the fabrication process. The dotted lines represent the positions of the ring-waveguide edges in the SEBL layout and take into account the width bias used in fabrication. The shaded areas correspond to the regions exposed by the SEBL. (a) Definition of angular positions along the outer and inner rings. (b) Clearing-dose contours for first frequency-matched filters.

while the smallest ring-waveguide widths are obtained near the top and bottom of the middle rings. The dose profile of each filter has two axes of symmetry (one vertical and one horizontal) going through the center of the middle ring of the filter.

When the same dose is used on middle and outer rings, the width of the middle ring is smaller than the width of the outer rings. Moreover, as the outer and inner radii are

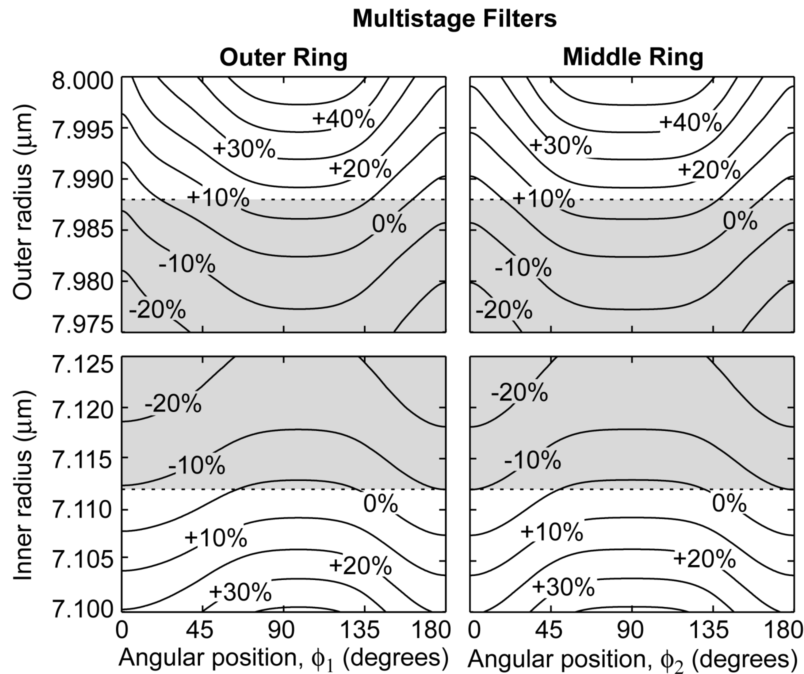

Fig. 9.5 Resist clearing-dose contours in multistage filters for various SEBL area-doses expressed as relative offsets from the dose minimizing the width variations in all ring-waveguides of a filter. The ring-waveguide edges will follow the clearing dose contours but will be consistently offset by the fabrication process. The dotted lines represent the positions of the ring-waveguide edges in the SEBL layout and take into account the width bias used in fabrication. The shaded areas correspond to the exposed regions by the SEBL. The angular positions are defined in Fig. 9.4a.

differently affected by proximity effects, the ring circumference is larger in the outer rings than in the middle ring. These raise the resonant frequency of the middle ring and create a frequency mismatch with the outer rings. This frequency mismatch will be a function of the SEBL area dose used as the shapes of the middle and outer rings are differently affected by a dose change. This dependence is presented in Fig. 9.6a. The smallest frequency mismatch is obtained near the MPE dose. When the SEBL dose used differs significantly from the MPE dose, the frequency mismatch increases sharply due to weaker dose-profile gradient near the resist clearing dose resulting in larger variations in

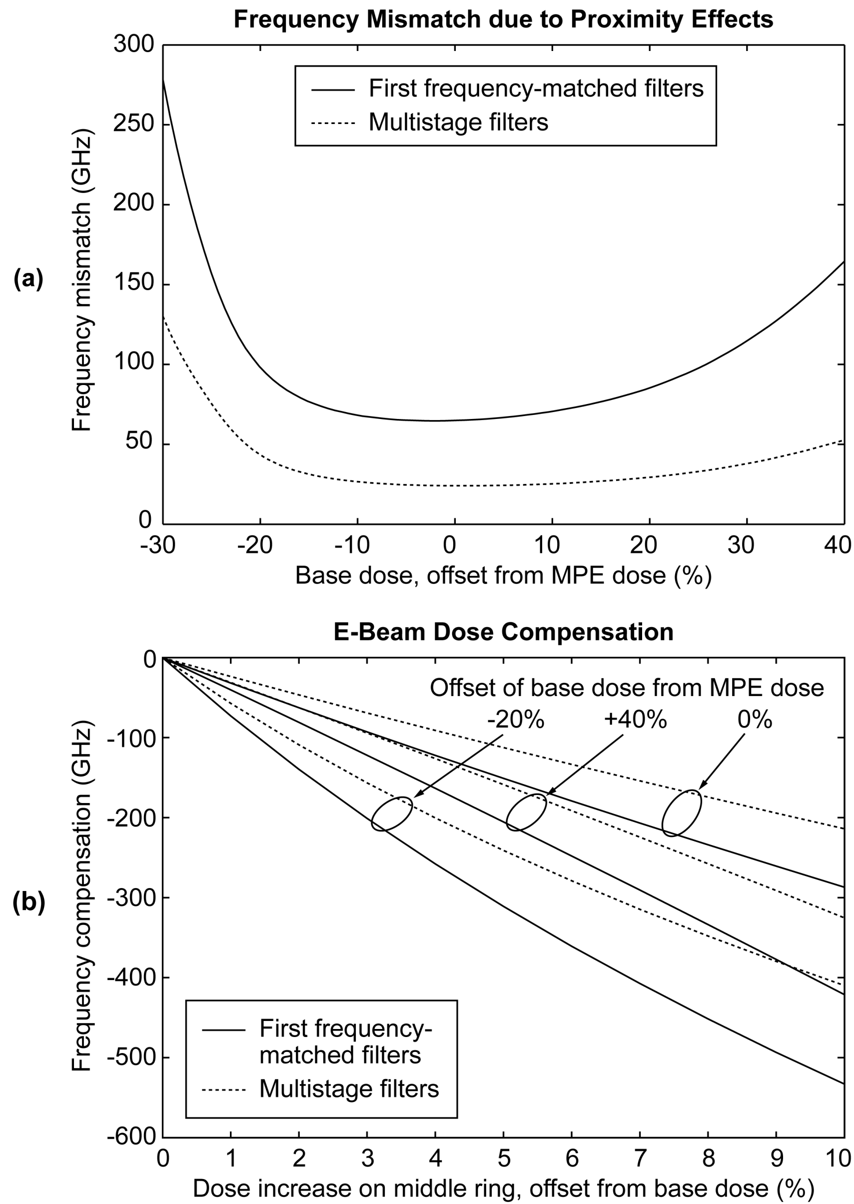

Fig. 9.6 (a) Predicted frequency mismatch between middle and outer microrings due to e-beam proximity effects. The minimum proximity effect (MPE) dose is defined as the SEBL dose minimizing the width variation in all ring-waveguides of a filter. (b) Predicted frequency compensation resulting from an increase of the SEBL dose on the middle ring. The base dose is the SEBL area dose used on all rings in (a) and on outer rings in (b).

the microring shapes. To correct for frequency mismatches due to proximity effects and all other repeatable sources, one can increase the dose on the middle ring to reduce its resonant frequency. The resulting frequency compensation is shown in Fig. 9.6b. Note that the exact shapes of the outer and middle rings do not need to be the same as only the resonant frequencies need to be equal. An estimate of the total frequency mismatch can be obtained by adding an estimate of the CIFS (usually obtained by FDTD) to the frequency mismatch due to proximity effects of Fig. 9.6a. Then, an estimate of the dose compensation required is obtained from Fig. 9.6b.

A dose increase on the middle ring will lower not only the resonant frequency of the middle ring but also, through proximity effects, the resonant frequency of the outer rings. This form of cross-talk is taken into account in Fig. 9.6b. For a given dose compensation, the decrease of the outer rings resonant frequency corresponds to 3.0-3.5% of the decrease of the middle ring resonant frequency.

To obtain repeatable frequency-matched filters, the ratio between the SEBL dose employed and the clearing dose of the resist must be controlled to a few percent. Moreover, the dose-compensation must be controlled to about 0.05%. These are very strict requirements. As the frequency mismatch mainly affects the in-band extinction, multistage filters can relax these fabrication tolerances by allowing over-designing of the in-band extinction. Such an over-design was employed in the polarization-independent filters presented in Chapter 3.

9.6 COMPARISON OF PREDICTED AND MEASURED DIMENSIONS

The width of fabricated microrings was measured in the first frequency-matched filters at diverse angular positions using the method described in Chapter 8. During fabrication, the SEBL area dose was chosen to minimize sidewall roughness. Predicted

microring shapes were obtained using an estimate of the clearing dose of the resist allowing us to choose the appropriate dose contours. The actual dose employed was found to be close to the MPE dose. Predicted and measured angular width variations are compared in Fig. 9.7. They agree within the measurement error and confirm the validity of our analysis. The worst agreement is observed near the bus-to-ring coupling gaps. It is believed to be mainly due to the behavior of RIE in small trenches, where sidewall passivation is reduced leading to wider gaps than expected. Another source of possible disagreement between predicted and measured width variations is the finite chemical-contrast of the resist. Resist edges would exactly follow the clearing-dose contours only if the resist exhibited infinite chemical-contrast. Obviously, this is not the case in practice. However, it is generally an acceptable approximation for high-contrast resists such as PMMA.

Error bars in Fig. 9.7 show that a useful estimate of the frequency mismatch cannot

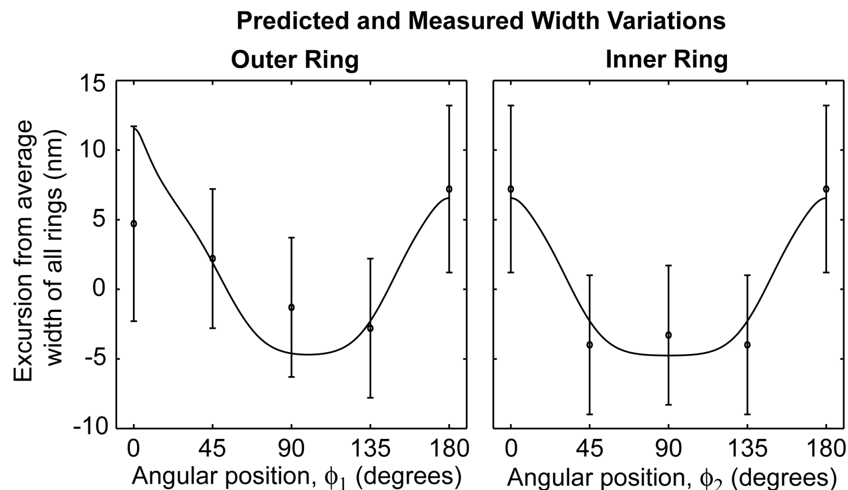

Fig. 9.7 Predicted and measured width variations in ring waveguides of first frequency-matched filters. The dimensional measurements were performed as explained in Chapter 8. The filter is assumed to have two axes of symmetry (one vertical and one horizontal) going through the center of the middle ring. The angular positions used are defined in Fig. 9.4a.

be obtained from dimensional measurements alone. For instance, in the first frequency-matched filters, a 5 nm measurement error on the ring-waveguide width corresponds to a 200 GHz error on the resonance frequency of the corresponding microring.

9.7 EXPERIMENTAL RESULTS

Frequency-matched filters reported in Chapter 3 were obtained by generating sets of filters with various middle ring dose-compensations distributed around the expected dose-compensation required. For the first frequency-matched filters, sets of 40 filters with a linear distribution of dose-compensation in 0.5% increments were fabricated. The best-compensated filter was reported in Fig. 3.6. For the multistage filters, sets of 30 one-, two-, and three-stage filters were fabricated. A non-linear distribution of dose compensation was used with the smallest dose-steps surrounding the expected dose-compensation required. Fig. 9.8 shows the empirical relationship between frequency-mismatch and dose-compensation for the first frequency-matched filters and the multistage filters. The experimental frequency-mismatch-points were obtained by fitting the measured spectral responses to a model of the filter. Parabolic trend lines were added. In the multistage filters, the frequency mismatches of the one-stage filters only were measured. The frequency mismatches of the two- and three-stage filters are expected to be the same as for the one-stage filters.

At small dose-compensation, the trend lines are consistent with the calculated frequency shift presented in Fig. 9.6b. The SEBL base-dose used in experiment was close to the MPE dose. Above 5% dose-compensation, the experimental trend lines level off and a discrepancy with the calculated trends arises.

Table 9.2 summarizes the calculated and observed frequency shifts as well as the required dose-compensations. Considering the complexity of the problem, excellent

agreement is seen between the calculated and experimentally observed parameters. The observed frequency mismatch is higher than the calculated one. This is probably due to phenomena that we were unable to estimate such as SEBL intra-field distortion, and SEBL digital-to-analog-converter errors. For the first frequency-matched filters, the

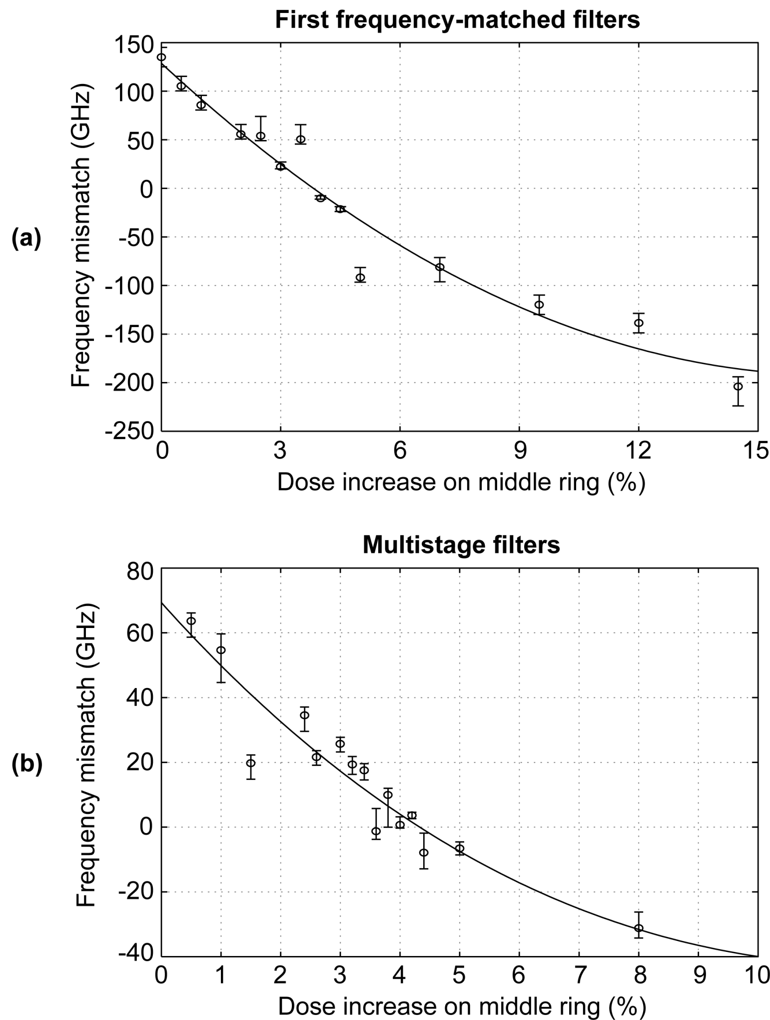

Fig. 9.8 Frequency mismatch observed in experiment at various dose-compensations for (a) first-frequency-matched filters and (b) multistage filters (frequency mismatch of the one-stage filters is reported). The data points were obtained by fitting the measured spectral responses to a model of the filter. An example of such fit is presented in Fig. 3.6b. The error bars represent estimated characterization and fitting errors. The trend lines are parabolic. [Data fitting by M.A. Popovic]

calculated dose-compensation required from Fig. 9.6b to compensate the experimentally observed frequency mismatch corresponds exactly to the dose-compensation experimentally needed. For the multistage filters, however, a discrepancy arises between the experimentally observed and the calculated dose-compensations required to compensate the experimentally observed mismatch. This error in the calculated dose compensation may be due to the leveling off of the frequency-mismatch trend observed in Fig. 9.8. This leveling is stronger in the multistage filters than in the first frequency-

TABLE 9.2
CALCULATED AND OBSERVED FREQUENCY MISMATCH

Parameter	First frequency-matched filters	Multistage filters
Calculated frequency-mismatch due to e-beam proximity effects	70 GHz	30 GHz
Calculated coupling-induced frequency-shift (CIFS)	38 GHz	22 GHz
Total calculated frequency-mismatch	108 GHz	52 GHz
Observed frequency-mismatch (from trend line)	130 GHz	70 GHz
Difference between observed and calculated mismatch	22 GHz	18 GHz
Calculated dose-compensation required	3.6 %	2.2 %
Calculated dose-compensation required for observed mismatch	4.3 %	3.0 %
Observed dose-compensation required	4 .0- 4.5%	4.2 - 4.4%
Smallest frequency mismatch obtained	< 1 GHz	< 2 GHz
Corresponding average ring-waveguide-width mismatch	< 26 pm	< 68 pm

matched filters. It is most probably caused by non-linear phenomena such as widening of the coupling gaps due to weak sidewall polymerization in high-aspect ratio trenches. In fact, the main differences in the fabrication process of the multistage filters with respect to the first frequency-matched filters are a higher exposure dose and an improved RIE process with stronger sidewall polymerization. The higher exposure dose should increase sensitivity to dose variations and is inconsistent with the leveling off. Thus, at first sight, the stronger leveling off should be related to the RIE step.

Stochastic frequency variations are a major concern as they result in device failure and may require use of expensive post-fabrication trimming to achieve an acceptable yield. Taking into account possible characterization and fitting errors, the standard deviation of the measured points from the trend line reaches 14 GHz for the first frequency-matched filters and 5 GHz for the multistage filter. The difference is attributed to a better controlled fabrication process at multistage filter fabrication. In addition, wider ring-waveguides in multistage filters reduce sensitivity to dimensional variations by 25%. Note that a standard deviation is not necessarily meaningful in the present case as the distribution of frequency variations does not appear to be normal (Gaussian). Rather, the variation would be better analyzed with a probability of device failure. Setting the failure threshold to be an offset from the trend of at least 4 GHz that cannot be explained by measurement and fitting errors, we obtain a failure rate of 29% for the first frequency-matched filters and 13% for the multistage filters. The resulting yield is low but manageable.

Relative frequency variations between resonators could be minimized by appropriate choice of resonator size. The resonators should be small enough so variations in resist clearing dose, material thickness, and material index of refraction are small. If the stochastic defect density is high, the resonators should be large enough so local defects

are averaged out. If the stochastic defect density is low, the resonators should be small to minimize the probability of a defect on a resonator and, in turn, of device failure. In the present case, however, the resonator size is mostly fixed by the required FSR of the filter and little flexibility in optimization is available.

Fig. 9.9 shows variations of the outer-rings resonant-frequency with filter position. Once again, the experimental points were obtained by fitting measured spectral responses to a model of the filter. The dose-compensation is monolithically increased with filter position. A small increase in resonant wavelength with position would be expected from the effect of the middle-ring dose-increase on the outer rings. This resonant wavelength

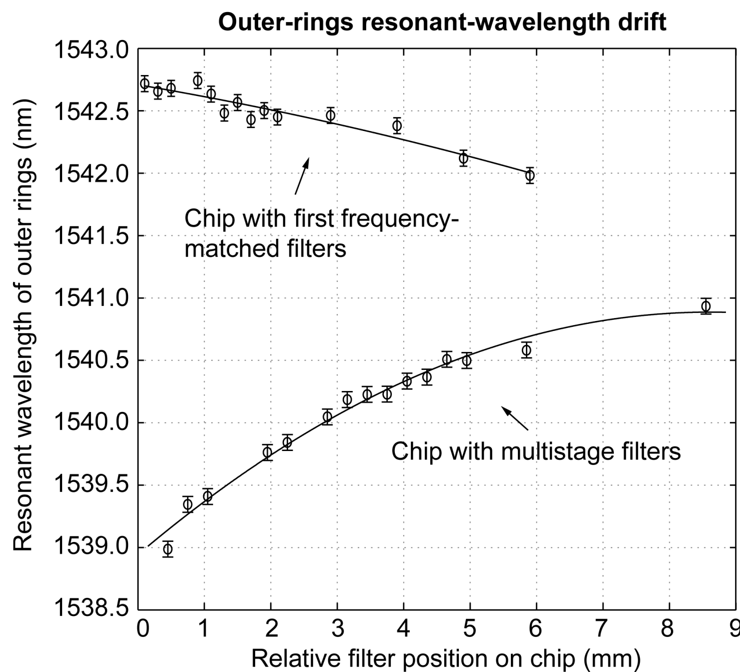

Fig. 9.9 Absolute resonant frequency of outer rings with relative filter position. The dose-compensation is monotonically increased with the filter position. The data points were obtained by fitting the measured spectral responses to a model of the filter. Parabolic trend lines are shown. The error bars represent estimated characterization and fitting errors. The frequency drift is most probably dominated by variations of the SiN thickness with position. The resonant wavelength decreases by about 0.5 nm for a 1-nm-decrease in SiN thickness [Data fitting by M.A. Popovic]

increase, however, should only be of about 0.1 nm for the first-frequency matched filters and 0.06 nm for the multistage filters. Hence, it cannot explain the observed drifts, which are on the order of a nanometer. The smoothness of the frequency trends indicates that frequency variations are not dominated by local defects. Hence, it could be compensated with appropriate calibration. Moreover, a discontinuous trend would be expected if the SEBL current drift was dominating the frequency variations as the SEBL dose was recalibrated at multiple points during the SEBL writing of the chips. This is not observed in experiment. Thus, the frequency drift is most probably dominated by variation of the SiN thickness with position. A 1-nm-decrease in SiN thickness would result in a 0.5-nm-drop of the resonant wavelength. The thickness variations could also explain the difference between the drifts observed in the two filter sets. The optical chip with the multistage filters investigated was closer to the wafer edge, where the SiN thickness variations are amplified, than the optical chip with the first frequency-matched filters. Moreover, the gas pressure during the low-pressure chemical-vapor deposition of SiN was higher at fabrication of the multistage filters than at fabrication of the first frequency-matched filters. A higher deposition pressure corresponds to worse thickness uniformity.

9.8 CONCLUSION

The relative dimensional control required for frequency matching of resonators was addressed. The sources of frequency shifts in microphotonic filters were investigated. Special attention was given to frequency shifts due to e-beam proximity effects and the impact of the SEBL exposure dose. Frequency mismatches were compensated with careful adjustments of the e-beam dose profiles. The required dose-compensations were estimate via simulations and compared to the experimentally needed dose-compensations. Considering the complexity of the problem, excellent agreement was observed. Microring

resonators frequency matched to better than 1 GHz were reported. This required their average ring-waveguide widths to be matched to 26 pm to a desired relative width-offset.

Chapter 10

Conclusions

10.1 SUMMARY OF ACCOMPLISHMENTS

Accurate nanofabrication techniques for high-index-contrast (HIC) microphotonic devices were developed and analyzed. The work addressed the two main challenges in fabricating high-index-contrast microphotonic devices: sidewall roughness and dimensional accuracy.

The most advanced microring add-drop filters ever reported in the literature were fabricated. Low 2.5 dB drop-loss, high >30 dB in-band extinction, high 40.8 nm free-spectral-range (FSR), filter bandwidth accurate to 5%, and polarization independent operation were demonstrated.

A sidewall roughness characterization and optimization technique was developed. The first three-dimensional analysis of scattering losses due to sidewall roughness in rectangular dielectric waveguides was derived. It offered new insight into the scattering mechanism and allowed prediction of the field polarization and the waveguide cross-sections that minimize scattering losses. The combination of these techniques enabled better understanding of the source of propagation loss in microphotonic waveguides and

improved estimation of the optical-loss induced by the contribution to roughness of individual process steps.

Strict dimensional accuracy was demonstrated. The scanning-electron-beam-lithography writing strategy was optimized to achieve the smooth features required by microphotonic devices. A process calibration technique was developed and an absolute dimensional accuracy of 5 nm demonstrated. Strict relative dimensional accuracy was achieved by careful control of the e-beam dose. The e-beam dose-profile was calculated and the dose variations required to obtain the needed precise dimensional offsets predicted. Microring resonators with average ring-waveguide widths matched to 26 pm to a desired relative width-offset were achieved.

The nanofabrication techniques developed in this work are significant for all HIC microphotonic devices: from microring resonators to photonic-bandgap structures.

10.2 FUTURE WORK

The main problem in the fabricated microphotonic devices is the high SiN material loss of 10 dB/cm. It was identified too late to be addressed in the present work and needs to be tackled in future work. From an optical-filter point of view, filter switching and tuning need to be explored. Finally, to allow HIC microphotonic devices to be widely employed in real world applications, the repeatability of resonant-frequency-control needs to be investigated.

Better understanding the source of the material loss in SiN would be a first step toward improving propagation loss. However, for practical reasons, it is unlikely that material loss in SiN could be radically improved even if the loss mechanism is well understood and found to be correctable. To do so, a dedicated reactor would be required to allow the needed deposition parameters flexibility, which cannot be provided by the

staff-operated shared-reactor presently used. More importantly, SiN is not fundamentally better than other materials potentially available for microphotonics. It was chosen for its availability at MIT and its interesting refractive index. Hence, switching to a material known to have low material loss may be an easier fix and a better allocation of resources. Three candidates come to mind: stoichiometric nitride (Si_3N_4), chalcogenide glasses (As-Se material system among others), and single-crystal silicon.

Stoichiometric nitride offers an index of refraction of about 2.0 and a material loss well below 1 dB/cm. The main problem with Si_3N_4 is its high stress after deposition not allowing the film thickness to exceed ~300 nm before the material cracks. The lower refractive index and the smaller achievable film thickness result in a reduced FSR when compared to SiN. Moreover, fabrication of polarization splitters and rotators would be problematical as they require thick films.

Select chalcogenide glasses offer low material loss and an index of refraction ranging from 2.4 to 2.8 [64, 65]. The main difficulty with these materials is their instability when compared to silicon and silicon nitride. Moreover, these materials are considered exotic for fabrication purposes so the deposition tools are not widely available and contamination concerns may be an issue.

Single-crystal silicon offers an index of refraction around 3.5 and negligible material losses when electronic doping is kept low. One of the main issues with single-crystal Si is that it cannot be directly deposited. Special wafer manufacturing is required to obtain the silicon-on-insulator wafers (SOI) needed for microphotonic devices. Furthermore, the high-refractive-index introduces unparalleled lithographic dimensional control requirements and stochastic resonant frequency variations would likely be a major issue. The main advantage of Si, is its high (10^{-4} K^{-1}) thermo-optical coefficient allowing thermal tuning of microring resonance over 15-20 nm. With appropriate design, this

tuning range is sufficient to create an add-drop filter that is thermally switchable and tunable over the entire C-band.

Whichever material is chosen, however, it is important to limit the complexity of the devices to be fabricated, otherwise the yield of research facilities would be a major obstacle. Research facilities excel in providing flexibility but not repeatability. A natural evolution of a research project is to tend towards increasing device complexity. However, one should aim the research toward demonstration of the most challenging key elements of a system and leave the large scale integration to industry, which excels in such tasks. Integration of components should be addressed within an academic laboratory if it represents a significant intellectual challenge (if a fundamental problem due to integration needs to be addressed). The complexity of the polarization independent filters reported in Chapter 3 should be seen as an upper boundary for device complexity.

Appendix A

RAITH 150

A.1 GENERAL OPERATION

A.1.1 Introduction

The Raith 150 is an entry-level scanning electron-beam lithography system (SEBL) widely used in academic laboratories. The system was designed for minimal cost and not maximum performance. This creates problems for the user that will be overviewed in this section. The main issues are related to:

- the e-beam column not being designed for lithography,
- the usable writing speed being much smaller than reported,
- the stage drift,
- the limited stage leveling range, and
- the numerous software and hardware bugs.

These will now be addressed. Then, an approach to multilayer exposures will be presented. The goal of this section is to provide technical insight that will be particularly useful for current and future Raith 150 users. This chapter assumes that the reader is familiar with the tool. Most of the problems discussed are not documented by Raith.

A.1.2 Column-Related Problems

The Raith 150 uses a LEO Gemini column designed for scanning-electron-beam microscopy (SEM). The column offers almost continuously adjustable e-beam energy from a fraction of a KeV to 30 KeV. For lithography, the low e-beam energies are of limited practical interest. Lithographic resolution, depth of focus, and dimensional variations due to proximity effects are improved at high electron energies. The only advantage to using low electron energies is that the in-lens secondary-electron detector can be used. This detector offers excellent signal-to-noise ratio making the parameter adjustments (focus, stigmation and aperture alignment) less problematic. Above ~17 KeV, the in-chamber secondary-electron detector must be used. It offers much worse signal-to-noise ratio than the in-lens detector and can make parameter adjustment difficult. For high electron energies, a backscattered-electron detector would be needed but is lacking in the system. In this work, all patterns were exposed at 30 KeV. However, 10 KeV was used for stage leveling as will be discussed below. Most commercial SEBL systems operate at 50 to 100 KeV.

One of the main limitations induced by the Gemini column is the usable field size, which is limited to 100 μm for the usual ~6 mm working distance. The field size can be increased up to ~150 μm if the working distance is increased to a large ~ 9 mm. In most cases, stitching errors cannot be tolerated within a device. Hence, the maximum field size limits the maximum device size one can create. The field size limitation is due to a noisy deflection amplifier used by the Gemini column at low magnification. For microscopy, low magnification is used solely to find the features to be inspected and a good amplifier is not required. For lithography, it is critical that the "mag range" of the system be 2 or 3 (but not 1) to ensure that the noisy amplifier is avoided.

The maximum exposure speed in the Raith 150 is claimed to be 10 MHz (10 million pixels per second). For acceptable results, the speed used should not exceed ~ 2 MHz (beam deflection speed of about 8 mm/s on a 100-μm-field). The faster the writing is, the larger the deflection errors discussed in Chapter 7 are. To reduce the writing speed one needs to decrease the e-beam current or increase the SEBL step size. For smooth dose profiles, the step size must be kept below the full-width at half-maximum of the proximity function reported in Chapter 9 (~ 20 nm on 200-nm-thick PMMA). In addition, the e-beam current must be kept sufficiently high for the secondary-electron detector signal to be large enough for one to be able to adjust the SEBL parameters appropriately. For high-index-contrast microphotonic devices exposed in 950 kg PMMA on a 100-μm-field, the best compromise was found to be a 6-nm-step-size and the 20-μm-aperture.

The main advantage of the Raith system with respect to other SEBL systems is its small e-beam size. The resulting high resolution enables exposure of 30 nm lines and spaces.

The e-beam current is generally stable and usually drifts by less than 5%/day. For long device exposures, a macro is available to measure the current and update the dwell time automatically. The macro can be introduced by the user to the Raith position list. This is particularly important when the electron gun is old and the current unstable.

A.1.3 Stage-Related Problems

In the Raith 150, the sample is mounted to a chuck. The chuck is loaded into the system through a load lock to rest on three posts attached to the heterodyne interferometer. The height of two of the three posts can be adjusted with closed-loop piezos to level the sample. The area to be exposed should be leveled to within the depth of focus of the system (~1 μm at 30 KeV). The piezos offer a limited ± 20 μm height adjustment range

that is often insufficient for sample leveling as it results in an angular adjustment range of only ± 0.01 degrees. As a result, the backside of the sample and the sample chuck need to be flat and clean. Any dust particle between the sample and the chuck may prohibit leveling. This is particularly problematic as the Raith is not in a clean environment. In addition, a sample chuck fabricated in a regular machine shop will not be flat enough to allow repeatable leveling. The chuck needs to be lapped after fabrication to ~ 1 μm global flatness.

The three posts in the Raith's chamber fit roughly into grooves machined into the back of the sample chuck. The chuck rests on the posts by gravity. When loading the chuck, one must shake the stage to allow the sample chuck to reach the resting position. The shaking is done by turning on and off a mysterious feedback control of the piezos. It is unsure what this control was meant for but it introduces intolerable noise if left active by accident.

The loose arrangement between the sample chuck and the interferometric stage results in a drift of the chuck with respect to the stage reaching 6 nm/min. As the Raith exposes the e-beam fields of a layout in rows starting from the left bottom corner and going from left to right and bottom to top, the stage drift worsens stitching errors on horizontal field-boundaries (along the "u" coordinate) significantly. Stitching errors on vertical boundaries reach a standard deviation of 20 nm and can result in a ~ 2 dB/cm loss in a SiN waveguide. In practice, we have observed stitching errors on horizontal boundaries reaching 100 nm. For this reason, all microphotonic devices must be laid out horizontally, limiting the number of horizontal stitching errors disturbing light propagation. The lowest left corner of the lowest left e-beam field to be exposed is set by the lowest left limit of patterns to be exposed. A small dummy element should be defined in the layout to fix the position of the field boundaries.

Mechanical vibrations are a major concern in the Raith 150. The dominant mechanical frequency is of about 30 Hz and may reach an amplitude of 10 nm at image acquisition (the relative position of the sample to the e-beam can move with 10-nm-amplitude). This is of particular concern for process calibration, as discussed in Chapter 8, as it limits the dimensional measurement accuracy. Moreover, it can reduce the exposure contrast of small features. The source of vibration is unclear. Geophones measurements performed in Summer 2003 showed a omnipresence of 30 Hz vibration and its harmonics in the room. Moreover, a significant 180 Hz vibration source was found to come from within the Raith. In the Gemini design, the turbo pump is fixed directly to the vacuum chamber. It is claimed to contribute only slightly to vibration with a 60 Hz line. However, the vibration problem worsened considerably when the cooling water flow to the turbo pump was increased in the beginning of 2003 to prevent overheating. In 2004, a vibration isolation platform was installed. The platform helped to isolate the system from floor vibrations significantly. Nonetheless, the arrangement of cables shortcut the isolation system appreciably and this needs to be improved. Moreover, nothing was done to improve isolation from acoustic vibrations and this too should be addressed.

A.1.4 Bugs

The Raith exhibits a significant amount of bugs. In general the layouts should either be created directly in the Raith software or through generation of ".asc" files with Matlab or another programming tool. A partial list of problems not addressed at Raith training is now presented.

- Polygons should be used in the layout. The line function should only be used for single-pixel lines (zero-width lines). For wide lines defined with the line function,

the Raith algorithm can make a significant amount of fill-in errors.

- The e-beam dose factor can be defined in the ".asc" file with 0.1% precision. The dose factor cannot exceed 3000%, however.
- The stand-alone Raith software (the one not running on the actual machine) divides the dose factors by a factor of 100 when loading an ".asc" file.
- Single-pixel lines going through field boundaries should be avoided as they can result in the system dramatically slowing and crashing.
- When selecting the dot base dose in the exposure window, one should be aware that the units suggested by the Raith are wrong and will result in an error on the dwell time of a factor of 1000. It is recommended that one calculates and inputs the base-dose dwell-time directly for dots.
- Layouts using hierarchical elements in the "gds" files will not allow creating dose matrices. The software will allow the user to select a dose factor for the hierarchical element but will not employ it. The base dose will be used by the system at exposure.

A.2 MULTILAYER EXPOSURES

A.2.1 Introduction

Multilayer alignment accuracy below 50 nm can be achieved. The alignment procedure is presented in details in the Raith operation manual. In this section, we present the multilayer approach employed to fabricate the polarization-independent add-drop filters reported in Section 3.4.4. We focus on the key concepts and the common problems encountered.

A.2.2 Signal

To perform alignment, one must somehow acquire positional information on the lower layer. This is done by scanning the e-beam on a region where an alignment mark is expected and collecting information with one of the secondary-electron detectors. As secondary electrons have a diffusion range in materials of a few nanometers, the secondary electrons collected will be the ones emitted at the surface of the resist (or rather at the surface of the Aquasave in our case). The goal is to increase or decrease the number of secondary electrons emitted from the resist-top in the presence of an alignment mark. This can be done by creating a contrast of backscattered electrons between the alignment mark and the surrounding environment. Backscattered electrons cannot be detected directly by the Raith but will generate secondary electrons as they exit the resist and will provide the positional information required. A metal mark will usually create an acceptable backscattering contrast with the surrounding dielectric environment. In general, the heavier the atoms are, the more electrons they backscatter. Note that the alignment marks should be as close to the surface of the sample as possible to achieve acceptable signal as the backscattered electrons have a finite range. In the present work, 55-nm-thick-Cr alignment marks were used with 200 nm of PMMA and 60 nm of Aquasave on top.

A.2.3 Alignment Marks and Acquisition

The alignment procedure is done in two phases summarized in Fig. A.1. First a global alignment is performed by the user. Three widely spaced marks are required. The marks should be big enough to be easily found optically. The positions of the marks on the chuck need to be noted before the sample is loaded. This can be done using a microscope with an appropriate stage. In addition, the marks should have small enough features to

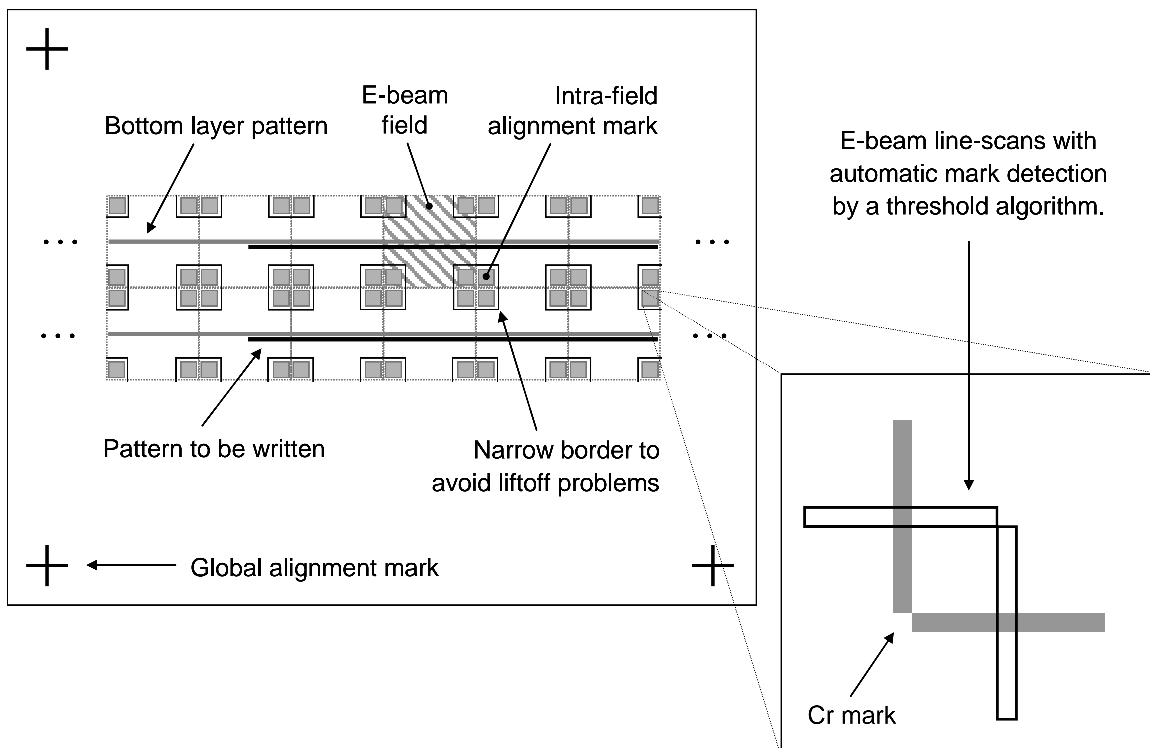

Fig. A.1 Illustration of the multilayer alignment strategy. First, a global alignment is performed by the user on large widely spaced marks. Then, an automatic intra-field alignment can be used to enhance alignment on critical e-beam fields. The intra-field alignment marks are made of 55-nm-thick Cr and are formed of two 5 x 0.5 μm bars arranged into an L-shape. The e-beam is scanned and the marks detected with a threshold algorithm. If Ni liftoff is to be performed following the aligned exposure, a narrow border should be exposed around the alignment marks to prevent these from acting as anchoring points for the Ni film.

allow precise e-beam alignment. In the present work, we used 250 x 250 μm crosses thinned down in the middle to a 100 x 100 nm square crossing.

Once the global alignment is done, a field calibration is performed to ensure appropriate angular alignment of the e-beam field to the lower layer. Then, the exposure is launched. To obtain an alignment accuracy of 50 nm or better, a second phase of alignment is needed. An intra-field alignment is required at every field where alignment is critical. The intra-field alignment can be done automatically by introducing appropriate

mark-acquisition features in the layout to be exposed. In the present work, L-shaped bars were used in the four corners of the e-beam field where intra-field alignment was required. Each L-bar was formed of two 5×0.5 μm lines. The e-beam is scanned in the field corners and a threshold algorithm is used to find the alignment-mark positions. As a 30 KeV electron energy and a small 20 μm aperture need to be used for microring exposures, the signal resulting from the secondary electrons generated by the backscattered ones and collected by the in-chamber detector is very small. Hence, heavy averaging is required. In the present work, we used 5 x 0.5 μm e-beam linescans with 2500 x 200 points and an averaging of 20. A minimum and maximum relative threshold of 70 and 85% was employed. The collector bias of the detector was set at 200 V. Each intra-field alignment with such parameters takes ~ 35 s. After the 72 hours aligned exposure performed for fabricating the polarization independent filters, the relative position of the sample chuck to the interferometric stage had drifted by more than 6 μm. Such a drift would have been disastrous if intra-field alignment had not been applied to compensate it.

When Ni liftoff is planned on PMMA exposed with intra-field alignment, a narrow border should be exposed around the alignment marks at about 10 μm from the marks. The heavily exposed PMMA around the alignment marks will show, after development, smooth gradual edges allowing the Ni film to be continuous and anchored to the SiN at the alignment marks. This creates problems at liftoff as the Ni film does not leave the sample over large areas. The remaining Ni film can be partially removed by ultrasonic agitation. However, a more elegant way to address the problem is to expose, during the aligned exposure, a narrow border around the alignment marks to cut out the Ni film from the anchors formed by the mark acquisition and allow the Ni to leave the sample.

For the threshold algorithm to be automatically applied, it is imperative that the threshold parameter-set to be employed be called “Align write field”. Moreover, the “Autoscan Options” in the “Writefield Alignment Module” found in “Module Status” must be set to “stay;set=Align write field”.

The four alignment marks allow adjustment of the position, the rotation, and the non-orthogonality of the field at every field where intra-field alignment is performed. In consequence, there is no true additional stitching error created during an intra-field aligned exposure. Instead, the top layer is aligned to the stitching errors encountered at exposure of the bottom layer.

A last point to remember when performing multilayer alignment is that the coordinates specified for a given gds-layout in the Raith position list correspond to the middle of the e-beam field in the lower-left corner of the gds-layout. For instance, when using 100-μm-fields, the position of the gds-layout specified in the position list will correspond to the point at 50 μm from the bottom edge and 50 μm from the left edge of the gds-layout. The coordinates in the gds-file have no pre-determined translational offset from the coordinates in the position list.

Bibliography

[1] J.D. Plummer,M.D. Deal, P.B. Griffin, *Silicon VLSI Technology: Fundamentals, Practice and Modeling*, Prentice Hall, Upper Saddle River NJ, (2000).

[2] R. Ramaswami, K.N. Sivarajan, *Optical networks: a practical perspective*, Morgan Kaufmann Publishers, San Francisco CA, (2002).

[3] E.A.J. Marcatilli, "Bends in Optical Dielectric Waveguides", *Bell System Technical Journal* **48**, pp. 2103–2132, (1969).

[4] Little B.E., Chu S.T., Haus H.A., J. Foresi, and J.-P. Laine, "Microring Resonator Channel Dropping Filters," *J. Lightwave. Technol*. **15**, pp. 998-1005, (1997).

[5] A. Yariv, *Optical Electronics in Modern Communication*, Oxford University Press, New York, (1997).

[6] Y. Yanagase, S. Suzuki, Y. Kokubun, and S.T. Chu, "Box-like filter response and expansion of FSR by a vertically triple coupled microring resonator filter," *J. Lightwave. Technol*. **20**, pp. 1525-1529, (2002).

[7] M.R. Watts, "Polarization independent microphotonic circuits," *PhD. Thesis*, Massachusetts Institute of Technology, Cambridge MA, (2005).

[8] M. A. Popovic, M.R. Watts, T. Barwicz, P. T. Rakich, L. Socci, E.P. Ippen, F.X. Kärtner and H.I. Smith, "High-index-contrast, wide-FSR microring-resonator filter design and realization with frequency-shift compensation," *presented at the Optical Fiber Communication Conference OFC/NFOEC'05*, OFK1, Anaheim CA, (2005).

[9] M. A. Popovic, T. Barwicz, M.R.Watts, P. T. Rakich, L. Socci, E.P. Ippen, F.X. Kärtner and H.I. Smith, "Multistage high-order microring-resonator filters with relaxed tolerances for high through-port extinction," *presented at the Conference on Lasers and Electro-Optics CLEO/QELS'05*, CMP2, Baltimore MD, (2005).

[10] M.R. Watts, T. Barwicz, M. A. Popovic, P. T. Rakich, L. Socci, E.P. Ippen, F.X. Kärtner and H.I. Smith, "Microring-resonator filter with doubled free-spectral-range by two-point coupling," *presented at the Conference on Lasers and Electro-Optics CLEO/QELS'05*, CMP3, Baltimore MD, (2005).

[11] M.A. Popovic, “High-index-contrast integrated optical resonators and filters”, *PhD. Thesis in preparation*, Massachusetts Institute of Technology, Cambridge MA, (2006).

[12] Mitsubishi Rayon America Inc. (2004), *aquaSAVE Datasheet*, [Online] Available: http://www.mrany.com.

[13] J.V. Hryniewicz, P.P. Absil, B.E. Little, R.A. Wilson and P.-T. Ho, “Higher order filter response in coupled microring resonators,” *IEEE Photon. Technol. Lett.* **12**, pp. 320-322, (2000).

[14] B.E. Little, “A VLSI Photonic Platform,” *in Proceedings of Optical Fiber Communication Conference*, Optical Society of America, Washington DC, vol. 2, pp. 444-445, (2003).

[15] C. Manolatou, M.A. Popovic, P.T. Rakich, T. Barwicz, H.A. Haus and E.P. Ippen, “Spectral anomalies due to coupling-induced frequency shifts in dielectric coupled resonator filters,” *presented at the Optical Fiber Communication Conference*, Los Angeles, CA, USA, 22-27 Feb. (2004).

[16] M.R. Watts, M. Qi, T. Barwicz, L. Socci, P.T. Rakich, E.P. Ippen, H.I. Smith, H.A. Haus, "Towards integrated polarization diversity: design, fabrication and characterization of integrated polarization splitters and rotators," *presented at the Optical Fiber Communication Conference OFC/NFOEC’05*, Postdeadline PDP11, Anaheim CA, (2005).

[17] M.R. Watts, H.A. Haus, and E.P. Ippen , “Integrated mode-evolution-based polarization splitter ,” *Optics Letters* **30**, pp. 967-969, (2005).

[18] M.R. Watts and H.A. Haus, “Integrated mode-evolution-based polarization rotators,” *Optics Letters* **30**, pp. 138-140, (2005).

[19] T. Barwicz and M.Qi, "Improved multilayer processing by functional separation of material deposition, lithography, and etching," *Provisional US and International Patent*, (2004).

[20] D. Marcuse, “Radiation Losses of dielectric waveguides in terms of the power spectrum of the wall distortion function”, *Bell Syst. Tech. J.* **48**, pp. 3233-3244, (1969).

[21] J.P.R. Lacey and F.P. Payne, “Radiation loss from planar wave-guides with random wall imperfections”, *IEE Proc.-J*. **137**, pp. 282-288, (1990).

[22] F. Ladouceur, J.D. Love and T.J. Senden, “ Effect of side wall roughness in buried channel waveguides,” *IEE P-Optoelectron*. **141**, pp. 242-248, (1994).

[23] T. Barwicz, H.A. Haus and H.I. Smith, “A three-dimensional analysis of scattering losses due to sidewall roughness in integrated optical waveguides,” *presented at the Conference on Lasers and Electro-Optics CLEO/QELS’03*, Baltimore MD, June (2003).

[24] K. K. Lee, D.R. Lim, H.C. Luan, A. Agarwal, J. Foresi, and L.C. Kimerling, “Effect of size and roughness on light transmission in a Si/SiO2 waveguide: experiments and model,” *Appl. Phys. Lett.* **77**, pp. 1617-1619, (2000).

[25] J. A. Ogilvy and J. R. Foster, “Rough surfaces - gaussian or exponential statistics,” *J.Phys. D: Appl. Phys.* **22**, pp. 1243-1251, (1989).

[26] J.S. Lim, *Two-dimensional signal and image processing,* Prentice Hall, Englewood Cliffs NJ, pp. 536-540, (1990).

[27] J. Canny, "A computational approach to edge-detection," *IEEE Trans. Pattern Analysis and Machine Intelligence* **PAMI-8**, pp. 679-698, (1986).

[28] R. B. Blackman and J. W. Tukey, *The Measurement of Power Spectra*, Dover, New York, (1958).

[29] H. Akaike and T. Nakagawa, *Statistical Analysis and Control of Dynamic Systems*, KTK, Tokyo, (1988).

[30] H. Akaike, "Statistical predictor indentification," *Ann. Inst. Statist. Math*. **22**, pp. 203-217 (1970).

[31] M. Ediger, "A Gauss-Newton Method for Nonlinear Regression," *Mathematica Journal* **1** (2), p. 42, (1990).

[32] C. Nelson, S.C. Palmateer, A.R. Forte and T.M. Lyszczarz, "Comparison of metrology methods for quantifying the line edge roughness of patterned features," *J. Vac. Sci. Technol. B* **17**, pp. 2488-2498, (1999).

[33] S. Yasin, D.G. Hasko, M.N. Khalid, D.J. Weaver, and H. Ahme, "Influence of polymer phase separation on roughness of resist features," *J. Vac. Sci. Technol. B* **22**, pp. 574-578, (2004).

[34] Yurii A. Vlasov and Sharee J. McNab, "Losses in single-mode silicon-on-insulator strip waveguides and bends," *Optics Express* **12**, pp. 1622-1631, (2004).

[35] M.S. Kulkarni, "A review and unifying analysis of defect decoration and surface polishing by chemical etching in silicon processing," *Ind. Eng. Chem. Res*. **42**, pp. 2558-2588, (2003).

[36] D. Marcuse, "Mode conversion caused by surface imperfections of a dielectric slab waveguide", *Bell Syst. Tech. J*. **48**, pp. 3187-3215, (1969).

[37] D.G. Hall, "Comparison of two approaches to the waveguide scattering problem," *Applied Optics* **19**, pp. 1732-1734, (1980).

[38] R.W.Gruhlke and D.G. Hall, "Comparison of two approaches to the waveguide scattering problem: TM polarization," *Applied Optics* **23**, pp. 127-133, (1984).

[39] F.P. Payne and J.P.R. Lacey, "A theoretical analysis of scattering loss from planar optical waveguides", *Opt. Quant. Electron*. **26**, pp. 977-986, (1994).

[40] K.S. Chiang, C.H. Kwan, and K.M. Lo, "Effective-index method with built-in perturbation correction for the vector modes of rectangular-core optical waveguides," *J. Lightwave Technol.* **17**, pp. 716-722, (1999).

[41] H.A.Haus, Massachusetts Institute of Technology, Cambridge MA, *private communication*, Jan. (2002).

[42] T. Barwicz, “3D analysis of scattering losses due to sidewall roughness in microphotonic waveguides: high-index contrast,” *presented at the Conference on Lasers and Electo-Optics CLEO/QELS’05*, Baltimore MD, May (2005).

[43] N.E. Nahi, *Estimation theory and applications*, New York, Wiley, (1969).

[44] M. Kuznetsov and H.A. Haus, “Radiation loss in dielectric waveguide structures by the volume current method,” *IEEE J.Quantum Electron*. **QE-19**, pp. 1505-1514, (1983).

[45] J.A. Kong, *Electromagnetic Wave Theory*, Cambridge MA, EMW Publishing, (2000).

[46] W.C. Chew, *Waves and fields in inhomogeneous media*, New York, IEEE Press, (1995).

[47] W.C. Chew and S.Y. Chen, “Response of a point source embedded in a layered medium,” *IEEE Antennas Wireless Propagat. Lett*. **2**, pp. 254-258, (2003).

[48] J.C.Cooke, “Stationary Phase in Two Dimensions,” *IMA J. Appl. Math*. **29**, pp. 25-37, (1982).

[49] W. Gander and W. Gautschi, “Adaptive Quadrature - Revisited,” *BIT* **40**, pp. 84-101, (2000).

[50] S. J. Spector, M. W. Geis, D. M. Lennon, R. C. Williamson, and T. M. Lyszczarz, “Hybrid multi-mode/single-mode waveguides for low loss,” *presented at the Integrated Photonics Research Topical Meeting*, San Francisco CA, June 27-July 2, (2004).

[51] A. Taflove and S. C. Hagness, *Computational electrodynamics: the finite-difference time-domain method*, Boston, Artech House, (2000).

[52] M.J. Shaw, J. Guo, G.A. Vawter, S. Habermehl, and C.T. Sullivan, “Fabrication techniques for low loss silicon nitride waveguides,” *presented at the 2005 Photonics West Conference*, Paper No. 5720-15, San Jose CA, Jan. (2005).

[53] K. Worhoff, A. Driessen, P.V. Lambeck, L.T.H. Hilderink, P.W.C. Linders, T.J.A. Popma, “Plasma enhanced chemical vapor deposition silicon oxynitride optimized for application in integrated optics”, *Sensors and Actuators* **74**, pp. 9-12 (1999).

[54] L. Dal Negro, Massachusetts Institute of Technology, Cambridge MA, *private communication*, Jan. (2005).

[55] P. Pellegrino, B. Garrido, C. Garcia, J. Arbiol, J. R. Morante, M. Melchiorri, N. Daldosso, L. Pavesi, E. Scheid and G. Sarrabayrouse, “Low-loss rib waveguides containing Si nanocrystals embedded in SiO_2,” *Journal of Applied Physics* **97**, Art. No. 074312, (2005).

[56] J. Petalas, S. Logothetidis, S. Boultadakis, and A. Markwitz, “The effect of hydrogen and temperature on the optical gaps of silicon nitride and comparative stoichiometriy studies on SiN thin films,” *Journal of Non-Crystalline Solids* **187**, pp.292-296, (1995).

[57] B.E. Little and S.T. Chu, “Estimating surface-roughness loss and output coupling in microdisk resonators”, *Optics Letters* **21**, pp. 1390-1392 (1996).

[58] U. Hofmanna, R. Crandall, L. Johnson, “Fundamental performance of state-of-the-art proximity effect correction methods,” *J. Vac. Sci. Technol. B* **17**, pp. 2940-2944, (1999).

[59] L. Stevens, R. Jonckheere, E. Froyen, S. Decoutere, and D. Lanneer, “Determination of the proximity parameters in electron beam lithography using doughnut-structures,” *Microelectron. Eng.* **5**, pp. 141-150, (1986).

[60] S.A Rishton and D.P. Kern, “Point exposure distribution measurements for proximity correction in electron-beam lithography on a sub-100 nm scale”, *J. Vac. Sci. Technol. B* **5**, pp. 135-141, (1987).

[61] T.H..P. Chang, “Proximity effect in electron-beam lithography,” *J. Vac. Sci. Technol.* **12**, pp. 1271-1275, (1973).

[62] Y. Ma, F. Cerrina, T. Barwicz, and H.I. Smith, “Theoretical and experimental study of electron beam exposure for microphotonic devices,” *presented at the Electron, Ion and Photon Beam Technology and Nanofabrication Conference*, *EIPBN’05*, Orlando FL, May 31-June 3, (2005).

[63] S.A. Prahl, “Light transport in tissue,” *Ph.D. Thesis*, University of Texas at Austin, (1988).

[64] N. Ponnampalam, R. G. DeCorby, H. T. Nguyen, P. K. Dwivedi, C. J. Haugen, J. N. McMullin, and S. O. Kasap, “Small core rib waveguides with embedded gratings in As_2Se_3 glass,” *Optics Express* **12**, pp. 6270-6277, (2004).

[65] Y. Ruan, W. Li, R. Jarvis, N. Madsen,A. Rode, B. Luther-Davies “Fabrication and characterization of low loss rib chalcogenide waveguides made by dry etching,” *Optics Express* **12**, pp. 5140-5145, (2004).